ISTANBUL TECHNICAL UNIVERSITY ★ GRADUATE SCHOOL OF SCIENCE ENGINEERING AND TECHNOLOGY

DEVELOPMENT OF IRON-RICH ANODE MATERIALS FOR LITHIUM-ION BATTERY TECHNOLOGY FROM LOCAL FeCr ALLOYS

M.Sc. THESIS

Mehmet Feryat GÜLCAN

Department of Metallurgy and Material Engineering

Material Engineering Programme

JULY 2020

ISTANBUL TECHNICAL UNIVERSITY ★ GRADUATE SCHOOL OF SCIENCE ENGINEERING AND TECHNOLOGY

DEVELOPMENT OF IRON-RICH ANODE MATERIALS FOR LITHIUM-ION BATTERY TECHNOLOGY FROM LOCAL FeCr ALLOYS

M.Sc. THESIS

Mehmet Feryat GÜLCAN
(506181420)

Department of Metallurgical and Material Engineering

Material Engineering Programme

Thesis Advisor: Prof. Dr. Sebahattin GÜRMEN
Thesis Co-Advisor: Asist.Prof. Dr. Billur Deniz KARAHAN

JULY 2020

İSTANBUL TEKNİK ÜNİVERSİTESİ ★ FEN BİLİMLERİ ENSTİTÜSÜ

YERLİ FeCr ALAŞIMLARINDAN LİTYUM İYON PİL TEKNOLOJİSİ İÇİN DEMİRCE ZENGİN ANOT MALZEMELERİNİN GELİŞTİRİLMESİ

YÜKSEK LİSANS TEZİ

Mehmet Feryat GÜLCAN
(506181420)

Metalurji ve Malzeme Mühendisliği Anabilim Dalı

Malzeme Mühendisliği Programı

Tez Danışmanı: Prof. Dr. Sebahattin GÜRMEN
Eş Danışman: Dr. Öğrt. Üy. Billur Deniz KARAHAN

TEMMUZ 2020

Mehmet Feryat GÜLCAN, a M.Sc. student of ITU Graduate School of Science Engineering and Technology student ID 506181420, successfully defended the thesis/dissertation entitled "DEVELOPMENT OF IRON-RICH ANODE MATERIALS FOR LITHIUM-ION BATTERY TECHNOLOGY FROM LOCAL FeCr ALLOYS", which he prepared after fulfilling the requirements specified in the associated legislations, before the jury whose signatures are below.

Thesis Advisor :	**Prof. Dr. Sebahattin GÜRMEN** Istanbul Technical University	.....
Co-advisor :	**Asist.Prof. Dr. Billur Deniz KARAHAN** Istanbul Medipol University	.....
Jury Members :	**Prof. Dr. Özgül KELEŞ** Istanbul Technical University	.....
	Asist.Prof. Dr. Mehmet Şeref SÖNMEZ Istanbul Technical University	.....
	Prof. Dr. Gökhan ORHAN Istanbul University	.....

Date of Submission : 12 June 2020
Date of Defense : 20 July 2020

To someone…

FOREWORD

Firstly, I want to thank my thesis advisor, Prof. Dr. Sebahattin GÜRMEN for his guidance during my thesis study.

I sincerely thank to my co-advisor Assist. Prof. Dr. Billur Deniz KARAHAN for allowing me to be a part of her project (218M768). I also express my sincere gratitude to her for the valueable support and guidance during my research.

I would like to extend my deepest gratitude to to Prof. Dr. Özgül KELEŞ, Prof. Dr. Gültekin GÖLLER, Prof. Dr. Süheyla AYDIN, Prof. Dr. M. Kürşat KAZMANLI, Dr. Selim ERTÜRK and my collegues Msc. Eren İNEL, Msc. İpek TUNÇ, Semih ATEŞ, Spc. Chem. Büşra ŞAHİN KURT, Msc. Reyhan SOLMAZ, Msc. Erdem BALCI and Dr. Yonca ALKAN GÖKSU for their helps in characterizations. In addition, I would like to thank Dr. Alper YEŞİLÇUBUK and Msc. Dilan ER from Arçelik A.Ş. for their helps in characterization.

Moreover, I want to thank to Dr. Semih ÖNCEL and Msc. Ömer ÇAYLAN (from TOBB University) for their helps in heat treatments .

Moreover, I would like to acknowledge the helps of Ahmet CAN, Celil ÇAKAN and Yahya BEYCE from Uzman Kataforez Yüzey Kaplama A.Ş. for Atomic Absorption Spectroscopy analysis.

I would like to thank Medipol University Faculty of Engineering and Natural Science for providing research opportunities. Also, I want to thank to REMER (Regenerative and Restorative Medicine Research Center) for providing SEM analysis.

I gratefully acknowledge Eti Krom A.Ş. for supplying ferrochromium as the precursor material

The data presented in this thesis includes some of the results of the study carried out within the scope of the Tübitak project (Project No: 218M768). Therefore, I would like to thank TUBITAK for their support.

Last but not the least, I would like to thank my family for being a part of my life.

July 2020

Mehmet Feryat GÜLCAN
(Metallugical and Material Eng.)

TABLE OF CONTENTS

Page

ABBREVIATIONS

CV	**:** Cycling Voltametry
FeCr	**:** Ferrochromium
SEI	**:** Solid Electrolyte Interface
PVDF	**:** Polyvinylidene Difluoride
NMP	**:** N-Methylpyrrolidone
TMO	**:** Transition Metal Oxide
TMOx	**:** Transition Metal Oxalate
FeOxH	**:** Iron Oxalate Hydrate
FeOxA	**:** Iron Oxalate Anhydrous
FeO	: Iron Oxide
XRD	**:** X-Ray Diffraction
SEM	**:** Scanning Electron Microscope
EDS	**:** Energy Dispersive X-ray Spectroscopy
AAS	**:** Atomic Absorption Spectroscopy
LIBs	**:** Lithium Ion Batteries
TGA	**:** Thermal Gravimetric Analysis
DTA	**:** Diffrential Thermal Analysis

SYMBOLS

µm	**:** Micrometer
nm	**:** Nanometer
˚C	**:** Degree Celcius
K	**:** Kelvin
V	: Voltage

LIST OF TABLES

Page

LIST OF FIGURES

Page

DEVELOPMENT OF IRON-RICH ANODE MATERIALS FOR LITHIUM-ION BATTERY TECHNOLOGY FROM LOCAL FeCr ALLOYS

SUMMARY

Energy is an indispensable concept for all creatures to survive. Energy is also needed to increase the quality of lives. At this point, it can be said that secondary batteries become important because they play a critical role in the widespread use of portable devices that are employed in defence, home appliance and medical applications. Among the secondary batteries, lithium-ion batteries stand out in terms of their light in weight, high safety, theoretical capacity and energy density. However, their high costs restrict their extensive uses.

History shows that after the industrial revolution steam machines replaced manpower and fossil fuels that were used to prefer as the energy source of the machines. However, mankind was greedy. Countries that became stronger with the acceleration of industrialization sought new resources in different geographies to meet their ever-increasing energy needs. This quest has led to various energy crises until this date.

The positive opportunities provided by the use of energy obtained from renewable energy sources rather than the use of limited energy resources such as fossil have been expressed in many different platforms.

The discontinuity of such renewable energy in question is overcome by the development of energy storage technologies. Following the works of Galvani and Volta in the 18th century, the first battery types were produced by Exxon in the 1970s where titanium disulphide and lithium metal were used as the cathode and the anode materials, respectively.

Then in the 1990s, Goodenough et al. created a great milestone for studies on energy storage technologies with the secondary battery system that they proposed. In this battery (LIB) design transition metals were used as cathode and carbon was used as the anode materials. The fact that in 2019, they were awarded the Nobel Prize thanks to their LIB design, officially documented the importance of such technology in the world history. Then in 1980, Armand published the intercalation mechanism of lithium metal in LIB. In 1991, Sony announced the introduction of the LIB as a product into the market. Today, the market of lithium-ion batteries is growing day by day, while the researches to improve their energy and power densities as well as safety are also increasing exponentially.

Simply, a lithium ion battery consists of four main elements: separator, negative electrode (Anode) , positive electrode (Cathode) and electrolyte. In charging, lithium ions of the cathode pass through the electrolyte and get in to the negative electrode, while electrons follow the ions and move on the external circuit to go to the anode. Then in discharging, lithium ions leave the anode material and return to their initial

place in the cathode material. Meanwhile, electrons direct the stored energy to the desired application. Examples of positive electrodes include $LiCoO_2$, $LiFePO_4$ and $LiMnO_2$, and the most widely used negative electrodes are silicon, transition metal oxide, and graphite.

These electrode materials are produced by a wide variety of synthetic methods. However, in many of these production methods, since the starting material is of high purity, industrial scaled production processes often require working with a continuous maintenance of high quality raw materials. In this type of production process, where raw materials are dependent on foreign countries, the input value becomes unstable which causes financial difficulties in the production for long term business. Also, the transportation of the raw material to different places may provoke environmental damages due to CO_2 gas release during logistic process.

In this thesis, iron-rich anodes for lithium-ion batteries have been fabricated by using hydrometallurgical methods where an indigienous metallurgical quality ferrochromium is used as the raw material. Herein, ferrochromium is particularly chosen as Turkey is well recognized with the high and good quality of ferrochromium that are fabricated in Elazığ and Antalya. In this thesis work, high carbon (wt.%5) contained ferrochromium alloy is supplied from Eti Krom A.Ş (Elazığ).

The aim is to design an environmentally friendly and practical process to fabricate iron rich oxide powders from an indigenenous ferrochrome alloy. The originality of this thesis lies in two concepts: material and method. First of all, by using an indigeneous product as precursor, a material is fabricated for a high value added application such as electrode material for lithium ion battery. Herein, the existence of other transition metals in the fabricated powder is believed to create electron conductive pathways in the electrode to improe its rate performance. Secondly, the fact that during the experiment, a rotary evaporator has been used in leaching, the change in the solid-liquid interaction is expected to affect the leaching mechanism as well. The latter enriches the literature since no similar approach has been reported previously.

In the scope of the thesis, in order to maximize the iron leaching efficiency with the least number of experiments and analysis the most effective parameters, Taguchi orthagonal method has been used.

Therefore, in the first chapter of the thesis, the particle size of ferrochromium containing wt.5% carbon was reduced by ball miling using Taguchi orthogonal array ($L_4(2^3)$). As a result of the Taguchi analysis (4 experiments), the smallest grain size was obtained as average (Dv50) 2.72 μm when the powder was ball milled in 4 hours, at 235 rpm and 10:1 balls:powder ratio. In ANOVA analysis, the most effective parameter was found to be duration. In the second chapter of the thesis, the process parameters related to leaching of the ferrochromium alloy with sulphuric acid were optimized by Taguchi method ($L_9(3^4)$) with 4 parameters and 3 levels. Herein first in the literature rotary evaporator was used as the leaching reactor. It is believed that the change in powder/liquid interaction would differentiate the leaching efficiency. Within the scope of this study, sulphuric acid is particularly chosen as the acidic medium to prevent the occurance of hexavalent chromium in leachate, which has a harmful effect on human health. Later, the effect of the duration, precursor particle size and stirring rate on the lecahing efficiency have been studied. In total 15 experiments were done to optimize the leaching conditions. As a result of the Taguchi analysis, the optimum parameters were obtained as 5 molar sulfuric acid, 1:50 volumetric solids: liquid ratio, 30 rpm and 90˚C at 150 minutes. The result showed that 91.88% corelation was

achieved successfully between the theoretically calculated and the experimentally achieved values in leaching. the ANOVA analysis demonstrated that the most effective parameter for iron leaching was solid: liquid ratio. After these experiments, in order to examine the effect of the grain size of the starting solid material on the iron leaching yield, the experiment was carried out using ferrochromium with a larger grain size ((Dv50) of 107.5 μm). As a result, it was observed that the precursor material with a larger grain size yield lower efficiency. Once the leaching parameters were optimized, longer leaching duration were done for investigating leaching duration effect. The leaching kinetic was analzyed and revelaed that surface reaction and lixiviant diffusion through solid particles determined the iron leaching.The mixed model for leaching kinetic was mathematically explained as follows: $-\ln(1-x)=k\,t^{0.4}$.In order to examine this model in more detail, the effect of mixing speed was also examined. In the third chapter, in order to evaluate the possible use of this sulphate solution in the battery application, a selective chemical precipitation was done. Oxalic acid was preferentially used to structure the iron oxalate precipitate in the shape of nanorods. Because, literature survey depicts that nanorods increase the electrolyte/active material contact area and decreases Li^+ diffusion distance. Therefore, enhanced electrochemical performance is expected to achieve when nanorod-structured anode was used in comparison to bulk powders. Morever, during precipitation, by adjusting pH of the solution other transition metals like Ni, Co were also embedded in the nanorod structured iron oxalate particles, to further improve the rate performance of the anode material. For optimizing the precipitation conditions, four experiments were realized. The effects of temperature, stirring velocity and volumetric oxalic acid:leaching solution ratio on the precipitation efficiency were examined. Fourtly, iron-rich oxide powders, which were selectively recovered from the leachate, were processed in varying heat treatment conditions. Herein 8 samples have been fabricated to discuss the effect of temperature, duration and environment on the final product properties. Finally, once these 8 powders were structurally, chemically and morphologically characterized, their uses as an anode material in LIB were reported based on the galvanostatic test results.

The galvanostatic analyses were realized when these 8 samples were tested between 1mV-3V under a load of 50mA/g. The results demonstrated that 6 samples (FeOxA2, FeOxA3, FeOxA6, FeO3003, FeO3002 and FeO2153) delivered higher capacities than graphite after 100 cycles. In case of iron oxalate samples, FeOxA3 delivered the highest first discharge capacity (1038.46 mAh/g) value and highest capacity (673.08 mAh/g) at the 94th cycle. In the cyclic voltammetry analysis, characteristic peaks of iron oxide and iron oxalate were found, lithiation mechanism of the electrodes are discussed based on electrochemical tests results.

YERLİ FeCr ALAŞIMLARINDAN LİTYUM İYON PİL TEKNOLOJİSİ İÇİN DEMİRCE ZENGİN ANOT MALZEMELERİNİN GELİŞTİRİLMESİ

ÖZET

Enerji canlı varlıklar için yaşamlarını sürdürebilmeleri adına vazgeçilmez bir kavramdır. İnsanlar ise yaşamsal faaliyetlerinin yanı sıra geliştirdiği teknolojiyi kullanabilmek için de enerjiye ihtiyaç duymaktadır. Eski zamanlarda bu tür teknolojiler için insan veya hayvan gücü kullanılırken sanayi devriminden sonra buharlı makinalara geçilmiştir. Günümüzde ise gelişen teknolojiler taşınabilir enerji kaynaklarına ihtiyaç duymaktadır.

Sekonder (ikincil) elektrokimyasal enerji depolama aygıtları tekrar kullanılabilmeleri bakımından günümüzdeki enerji sorununun çözümü için önem arz etmektedir. İkincil piller arasında lityum iyon bataryalar hafif ve güvenli olmalarının yanı sıra alterantiflerinenazaran daha yüksek teorik kapasite ve enerji yoğunluğu sergiledikleri için son yıllarda - ön plana çıkmaktadırlar. Ancak yüksek üretim maliyetleri kullanımlarını sınırlandırmaktadır

Enerji depolama teknolojileri tarihi incelendiğinde Galvani ve Volta'nın 18. yüzyıldaki çalışmalarını takiben, 1970'lerde ilk akü tipleri Exxon tarafından üretildiği görülmektedir. Bu tasarımda katot ve anot malzemeleri olarak titanyum disülfit ve lityum metaleri kullanıldığı belirtilmiştir.

1990'larda ise Goodenough ve ekibinin önerdikleri ikincil pil sistemi ise enerji depolama teknolojileri üzerine çalışmalar için büyük bir kilometre taşı etkisi yarattı. Bu batarya (LIB) tasarımında katot olarak geçiş metalleri, anot malzemeleri olarak karbon kullanılmıştır. 2019'da LIB tasarımları sayesinde Nobel Ödülü'ne layık olmaları, bu teknolojinin dünya tarihinde önemini resmi olarak belgelemiştir. Daha sonra 1980'de Armand, LIB'de lityum metalin interkalasyon mekanizmasını yayınlamış ve 1991'de Sony, LIB'nin piyasaya bir ürün olarak tanıtıldığını duyurmuştur. Günümüzde lityum-iyon pil pazarı günden güne büyürken, enerji ve güç yoğunluklarının yanı sıra güvenliğini artırmak için yapılan araştırmalar da katlanarak artmaktadır.Yapılan araştırmalar ise bu pillerin performans, üretim, maliyet ve güvenlik özelinde devam etmektedir.

Basitçe bir lityum iyon pil dört ana elementten oluşmaktadır. Bunlar sırası ile separatör, negatif elektrot (anot), pozitif elektrot (katot) ve elektrolittir. Bir lityum iyon pilde şarj ve deşarj reaksiyonları gerçekleşmektedir. Şarj tepkimesinde katottaki lityum iyonları anoda elektrolit yardımı ile geçmektedir. Elektronlar ise harici bir devre elemanı ile katottan anoda gitmektedir. Deşarj tepkimesi ise şarj tepkimesinin tersi biçiminde açıklanabilir. Deşarj sırasında, elektronlar depolanan enerjiyi istenen uygulama alanına yönlendirir. Pozitif elektrot örnekleri arasında $LiCoO_2$, $LiFePO_4$ ve

$LiMnO_2$ bulunurken, silikon ve grafit ise negatif elektrotlarda kullanılan malzemelere örnek olarak verilebilir.

Belirtilen bu elektrot malzemeleri çok çeşitli sentetik yöntemlerle üretilir. Bununla birlikte, bu üretim yöntemlerinin çoğunda, başlangıç malzemesi yüksek saflıkta olduğu için, üretim süreçleri sürekli ve düzenli yüksek saflıkta ham madde teminine dayalı olarak sürdürülmektedir. Hammaddelerin yabancı ülkelere bağımlı olduğu bu tür üretim sürecinde, girdi değerinin dengesiz olması uzun vadede üretimde finansal zorluklara neden olabilir. Bunun yanı sıra, birçok ürünün farklı konumlardan taşınmasıyla üretimin gerçekleştirilmesi, lojistik süreçte salınan CO_2 gazı nedeniyle çevresel hasara neden olabilir.

Bu tez çalışmasında günümüz dünyasının problemleri doğrultusunda yerli, metalürjik kalitede ferrokrom kullanılarak hidrometalürjik yöntemlerle lityum iyon piller için demir esaslı anotların üretimi amaçlanmıştır. Bu tez kapsamında literatürde ilk defa Türkiye'de üretilen ferrokrom alaşımı başlangıç malzemesi olarak kullanılarak farklı demir oksit yapılar üretilmiş, karakterize edilmiş, anot olarak performansları incelenmiştir. Hammadde olarak yerli ferrokrom alaşımını tercih ederek maliyet ve çevresel zararın azaltılması amaçlanmıştır. Aynı zamanda ferrokrom yapısında eser miktarda bulunan diğer geçiş metallerini de tasarlanan proses sayesinde demir oksit yapısına geçirerek demir esaslı anotlarda yaşanan iletkenlik probleminin de çözülmesi hedeflenmiştir.

Bu tez kapsamında kullanılan başlangıç malzemesi ve üretim yöntemi çalışmayı anot malzemesi tasarlayan direk araştırmalardan farklı kılmaktadır. Literatür incelendiğinde daha önce ağırlıkça 5% karbon içeren yerli ferrokrom alaşımının hidrometalurjik yöntemlerle (liç ve selektif çöktürme) işlenmesi suretiyle demirce zengin metal oksit anotları üretiminde kullanılmasına dair benzer br çalışmaya rastlanmamıştır. Liç işlemi sırasında döner evaportör kullanmak suretiyle elde edilen katı-sıvı değişiminin de proses verimine etki ilk defa bu araştırma ile incelenmiştir. Bilindiği üzere cevherden yapılan birincil üretim fazla enerji harcanmasına ve yüksek miktarda atık oluşumuna sebep olmaktadır. Ayrıca, yüksek safiyetteki hammadde kullanımının da üretimde yüksek maliyetlere yol açtığı bilinmektedir. Bu doğrultuda başlangıç malzemesi olarak metalürjik kalitede yerli ferrokrom kullanarak ve hidrometalurjik temelli üretim prosesi tasarlayarak daha az maliyetli ve daha az çevreye zararı olan yüksek katma değere sahip elektrot malzemelerinin elde edilmesi amaçlanmıştır.

Bu kapsamda, yerli ferrokromdan demirce zengin çubuklar üretmek için çevre dostu, pratik ve ulusal bir süreç tasarlanmıştır.

Bu tez çalışmasında, çevre dostu, ekonomik ve yüksek katma değerli ürün elde etmek için çevre dostu üretim tasarlanmış, deney parametreleri ayrı ayrı optimize edilmiştir. Bu bağlamda, tezin ilk başlığında ağ. % 5 karbon içeren ferrokromun, parçacık boyutu Taguchi Ortagonal yöntemi ($L_4(2^3)$) kullanılarak bilyalı öğütme ile küçültülmesi için 4 adet deney Taguchi yönteminden yararlanılarak tasarlanmış ve gerçekleştirilmiştir. Taguchi analizi sonucunda, "küçük daha iyidir" yaklaşımıyla yapılan istatistiksel inceleme en küçük partikül boyutunun ((Dv50) 2.72 μm) 4 saatte 235 rpm hızda ve 10:1 ağırlıkça bilya:toz oranında öğütülmesi ile elde edildiğini ortaya çıkarılmıştır. Yapılan ANOVA analizinde ise en etkili parametrenin süre olduğu görülmüştür. Tezin çalışmasının ikinci aşamasında ise ferrokromda bulunan geçiş metallerini çözeltiye almak üzere sülfürik asit ile liç işlemi gerçekleştirilmiştir. Sülfürik asidin tercih sebebi insan sağlığına olumsuz etki yaratan hekzavalent kromun açığa çıkmasını

engellemektir. Optimum parametreleri bulmak adına Taguchi ortagonal yöntemi ($L_9(3^4)$) ile 4 parametre 3 seviye ile deney parametrelerine karar verilmiştir. Daha sonra sürenin etkinliği kontrol deneyi parametreleri ile yapılan inceleme ile ortaya çıkartılmıştır. "büyük daha iyidir" istatistiksel yaklaşımı ile yapılan hesaplamalar 5 molar sülfirik asit çözeltisinde, 1:50 hacimce katı:sıvı oranında, 30 rpm döndürme hızında ve 90˚C çözelti 150 dak'da yapılan liç işlemi ile en yüksek demir çözme veriminin elde edildiği anlaşılmıştır.İstatistiksel verilerden yola çıkarak yapılan teorik hesapla optimum koşullarda gerçekleştirilen liç deneyinden elde edilen sonucun 91,88% oranında benzerlik gösterdiği görülmüştür. Yapılan ANOVA analizinde liç işlemi ile demirin çözeltiye geçmesi için ise en etkin parametrenin hacimce katı: sıvı oranı olduğu hesaplanmıştır. Daha sonra sürenin etkisi ayrı bir deney olarak incelenmiş ve en optimum koşulun 150 dakikada elde edildiği anlaşılmıştır. Bu deneyler sonrasında başlangıç katı malzemesinin tane boyutunun liç verimine olan etkisini inceleyebilmek adına daha büyük tane boyutuna sahip ((Dv50) 107,5 μm) ferrokromlar kullanılarak deney yapılmıştır. Bunun neticesinde daha düşük tane boyutuna sahip başlangıç katısının daha yüksek demir verimine sahip olduğu görülmüştür. Daha sonra optimum parametreler ışığında gerçekleştirilen liç kinetiği analiz edilmiştir. Yapılan hesaplar liç kinetiğinin karma model ile ifade edileceğini ortaya çıkarmıştır. Proses yüzey reaksiyon kontrolü; çözelti difüzyon modeli olarak ortaya konmuştur. $-\ln(1-x) = k.t^{0.4}$, liç kinetiğinie ait matematiksel denklem olarak ifade edilmiştir. Bu modelin daha detaylı irdelenebilmesi adına karıştırma hızının etkisi de incelenmiştir. Sonuç olarak üslü ifadeden de ortaya konulduğu üzere liç işleminin kinetiğinin difüzyon eğilimli olduğu anlaşılmıştır. Liç başlığı altında toplamda 16 deney geçekleştirilmiştir.

Tez çalışmasının üçüncü başlığında ise çözeltideki demir ve diğer geçiş elementleri krom iyonlarından ayrılarak selektif olarak çöktürülmesi için proses şartları optimize edilmiştir. Bu noktada tez kapsamında çöktürücü ajan olarak oksalik asit tercih edilmesinin iki önemli sebebi bulunmaktadır. Birincisi, çözeltide bulunan demir sülfat oksalik asitle reaksiyona girmesinin ardından çubuk şeklinde çökelti oluşumuna sebep olurlar. Yapılan literatür incelemesi söz konusu çubukların geniş elektrot/elektrolit ara temas yüzeyine sebep vermesi ve Li^+ difüzyonunu kolaylaştırmaları sebebiyle anot olarak kullanıldıkları durumda toz numunelere nazaran daha üstün performans sergilediklerini ortaya koymuştur. Yine araştırmalar uygun pH ayarlaması ile oksalik asit kullanarak yapılan çöktürme işlemi sırasında demirin yanı sıra Ni, Co gibi diğer geçiş metallerinin de selektif olarak kazanılabilineceğini göstermiştir. Parametrelerin çökelme üzerindeki etkisini belirlemek için farklı sıcaklık, karıştırma hızı ve hacimce oksalik asit: liç çözeltisi oranının çöktürme verimine etkisi her seferinde bir parametreyi değiştirmek suretiyle incelenmiştir. Bu hedefle 4 adet deney yapılmıştır.

Tezin dördüncü aşamasında ise liç sonrası elde edilen çözeltiden seçici olarak geri kazanılan demir açısından zengin oksit tozları, değişik ısıl işlem parametrelerinde işlem görmüştür ve farklı özelliklere sahip oksit tozları üretilmiştir. Bu noktada ısıl işlem süresinin, sıcaklığının ve atmosferin etkisi her seferinde bir parametreyi değiştirmek suretiyle incelenmiştir. Toplamda 8 adet farklı özellikte demirce zengin metal oksit tozu elde edilmiştir.

Elde edilen bu 8 adet toz daha sonra yapısal, kimyasal ve morfolojik olarak karakterize edilmiştir. Tezin beşince başlığında ise söz konusu tozların LIB'de anot olarak kullanımları incelenmiştir ve tartışılmıştır.

Elde edilen tozlar kullanılarak aynı kompozisyona sahip çamurlardan laminasyon işlemi ile anotlar elde edilmiştir. Bu anotlar 1 mV-3 V aralığında 50 mA/g hızında test edildiğinde FeOxA2, FeOxA3, FeOxA6, FeO3003, FeO3002 ve FeO2153 kodlu numunelerin 100 çevrim sonunda grafitin teorik kapasiteisnden (372 mAsa/g) daha yüksek kapasite sergilediği görülmüştür. Demir oksalat numuneleri arasında, FeOxA3 en yüksek ilk deşarj kapasitesi değerine (1038.46 mAsa/g) ve 100 döngü boyunca en yüksek kapasiteye (673.08 mAsa/g) sahip olduğu belirlenmiştir. En yüksek kapasite korunum yüzdesine ise oksalat numuneleri arasında FeOxA2 numunesi sahiptir. Demir oksit numuneleri arasında en yüksek ilk deşarj kapasitesine ve 100 çevrimde en yüksek deşarj kapasitesinde FeO3002 kodlu numune ulaşmıştır. En yüksek kapasite korumuna da FeO205 kodlu numune sahiptir. Çevrimsel voltametri analizinde demir oksit ve demir oksalatın karakteristik pikleri bulunmuştur. Elektrokimyasal test sonuçları ile üretilen elektrotların Li ile gerçekleştirdiği reaksiyonlara ait mekanizmalar tartışılmıştır.

1. INTRODUCTION

Since the end of 18^{th} century, fossil fuels (such as coal, petroleum and natural gas) have been used for the reason of energy efficiency. As a result, carbon dioxide emission has been increased exponentially in the atmosphere for the last 2 centuries. This fact creates considereable concerns as CO_2 emission causes global climate change due to its greenhouse gas warming potential. As stated by Andres et al [1], there was an accelerated growth in carbon dioxide emission between 1751 and 1950. Moreover, the total cumulative carbon dioxide emission caused from fossil fuel was detected to be $250x10^9$ tonnes from 1751 to 1995 [1]. In this sense, people have been looking for alternative green energy systems.

Renewable energy systems attract attention because not only they are sustainable but also they provide clean energy. However, the discontinuity of generation (due to seasonal / day timing variations) is the biggest restriction for their ultimate use. Therefore, most of cases complex engineering design, planning and control should be done for using renewable energy sources effectively. Herein, efficient storage of such a clean energy represents the big challenge [2].

Herein secondary batteries become very important as they can store the energy when there is excess, and let the consumers use it when it is required. Among alternatives, lithium ion batteries have come into prominence by light weight, long shelf lives, high energy density and power density [3].

Shortly, a lithium ion battery contains four elements: separator, negative electrode, positive electrode and electrolyte. In 1990, Sony commercialized first lithium ion battery where $LiCoO_2$ and graphite were used as cathode and anode, respectively [4]. LIB technology has rapidly become widespread thanks to its superior properties. At this point, the high price of and the environmental damage caused by Co metal used in the cathode material's production lead scientists to look for alternative materials to replace lithium cobalt oxide. On the other hand, the client's need for higher energy

density induces a search for alternative materials to substitute graphite as the anode material.

In this thesis, by combining both principles of metallurgy and electrochemistry, iron based oxide powders have been fabricated. At this point, by using the domestic ferrochromium (FeCr) alloy as a starting material, it is aimed to reduce the damage to the environment during the production of the electrode's raw material and to support the economic development in the long-term run by enabling the use of a domestic product in a high value added application.

In the context of the thesis grinding, leaching, selective precipitation and calcination are used to fabricate iron-rich oxide powders as semi- products. After the structural, chemical and morphological characterizations of the semi-product, an electrode slurry is prepared. Finally lamination has been done by Dr. Blade to fabricate the anode material, final product. The anode material has been tested in CR2032 coin cells galvanostatically and potentiostatically.

The thesis has made of four steps. First step is to study the leaching mechanism and kinetic of FeCr alloy. In leaching process, sulfuric acid is used to etch transition metals (i.e. iron, chromium, and others like Ni,Co) from ferro chromium alloys. Taguchi experimental design $L_9\ 3^4$ approach is used to maximize the leaching efficiency of iron and chromium. Then leaching kinetic and mechanism have been discussed. In the second step, iron ions (along with Ni and Co) are selectively recovered by oxalic acid reaction in the shape of rods. Then, in the third step, resulting precipitate is calcinated differently to fabricate iron-rich oxalate and iron oxides rods of different structures. Finally, the use of those oxide rods as anode material for lithum ion batteries have been investigated based on their galvanostatic performances.

2. ORIGINALITY OF THIS WORK

Use of transition metal oxides as anode material becomes important as the conversion reaction enables the reaction of >1 Li^+ with the electrode material. Therefore, higher capacity could be achieved, eventually. Among alternatives, iron oxides attract attention due to their high abundance on earth, high theoretical capacity and environmentally friendly behaviour.

So far many researchers have fabricated iron oxides powders by means of solgel [5], hydrothermal reaction [6], solvothermal reaction [7], chemical precipitation [8] and spray pyrolysis [9], and they have tested their electrochemical performances when used as anode material in LIBs. The results have revealed that the intrinsically low electrical conductivity of iron oxides and the high volumetric changes that happen in the electrode upon cycling deterioriate the cycle performance of the electrode, resulting low first cycle coulombic efficiency and low capacity retention eventually.

In this thesis, different approaches have been proposed to fabricate electrode material. The originalities of the thesis lie in the material selection and designed fabrication process properties: The fact that an indigeneous ferrochromium has been used as the starting material represents the first originality of this study. Secondly, unlike to traditional methods a rotary evaporator has been used in leaching which changes the solid/liquid particle interaction upon leaching. And, thirdly as the ferrochromium contain trace amounts of nickel, manganese, cobalt, the iron oxide rods fabricated through the ferrochromium may have some amount of these transition metals in the structure, if the recovery process is designed for that purpose.

In this thesis, first in the open literature wt. %5 C contained ferrochromium has been leached with sulfuric acid and leaching parameters have been optimized to maximize the leaching efficiency of iron and chromium. Herein sulfuric acid is chosen as it inhibits hexavalent chromium formation in the leachate, which makes the process safer and environmentally friendly. Plus, sulfuric acid not only dissolves Fe and Cr but also other transition metals (Ni, Co, Mn, etc.) present in the precursor alloy. Then as a leaching reactor instead of using magnetic or mechanical stirrer a rotary evaporator

has been utilized. Such a change of the leaching system is expected to modify the leaching efficiency, eventually. And finally, by adjusting the precipitation parameters additional transition metals may be precipitated along with iron ions in order to create some electron conductive pathways in the rods structured oxide particles. Consequently, first in the open literature, not only iron-rich oxides but also the use of iron-rich oxalate rods have been fabricated from the indigeneous FeCr alloy and their possible uses as anode material in LIBs have been evaluated within the content of this thesis.

3. LITERATURE REVIEW

Although the first usage of electrochemical energy storage devices (or batteries) are stated as belonging to Persian civilizations depending on archaeological findings in Bagdad, the firstly accepted works on electrochemical batteries belong to Galvani and Volta from 18th century [10]. Many scientists have been working under inspiration of Galvani words as "animal electricity" [11].

Since 18th century, many types of rechargeable batteries that have been developed over 3 centuries, have been reported, as seen in Table 3.1.

Table 3.1: Types of rechargeable batteries [12].

Storage system	Energy Density (Wh/g)	Theoretical Capacity (Ah/kg)	Cell Voltage (V)
Lead Acid	30-50	83	2
Ni-Cd	45-80	162	1.2
NiMH	60-120	172	1.2
Li-ion (LiMnO2/graphite)	100- 150	104	3.7
Li-ion (LiCoO2/graphite)	150- 250	158	3.6

Among alternatives, lithium ion batteries (LIBs) offer higher energy and power densities compared to other rechargeable batteries [3]. Moreover, compared to lead and cadmium containing storage devices, lithium ion battery has a better impact on the environment: high operating voltage (3.7 V), high gravimetric and volumetric densities, no memory effect, low self-discharge rate and operation in wide range of temperature [13]. Moreover, lithium ion batteries have no memory effect like nickel cadmium batteries and has a very long shelf life due to low discharge rate of the cell.

3.1 Lithium Ion Batteries

Lithium battery as a primary battery was firstly studied at Bell's Laboratories in 1960 with graphite anode [14]. After that, Sony contributed the first commercial lithium ion battery in 1990 [4]. Following its entrance into the market, LIB's share rapidly increased due to its superiorities compared to NiCd and acid Pb batteries [13]. Such privileges caused them to be used in different scales from mobile phones to portable electronic devices, electric vehicles to gride applications [15-16].

Literature survey reveals that studies on LIBs have increased exponentially from 1990 to 2019 (Fig.3.1.). The data collected from Scopus, Science Direct and Web of Science.

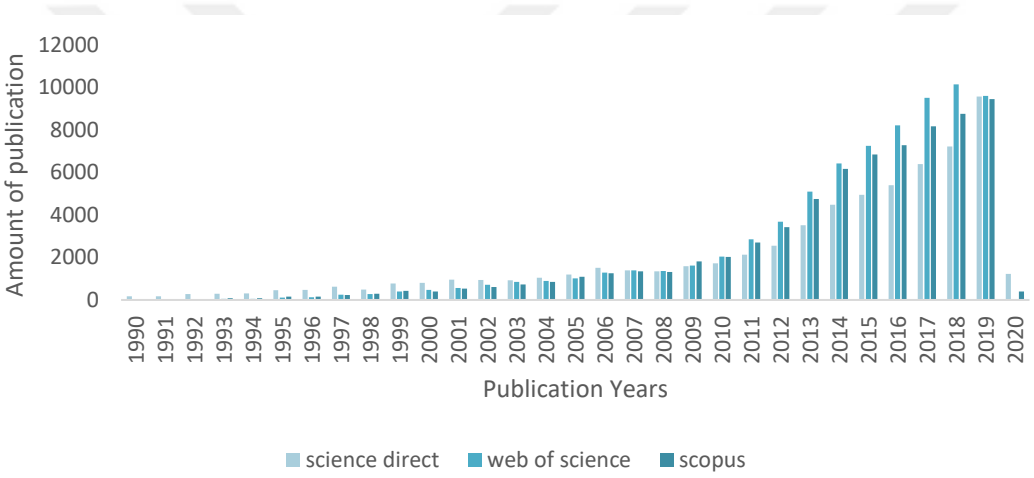

Figure 3.1: Amount of publication about LIBs per years by constructing from different database.

3.2 Operational Procedure of Lithium Ion Batteries

Lithium ion batteries being type of secondary batteries can be charged/discharged reversibly over cycles (Figure 3.2.a-b). During charge reaction (Figure 3.2.a), Li^+ ions get out from the cathode and pass through the electrolyte to get into the anode. In the same time, electrons emerged from the cathode simultaneously move to the anode by the help of external electric circuit. Then upon discharging, (Figure 3.2.b) Li^+ ions are moved from the anode, pass through the electrolyte and get into the cathode material. To neutralize the reactions, electrons that are moving from the anode get into the cathode, reversibly, by the help of the external electrical circuit [17].

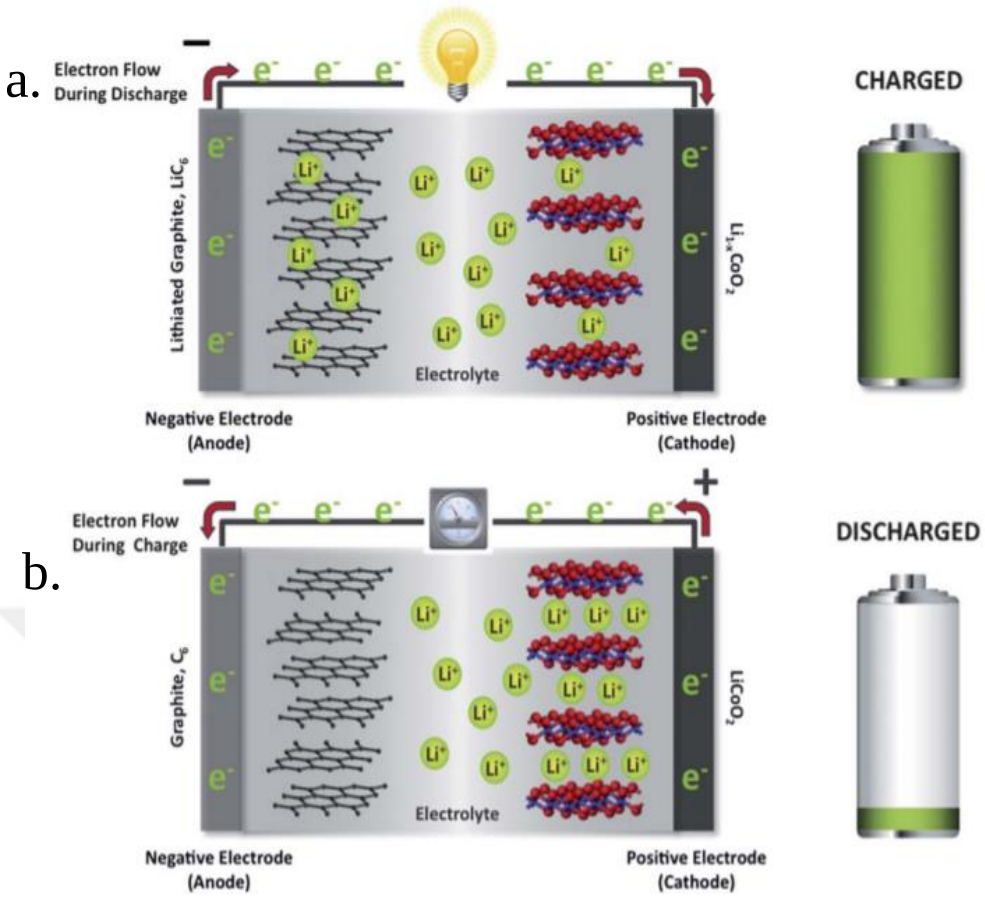

Figure 3.2: Illustration of working reaction lithium ion battery **a)** charge **b)** discharge [17].

3.3 Components of LIBs

A lithium ion battery simply consists of 4 component; separator, electrolyte, positive and negative electrode

3.3.1 Separator

The main contribution of the separator is to prevent any short cut between the electrodes. Therefore, the properties expected from the separator can be listed as follows: being chemically stable during the cycling test, easily getting wet after being in contact with the electrolyte, having high decomposition temperature, low electrical conductivity, and homogeneous por diameters to selectively pass Li ions in cycling [18]. Common type of separators and their properties are given in Table 3.2.

Table 3.2: Lists of separators producer, materials and design [19].

Producer	Materials	Design
Celgrad LLC	PE, PP and PP/PE/PP	Uniaxiallly oriented
Ashai Kasei Chemicals	Polyolefin and ceramic-filled polyolefin	Biaxiallly oriented
Entek Membranes	ceramic-filled UHMWPE	Biaxiallly oriented
SK Energy	PE	Biaxiallly oriented
Ube Industries	PP/PE/PP	Uniaxiallly oriented
ExxonMobil/Tonen	PE and PE/PP mixture	Biaxiallly oriented

3.3.2 Electrolyte

Electrolyte being a lithium ion transferring media, is present between negative and positive electrodes. Electrolyte could be in a solid or in a liquid state. Mainly, liquid electrolyte is a mixture of solvent and salts. Common expectations from the electrolyte salts are high Li^+ transport rate for obtaining high power, high solubility, stability and non-corrode current collector [20]. Common types of lithium salts are lithium perchlorate ($LiClO_4$), lithium hexafluoroarsenate ($LiAsF_6$), Lithium hexafluorophosphate ($LiPF_6$), lithium tetrafluoroboarte ($LiBF_6$) and lithium trifluoromethanesulfonate ($LiSO_3CF_3$) [21-22]. $LiPF_6$ is the most soluble salt compared to others [20]. Commonly used solvents could be exemplified with ethylene carbonate (EC), propylene carbonate (PC), dimethyl carbonate (DMC), ethyl methyl carbonate (EMC) and diethyl carbonate (DEC) [23].The common expectations from the organic solvents can be summarized as follows high electrolytic conductivity, safety and chemical stability [20]. In case of this thesis, a mixture of EC:DMC is chosen as the electrolyte. EC:DMC composition is best option for disabling oxidation of $LiPF_6$ compared to other candidate organic solution [25]. Moreover, $LiPF_6$ EC:DMC electrolytes have stability in wide voltage range [26].

3.3.3 Negative electrode

The negative electrodes accommodate Li ions that are extruded from the cathode. The common expectations from the anode material could be summarized as follows [29].

- Having low atomic weight,
- Having high structural stability, electrical conductivity,
- Having low lithiation voltage
- Having affordable price
- Being environmentally friendly

Upto now different materials have been tested as anode materials for LIBs. The results reveal that Li reaction mechanism with an anode material could be classified as insertion, alloying and conversion reaction.

In insertion, lithium can easily be inserted/deinserted to anode interstitial sites. The common example of this mechanism is $Li_4Ti_5O_{12}$ anode material as a titanate material. In example of $Li_4Ti_5O_{12}$, Lithium is inserted into the tetrahedral sites of $Li_4Ti_5O_{12}$ and $Li_7Ti_5O_{12}$ is formed consequently [31]. $Li_4Ti_5O_{12}$ is a promising anode material because its lithiation voltage is high enough to avoid Li dendrite and solid electrolyte interface formation on the electrode surface. However, its low theoretical capacity (175 mAh/g) restricts its wide use.

In alloying, metals or alloys could make unique compound with lithium. Table 3.4 depicts some examples which form alloys following their reactions with Li.

Table 3.4: Alloying type anodes and properties [32-33].

Material	**Potential vs Li^+ (V)**	**Theoretical specific capacity (mAh/g)**	**Product of reaction with lithium**
C	0.05	372	LiC_6
Si	0.4	4200	$Li_{4.4}Si$
Sn	0.6	994	$Li_{4.4}Sn$
Ge	0.25	1100	$GeLi_x$

Although, in most of the cases alloying mechanism leads to high discharge capacity, the capacity retention is very low due to the weak structural stability of the anode material.

And in 2000, Poziot et al have discovered conversion type reaction mechanism [34]. Basically, a reversible displacement reaction occurs over cycling between lithium and the nanosized active material. The lihitation reaction between the active material and lithium could be described as Equation 3.1 [35]. (3.1)

$$M_aX_b + (b.n)Li^+ + (b.n)e^- \leftrightarrow aM + bLi_nX \quad (3.1)$$

M and X represent metal or mix of metal and an anion such as halogen, nitrogen, oxide, oxalate sulphate and etc., respectively. Common examples for conversion anodes could be seen in Table 3.5.

In general, conversation type anodes have advantages due to cost, safety and high capacity [35]. However, the process may have some problems such as low electronic conductivity, high volume change and relatively high lithiation.

Zhang et al [8] have stated that metal oxides have the highest theoretical capacity and safety among other anode active materials in case of converisation type [8].

Table 3.5: Conversion type anodes and properties [36-39].

Material	**Potential vs Li^+ (V)**	**Theoretical specific capacity (mAh/g)**	**Products of reaction with lithium**
CuO	2.24	673.9	$Cu+Li_2O$
Fe_3N	1.19	443	$Fe+Li_3N$
CoC_2O_4	0.58	364	$Co+Li_2C_2O_4$
CoO	1.8	715.3	$Co+ Li_2O$

3.3.4 Positive electrode

Positive electrode (or cathode) represents the source of lithium in the coin cell. 1D (olivine), 2D (layered), and 3D (spinel) structured cathode materials have been fabricated and tested [26]. Common expectations from a cathode could be stated as having reversible reaction with lithium, high electrical and ionic conductivity, being chemically stable against the electrolyte, economic and environmental friendly [27].

In Table 3.3, the most commonly used positive electrode materials and their capacities are presented.

Table 3.3: Positive electrode examples and properties [28].

Positive Electrode Type	Structure	Specific Capacity (mAh/g)	Midpoint voltage at C/20
$LiCoO_2$	Ordered rock salt	140-155	3.9
$LiNi_{0.8}Co_{0.15}Al_{0.05}O_2$	Ordered rock salt	200	3.73
$LiNi_{1-x-y}Co_xMn_yO_2$	Ordered rock salt	140-180	3.8
$LiMnO_2$	Spinel	100-120	4.05
$LiFePO_4$	Olivine	160	4.05

3.3.4.1 Transition metal oxide and iron oxide anodes

Poizot et al have explained the lithiation mechanism and revealed that upon lithiation nanosized transition metal oxide particles are disintegrated leading the formation of nanoscale metal particles (1 ± 5 nanometer in size) in Li_2O matrix [34]. In the same study, it is also mentioned that the voltage-capacity curves of the transition metal oxides vs Li (MO / Li (M: Ni, Co, Fe)) are all very similar and they all reveal changes in curvature shape after the 1st cycle. They have also [34] stated that there is an optimum particle size for each metal oxide system where the metal particles will give the best electrochemical performance. In Table 3.6, types of transition metal oxides, their theoretical capacities and calculated lihitation voltages are listed. [40-41]

Table 3.6: Theoretical capacities and calculated lithitation voltage of TMO.

Material	Fe_3O_4	FeO	Fe_2O_3	Cr_2O_3	CoO	MnO	Mn_3O_4	Mn_2O_3	NiO
Theoretical capacity (mAh/g)	926.1	746.1	1007	1058	715.3	755.6	937.1	1018.6	717.6
Calculated Lihitation Voltage (V)	1.61	1.65	1.64	1.13	1.82	1.02	1.26	1.40	1.83

Following the explanation of Poizot et al, studies on transition metal oxide anodes have been exponentially increased over years (Figure 3.3).

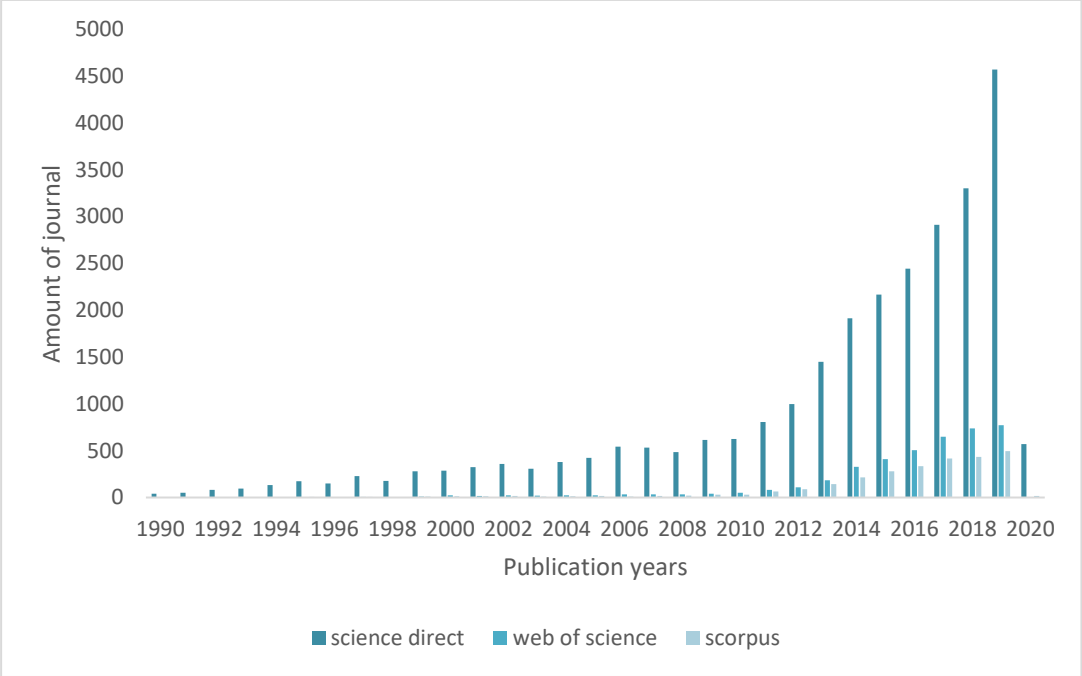

Figure 3.3: Amount of publications about metal oxide anodes year by year.

Among the alternatives, iron oxides become attractive due to their low fabrication cost, high abundance on earth crust and environmentally friendly behaviour. Figure 3.4. depicts that the number of the articles published on iron oxide anode material has increased exponentially over years. Plus, the fact that iron has many oxidation states, there are four different types of iron oxides available as electrode materials: Magnetite, hematite, maghematite and wustite. Iron oxide could be produced by different methods, through various precursors [8]. These materials perform different electrochemical behaviours as summarized in Table 3.6. The different performances are related to their characteristic lithiation reactions (Equations 3.2-3.4) [42-44];

$$Fe_2O_3 + 6Li^+ + 6e^- \leftrightarrow 3Li_2O + 2Fe \quad (3.2)$$

$$Fe_3O_4 + 8Li^+ + 8e^- \leftrightarrow 4Li_2O + 3Fe \quad (3.3)$$

$$FeO + 6Li + +2e- \leftrightarrow Li2O + Fe \quad (3.4)$$

So far, different methods (hydrothermal [42], solvothermal [45], elctrospinning [46], thermal decomposition [47] and precipitation [44] etc.) have been used to fabricate

iron oxide electrodes. Table 3.7, summarizes the properties and the performances of the iron oxide anode materials stated in the literature.

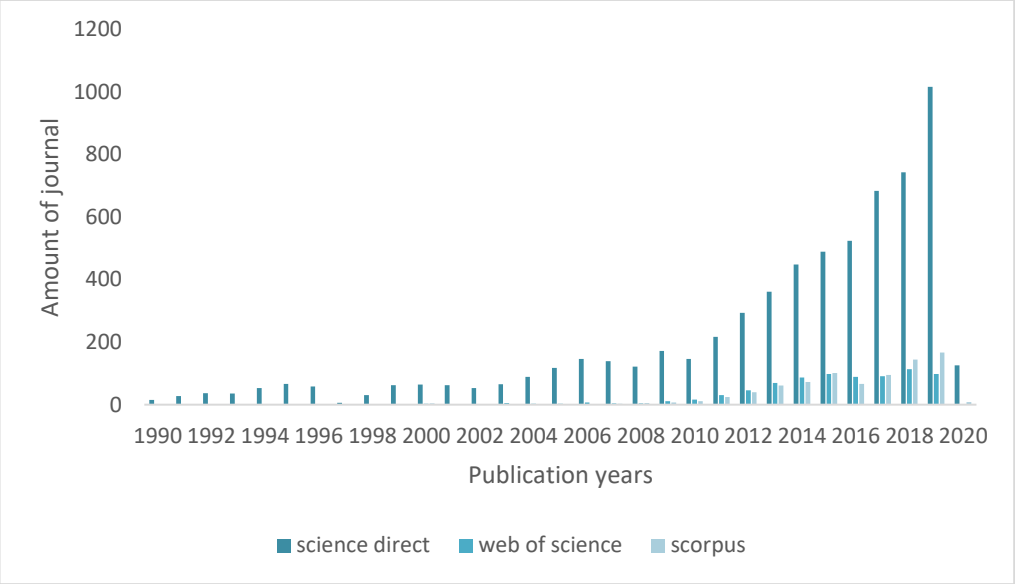

Figure 3.4: Amount of publications about iron oxide anodes year by year.

Among them, the study of Larcher et al [48] stand out as in this research they have revealed that the micron (M-Fe_2O_3) and nano sized (N-Fe_2O_3) iron oxide particles have different intercalation charcteristics. Moreover, experimentally they have demonstrated that the use of N-Fe_2O_3 performs better than M-Fe_2O_3. According to this work [48], M-Fe_2O_3 and N- Fe_2O_3 could react with 7.2 and 8.4 mol Li and show 1200 and 1400 mAh/g 1st discharge capacity, respectively. Unlike to N-Fe_2O_3 where multiple plateaus are noted showing the biphasic transformation, during the discharge of M-Fe_2O_3, nearly no Li insertion is noted for M-Fe_2O_3 from 3 V to 1 V. When reaching 1 V, there is an insertion of 6 mol Li to structure. From 1 V to 0 V, 1 mol Li is intercalated into the structure, additionally. It is also argued in this study that the reduction reaction of α-Fe_2O_3 is reversible due to the high contact area between Li_2O and Fe. Moreover, Larcher et al state that by using N-Fe_2O_3 and M-Fe_2O_3 the reaction with Li takes place following Eq. 3.5-3.6, respecitvely [48].

$$N - Fe_2O_3 \xrightarrow{monophasic} \alpha - LiFe_2O_3 \xrightarrow{biphasic} cubic\ Li_2Fe_2O_3 \xrightarrow{biphasic} Fe^0 + Li_2O \quad (3.5)$$

$$M - Fe_2O_3 \xrightarrow{monophasic} \alpha - Li_{0.03}Fe_2O_3 \xrightarrow{biphasic} cubic\ Li_2Fe_2O_3 \xrightarrow{biphasic} Fe^0 + Li_2O \quad (3.6)$$

Table 3.7: Example of iron oxide anodes according to literature.

Cyrstal structure	Fabrication method	Powder properties	1st discharge capacities	Final discharge capacity (cycle no)	Test conditions
Magnetite [42]	Hydrothermal	Spherical with 25 nm diameter	740 mAh/g	270.14 mAh/g (15.)	25 mA/g 1mV-3V
Hematite [44]	Precipitation	1 μm flower-like	1700 mAh/g	1000 mAh/g (10.)	100 mA/g 1mV-3V
Hematite [51]	Hydrothermal	200 nm nanorod	1303 mAh/g	456 mAh/g (100.)	0.1 C 1mV-3V
Hematite [6]	Hydrothermal	200 nm Nanospheres	1248.1 mAh/g	795.8 mAh/g (30.)	20 mA/g 1mV-3V
Maghemate [47]	Thermal decomposition	43 nm plates	1284 mAh/g	538 mAh/g (50.)	50 mA/g 1mV-3V
Hematite [52]	Thermal decomposition	Hollow spheres with 2 μm diameter	905 mAh/g	419 mAh/g (50.)	50 mA/g 5 mV-3V
Hematite [46]	Electrospun and decomposition	100-250 nm fibers	597.12 mAh/g	256 mAh/g (50.)	50 mA/g 1mV-3V
Hematite [45]	solvothermal	100 nm particles	678 mAh/g	120 mAh/g (100.)	0.1 C 1mV-3V

Then, Wang et al. have underlined the importance of the morphology on the electrochemical performance of the electrode material [49]. Nuli et al have been working on different iron oxide morphologies in nanosize [6]. Different morphologies shows different resistance properties as ordered from the highest resistance value to the lowest resistance value: nanocuboids, nanosheets and nanowires. Wang has reported resemblances with the research outputs made by Nuli et al. [6]. Chun et al [50] explain the reactions of 50 nm sized hematite nanoflakes anode material with lithium through XRD analysis' results. They claim that the peaks related to the formation of $Li_2Fe_3O_4$ are distinguished in XRD. The fact that there is no peak belonging to Li_2O in the XRD data obtained around ≈0.9V (against Li) reveal that Li_2O is amorphous in the conditions when the intermediate phase ($Li_2Fe_3O_4$) occurs. In the galvanostatic test, it is expected that Li, which enters in the anode structure with the further decrease in the potential, will completely disrupt Fe_2O_3 and causes the formation of Fe atoms distributed in the Li_2O matrix [50], eventually (Equation 3.7).

Moreover, electrochemical analyses' results prove that nanostructuring and doping could be useful to increase the cycling performance of transition metal oxide anode material because doping may have a positive effect on the electrical conductivity of anode. [53-55]. Mai et al [53] have been sustaining Li^+ diffusion by doping Co to NiO. Shi et al [54] have demonstrated Cr doping enhancing electronic conductivity of $LiFePO_4$. Ni doping has been investigated by Lin et al. [55], they achieve better rate performance in case of $Li_4Ti_5O_{14}$.

$$6Li + 3Fe_2O_3 \rightarrow 2\ Li_2Fe_3O_4\ +\ Li_2O \tag{3.7}$$

3.3.4.2 Transition metal oxalates and iron oxalate anodes

Recent studies have highlighted the possible use of metal oxalates as anode material for LIBs [56]. Figure 3.5 depicts that studies on metal oxalates have increased over years exponentially. Yeoh et al have mentioned about their potentials to create opportunity for sustainable materials synthesis and materials [56]. Their lithitation reaction is given in Eq. 3.8 [56];

$$MC_xO_y + 2Li^+ \leftrightarrow Li_2C_xO_y + M \tag{3.8}$$

M refers metal such as nickel, iron, manganese and cobalt. In this reaction, oxalate complex is believed to keep structurally stable over cycling. Leon et al [57] have been

sythesized MnC_2O_4 nanoribbon by reverse micelles method and they have achieved 350 mAh/g over 70 cycle at 2 C. In case of cobalt, Aragon et al. [58] stated that CoC_2O_4 nanoribbons that have been produced by reverse micelles and delivered 550 mAh/g over 50 cycle at 2 C rate. Then, Lopez et al [59] have fabricated NiC_2O_4 nanoribbons by reverse micelles and achieved 240 mAh/g over 70 cycle at 2 C rate. In last example, FeC_2O_4 nanoribbons have been synthesised by reverse micelles and performed 480 mAh/g over 70 cycles at 2 C rate [60].

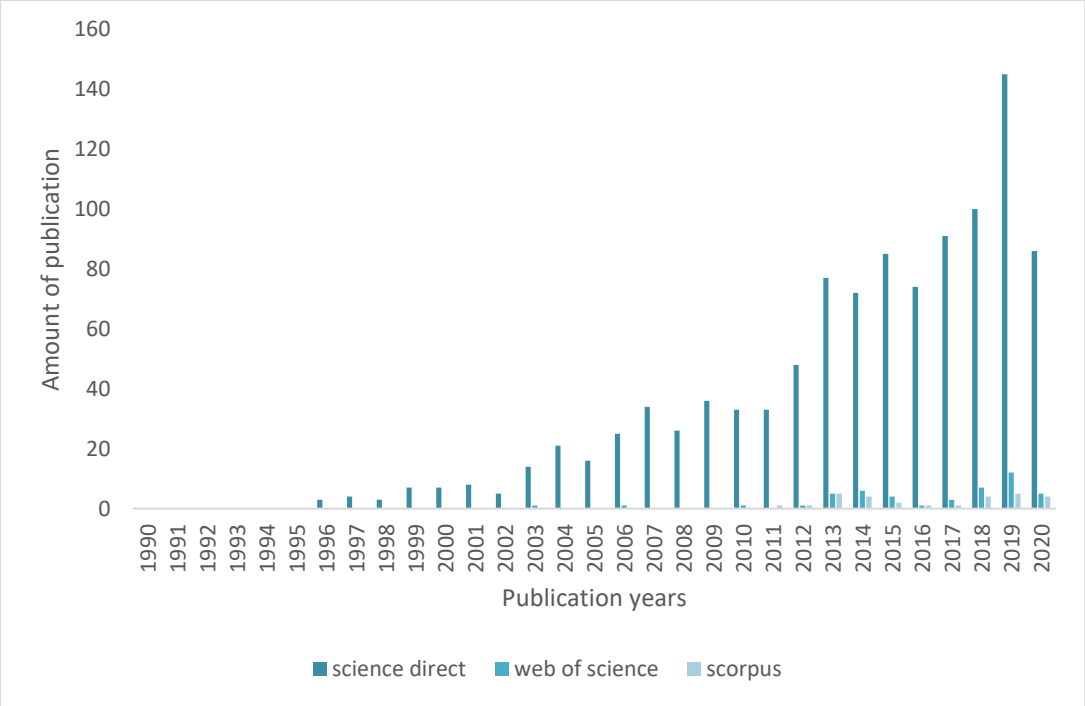

Figure 3.5: Amount of publications about metal oxalate anodes year by year.

Among all different metals, iron oxalates become prominent. Ang et al. [61] have described the reactions of iron oxalates with Li by Equation 3.9. Accordingly, they stated upon lithiation the crystal structure of the oxalate particles is disintegrated and iron atoms are dispersed in lithium oxalate. Oh et al. [62], on the other hand, have stated that oxalate structures react alternately with Li like metal oxide structures but form $Li2C_2O_4$ unlike metal oxides (Li_2O occurs in the conversion reaction of metal oxides) [63]. In the study of Oh, however, it is clearly stated that the answer to the question of why the capacity obtained at the end of this reaction is higher than the theoretical value is still being investigated.

Table 3.8 summarizes different iron oxalates performances reported in the open literature.

Table 3.8: Iron oxalate anode example according to literature.

Powder properties	Fabrication method	1st discharge capacities	Final discharge capacity (cycle no)	Test conditions
Nanotube FeOx hydrate [63]	Precipitation	1730 mAh/g	340 mAh/g (100.)	0.5 C 1 mV- 2V
Nanorod FeOx hydrate [63]	Precipitation	1340 mAh/g	Dead (90.)	0.5 C 1 mV- 2V
Cocoon shape FeOx [61]	Precipitation	825 mAh/g	438 mAh/g (100.)	11C 1 mV-3V
Rod shape FeOx [61]	Precipitation	906 mAh/g	764 mAh/g (100.)	3C 1 mV-3V
Nanorod α@β-FeOx [64]	Solvothermal	1137 mAh/g	746.46 mAh/g (200.)	5 A/g 1 mV-3 V
Nanoribbon FeOx [65]	Reverse micelle	900 mAh/g	600 mAh/g (70.)	2 C 1 mV-2V

$$FeC_2O_4 + 2Li^+ + 2e^- \rightarrow Fe + Li_2C_2O_4 \quad (3.9)$$

According to Figure 3.6, amount of publication on iron oxalate anodes could be seen. There is an increasing trend for iron oxalate publication.

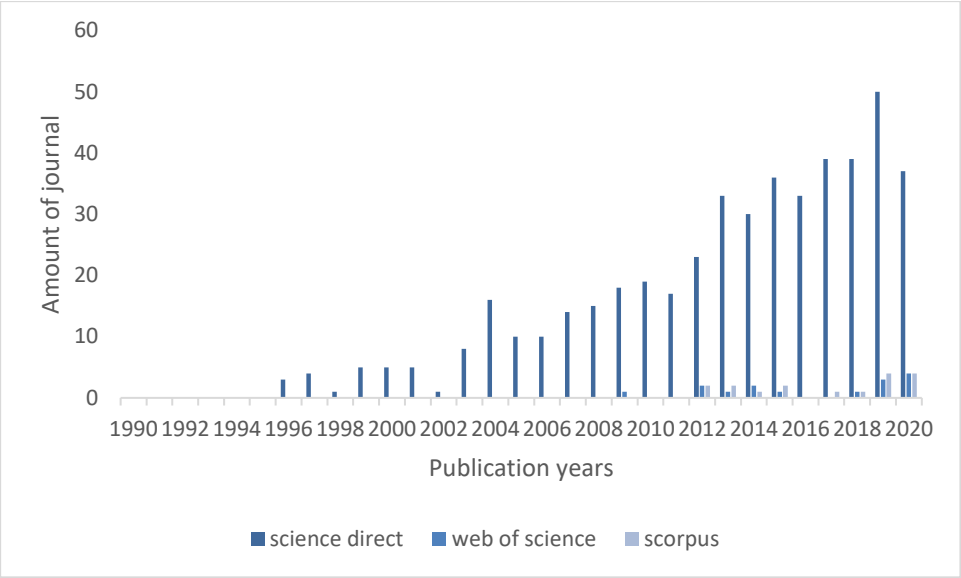

Figure 3.6: Amount of publications about iron oxalate anodes year by year.

3.4 Iron Based Material Production

As mentioned before, iron abundance is higher than other transition metals [6]. Moreover iron based materials have been used in many field such as defence, biomedical, sensors, batteries, construction and etc. Upto now, spray pyrolysis, sol-gel, hydrothermal, precipitation-calcination route and mechanical ways have been used to produce iron based oxide particles [66-70]. By the help of these methods, variety of iron oxide in different dimensions and shapes have been fabricated [66-70]. It is already kown that precipitation and calcination methods come to prominence when considering green manufacturing and energy consumption subjects.

In this thesis work, iron oxides and iron oxalates have been produced by a combination of precipitation-calcination processes where the precursor is the domestic ferro chromium alloy. In this perspective, ferro alloys are considered to be good candidates as they all contain high amount of iron in their structure. Moreover, the existence of trace amount of other transition metals could have dopping effects onto the iron oxide particles.

3.4.1 Ferro alloys in Turkey

In the thesis in order to reduce carbon footprint caused by transportation and mining FeCr alloy has been chosen as the precursor material. Knowing that high purity precursors have high expence and low grade precursors need purification processes, ferro alloys are believed to be a good candidate to fabricate iron based oxide materials.

As stated by Aydın et al [71], high carbon contained ferrochromium is the highest amount of ferroalloy produced in Turkey. The map that shows the places of ferrochromium producers is given in Figure 3.7 In the thesis we have used ferrochromium that have been fabricated in Eti Krom AŞ.

Figure 3.7: Map and producer list of ferrochromium [72].

3.4.2 Iron leaching

Leaching has been applied to recover the iron (Fe) and trace amount of transition metals (Mn, Ni, Co etc) in the ferrochromium into solution for using as starting material So far, many groups have optimized the leaching's parameters of transition metals and results revealed that temperature, solid/liquid ratio, temperature, duration and stirring rate affect the leaching efficiency.

Mohanty et al leached a material that has 24% Fe in its structure and reported that the highest iron gain (83% yield) is achieved when the electrolyte has 1.93 M sulphuric acid compared to other leaching medias such as acids (HNO_3, HCl and H_2SO_4), base (NaOH) and salt mixture ($CuCl_2$ with NaCl) [73]. Then, Tzeferis et al [74] have used organic acids (such as oxalic acid, citric acid), sulphuric acid and their mixtures to leach lateritic nickel ore containing iron, the results prove that sulphuric acid can leach iron with higher efficiency compared to organic acids and acid mixtures. Afterwards, Ige et al [75] have worked with tantalum ore and determine that iron leaching efficiency is increased with increasing sulphuric acid molarity in leaching experiments

performed at constant variables. In the same study, Ige et al have also reported that the decreasing particle size of the starting material is increasing leaching efficiency. Further, El bar et al [76] have stated that 30% Fe recovery is obtained when the waste containing 10% iron is leached in 2 hours with 2 M sulphuric acid at 85˚C. In the study of Liu et al [77] they have leached a chromite ore by using a magnetic mixer. The highest efficiency for iron recovery has been achieved when the leaching has been done at 138˚C and 60 minutes. In the study of El Bar et al. [78] where copper sulphate concentrate is leached with 2 M sulphuric acid, it is explained that the highest iron gain was achieved at 2 hours, 65˚C and 100 rpm. In the study performed by Zhao et al. [79] where chromite ore is leached by using a mechanical mixer, they state that leaching efficiency is increased with decreasing particle size. Within the scope of the same study, the effect of leaching temperature on yield is also investigated, and it has been explained that the yield increased up to 180˚C, but after 180˚C the yield decreased with the precipitation of sulphated compounds [79]. When the research on the leaching of ferrochromium alloys with low carbon (wt. <0.1%) content with sulphuric acid is examined, it is more than 90% of chromium and iron are found to be leached out as a result of the reaction performed in 6 hours at a volumetric solid: liquid ratio of 1: 3 at 90˚C by a mechanical stirrer. It is also mentioned in this study that the remaining leach residue does not contain hexavalent chromium and that this residue can be used in ferrochrome production again [80-84]. However, the molarity of the solution used in this study is not specified.

Liu et al. [80] have stated that the reactions that occurred during the leaching of ferrochromium with sulphuric acid are as follows (Equation 3.10-3.15).

$$3H_2SO_4 + 2Cr \rightarrow Cr_2(SO_4)_3 + 3H_2 \quad (3.10)$$

$$H_2SO_4 + Fe \rightarrow FeSO_4 + H_2 \quad (3.11)$$

$$H_2SO_4 + Mn \rightarrow MnSO_4 + H_2 \quad (3.12)$$

$$H_2SO_4 + Co \rightarrow CoSO_4 + H_2 \quad (3.13)$$

$$H_2SO_4 + Ni \rightarrow NiSO_4 + H_2 \quad (3.14)$$

$$4H_2SO_4 + Fe_3O_4 \rightarrow FeSO_4 + Fe_2(SO_4)_3 + 4H_2O \quad (3.15)$$

3.4.3 Iron extraction from solution

The results of the literature review for the selective recovery of iron from chromium rich solution show that the selective precipitation step would be the most environmentally friendly, economical and efficient process in this context. The work where Liu et al. [85] have recovered iron, manganese, cobalt and nickel from the leaching solution of low C contained FeCr alloy stand out. In this study, oxalic acid is chosen as the precipitating agent. In order to selectively recove Fe along with Ni, Co and Mn the pH of the leachate has been adjusted to 3 with the help of 25% ammonium solution. The results prove that iron and other transition metals (Ni, Co, Mn) precipitate as oxalates; where as chromium ions remain in the leachate. In this study, the change in precipitation efficiency of the metals (Fe, Co, Ni, Mn, Co, Cr) upon pH is given graphically: the chromium begins to settle after pH 3.5 as the chromium oxalate compound and the iron recovery efficiency decreases when pH becomes higher than 3.5. In 2011, a similar approach was demonstrated by Chen et al. [86]. They have show that iron oxalate has been fabricated from the sulphate solution when pH has been adjusted to 3 by using NaOH solution (containing wt. 10% NaOH).

Apart from oxalic acid, it is possible to extract iron ions from the leach solution with the help of different precipitating agents (Di-(2-ethylhexal) phosphoric acid [87-88], ethylene diamine tetra acetic acid [89]). However, because of the high cost of chemicals and / or the fact that the agents are not able to selectively remove different transition metals from the solution, they are not preferred within this thesis study. Furthermore, as iron oxalate considered as a promising anode material, oxalate precipitation has been chosen in this work.

3.4.4 Thermal treatments for iron oxalate hydrate as precursor

It has been stated in the literature that iron oxide structures (hematite, wustite, maghemite, magnetite) in different atomic sequence can be obtained following a heat treatment in different atmosphere and conditions [90-91].

Tsyrnorechki et al. [92] have produced maghemite by calcination of iron oxalate hydrate at an atmosphere containing 4-5% oxygen for 24 hours at 350˚C. Gopalakrishnan et al. [93] stated that iron oxalate hydrate could be transformed maghemite when being processed in an air flow of 200˚C. Ang et al. reported that

hematite could be obtained by calcination of iron oxalate hydrate at 270˚C in air atmosphere [61].

In addition, Tahildades et al. [93] have stated that they made heat treatment to the iron oxalate powder for 2 hours at 350˚C in an atmosphere containing 90% N_2 and 10% H_2, and then at an atmosphere containing 100% N_2 for 1 hour at 480˚C. The structural characterization reveals that magnetite has been fabricated eventually. Zhou et al. [94] have stated that by processing iron oxalate powder at 400˚C in N_2 atmosphere for 2 hours, they have produced maghematite. On the other hand, Hermankova et al. [95] have stated that they obtained the structure containing magnetite and metallic iron by processing the iron oxalate hydrate as starting material for 2 hours in Ar atmosphere at 400˚C.

When all these articles mentioned above are examined in detail, it is seen that the heat treatment temperature of the studies is selected based on the results of TGA/DTA. Similarly, within the scope of this thesis, temperature of different heat treatment processes have been chosen by using the results of the TGA/DTA analyses.

3.5 Taguchi Method and Principle

This method is established by Dr. Genish Taguchi who had expressive contribution in case of Quality Engineering. Taguchi declared that his methodology depends on several philosophies. Unlike to the full factorial experimental design, Taguchi method simply offers lower amount of experimental trial by benefitting experience and wisdom of researcher and literature research [96]. Furthermore, minimizing the effect of uncontrolled parameters (‘random noise’) over the controllable factors (‘operator’s signal’), Taguchi approachs offer formulations to maximize signal/noise ratio (S/N) in the design. This formula being independent of the target value of the experiment, always consistent with the Taguchi’s quality objective. Consequently, Taguchi always supplies robust design solutions [97].

In this thesis study, Taguchi orthogonal method is applied for different purposes. First an optimization of ball miling has been done to obtain ferrochromium with minimum grain size by “smaller is better” approach. Then, an optimization of leaching parameters have been done to maximize the leaching effeiciency of iron and chromium via “larger is better” approach.

4. EXPERIMENTAL STUDIES

Experimental studies could be divided into four main group: ferrochromium preparation, leaching, powder production and characterizations. Flow chart for experimental studies is seen in Figure 4.1.

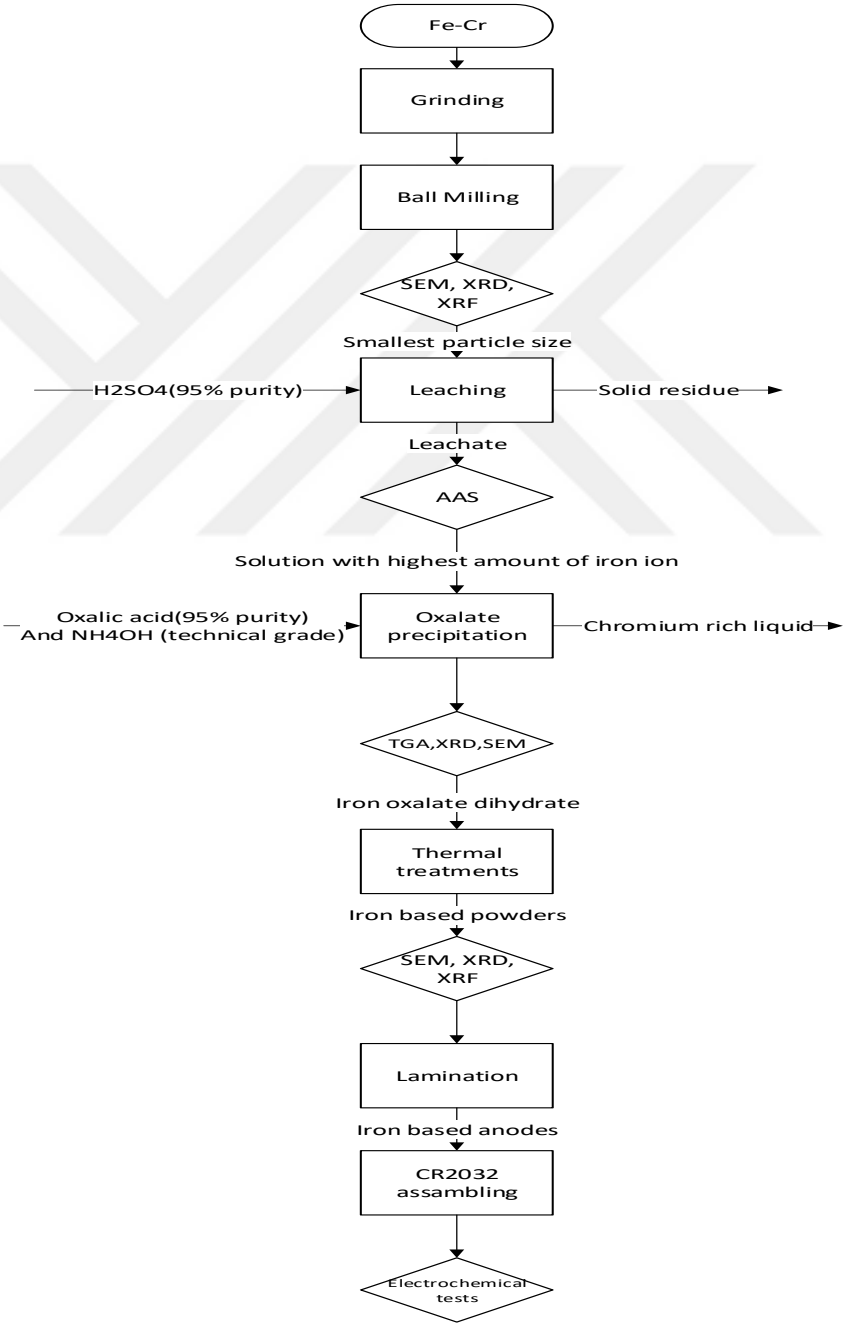

Figure 4.1: Flow chart of experimental studies.

4.1 Materials

For milling, Turkish high carbon ferrochromium alloy is supplied from Eti Krom A.Ş., Elazığ. Ethanol (1.00983.2511) are purchased from Merck.

Leaching has been made with Merck quality sulfuric acid (1.00713.2500). For selective iron precipitation. oxalic acid is purchased from Isolab (LS096211DAGW). Deionized water and NH_4OH are of analytical grade.

To fabricate eletrode, polyvinylidene fluoride (PVDF) and conductive carbon have been purchased as technical grade for slurry formation. N-Methyl-2-pyrrolidone (NMP) is Merck quality (8.06072.2500). Highly pure Copper (>99.95%) foil has been chosen with 10 μm thickness.

4.2 Ferrochromium Preparation

Firstly, ferrochromium chunks are hammered then ground to achieve particle size under 100 μm by using the grinding machine (Siebtechnik) given in Figure 4.2.a. Then, the ground particles are planetary ball-milled by Retsch Pm 100 (Figure 4.2.b.), to achieve the smallest particle size by using Taguchi orthogonal method. 3 parameters with 2 levels ($L_4 2^3$) have been optimized. In ball milling, zirconia jar and zirconia balls are used to prevent any contamination.

Figure 4.2: a) Grinding machine [98] b) Planetary ball mill.

The investigated parameters are duration (1 and 4 hours), rotation speed (235 and 500 rpm) and ball to powder ratio (BPR) in weight (4:1 and 10:1). The experiments design by Taguchi approach (with parameter's levels) are given in Table 4.1. In each

experiment, 5 ml ethanol is used as dispersant and 5 mm diameter zirconia ball are used to grind.

Table 4.1: Constructed Taguchi experiment for ball milling of ferrochromium

Parameters	**Units**	**1st level**	**2nd level**
Durartion	Hour	1	4
Rotation speed	RPM	235	450
BPR	wt/wt	1:4	1:10

Milled ferrochromium is cleansed by deionized water. Cleansing is made for removal of water soluble inclusion before leaching and performed with Velp Scientific LH magnetic stirrer. 10:1 volumetric ratio of powder: d.w. has been chosen. Powders are cleansed at 60˚C with 500 rpm. The cleansed powder is dried in air atmosphere at 100˚C for 12 hours

4.3 Leaching

All leaching experiments have been done in a rotary evaporator (Figure 4.3) (Buchi Rotavapor® R-300). There has been no published article/report found in literature where the rotary evaporator has been used for such purpose. In the first step of leaching study, nine experiments are designed to optimize the leaching process parameters via Taguchi orthogonal array method (L1-L9). Four parameters with three levels ($L_9(3^4)$) have been chosen; Molarity (0.5 M, 2 M and 5 M), volumetric solid:liquid ratio (1:50, 1:100 and 1:200), temperature (RT, 60˚C and 90˚C) and rotating speed (30, 100 and 200 rpm). The parameters and their levels are presented in Table 4.2. In addition, a control experiment (L10) at the optimum parameters has been done to maximize the efficiency within the defined experimental frame.

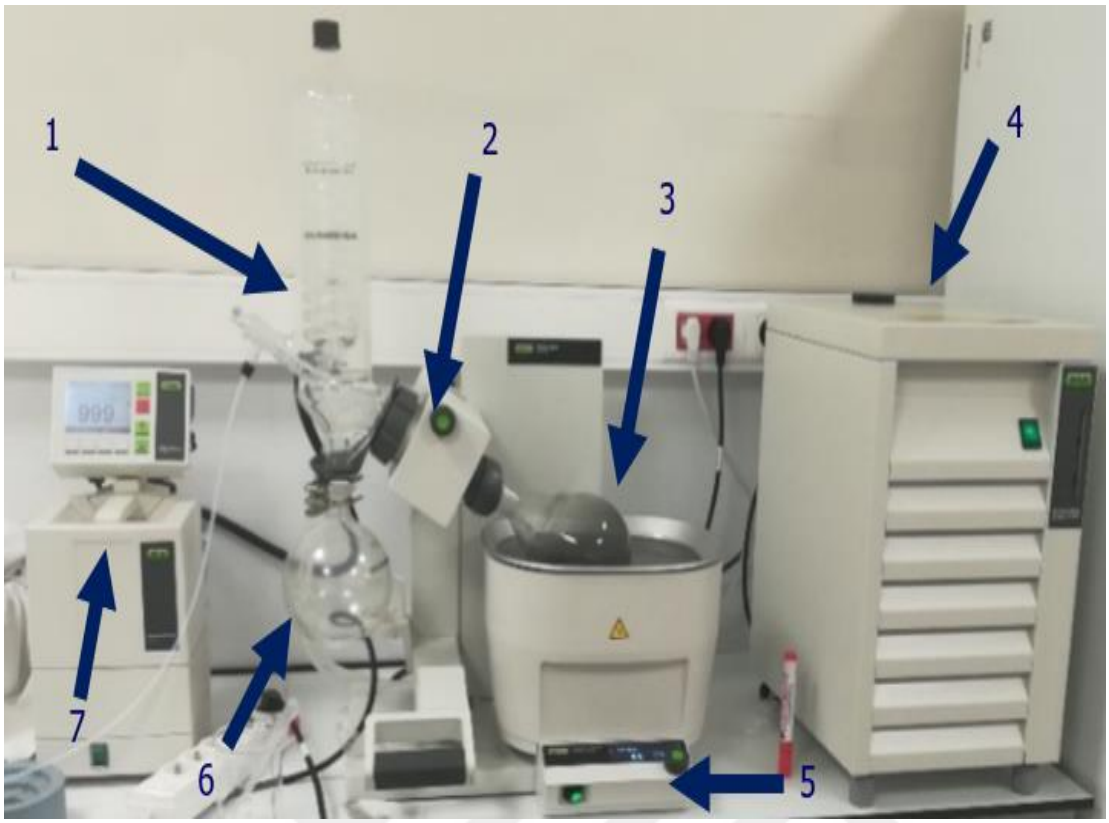

Figure 4.3: Rotary evaporator system 1. Glass condenser 2. Rotating motor 3. Leaching flask 4. Cooling chiller 5. Control unit 6. Collecting bottle 7. Vacuum pump

For further optimization, time depended experiment (L11) is performed at the optimum process parameters (L10) resulted from the Taguchi experimental design, for 6 hours. Moreover, the precursor's particle size effect on leaching efficiency (L12) has been investigated by using ferrchromium particles (Dv50) of 107.5 μm.

In the second step of leaching study, additional experiments have been performed to analyze the kinetic of the Fe leaching from FeCr alloy.

Table 4.2 gives the experimental parameters of the samples fabricated in leaching step of the thesis.

Table 4.2: Constructed experiments for leaching of ferrochromium.

Experiment code	Molarity (M)	Solid:Liquid Ratio (Vol:Vol)	Temperature (˚C)	Rotating speed (RPM)	Duration (min)
L1	0.5	1:50	RT	30	150
L2	0.5	1:100	60	100	150
L3	0.5	1:200	90	200	150
L4	2	1:50	60	200	150
L5	2	1:100	90	30	150
L6	2	1:200	RT	100	150
L7	5	1:50	90	100	150
L8	5	1:100	RT	200	150
L9	5	1:200	60	30	150
L10	5	1:50	90	30	150
L11	5	1:50	90	30	360
L12	5	1:50	90	30	150
L13	5	1:50	45	30	150
L14	5	1:50	60	30	150

4.4 Selective Iron Precipitation

Oxalic acid has been added into leaching solution at room temperature. Then, pH is adjusted to 3 by titrating NH_4OH (25%). After balancing pH at 3, solution is stirred for 30 min. Yellow precipitate (Iron oxalate hydrate) is obtained after 30 min. of stirring. The yellow precipitate is filtered and cleansed for several time by deionized water, respectively. To analyze the precipitation efficiency the precipitating agent/leachate ratio are investigated with P1 and P2 experiment. After that, temperature effect is examined with P2 and P3. Finally, P4 is made for investigating effect of stirring compared to P2.

Table 4.3 gives the experimental parameters of the iron oxalate powders formed in precipitation process.

Table 4.3: Iron precipitation experiments.

Sample name	Temperature (˚C)	Oxalic acid: leaching solution ratio (vol./vol.)	Rotating speed (RPM)
P1	25	1:100	450
P2	25	1:5	450
P3	60	1:5	450
P4	25	1:5	200

4.5 Heat Treatments

Table 4.3 gives the experimental parameters of the iron rich oxalate powders in heat treatment step of the thesis.

Experiment are constructed by considering the thermal analysis results and literature review's outcomes.

Table 4.3: Constructed calcination and heat treatments for iron oxalate hydrate powder.

Sample name	Temperature (˚C)	Atmosphere	Duration (min.)
FeOxH	70	Vacuum	720
FeOxA2	180	Vacuum	120
FeOxA3	180	Vacuum	180
FeOxA6	180	Vacuum	360
FeOxA205	205	Vacuum	180
FeO215	215	Air	180
FeO3003	300	Air	180
FeO3002	300	Air	120
FeO350Ar	350	Argon	120

4.6 Anode Fabrication

Slurries are made by mixing PVDF (as binder), conductive carbon black and iron based powder with 10% 10% and 80%wt. ratios. PVDF and active material are separately dissolved in NMP via Thinky ARE-250 (Figure 4.4.a). Then, all is mixed together with Thinky ARE-250.

Lamination is performed by Dr. Blade technique (Figure 4.4.b). Slurries are casted on 10 µm copper foil. The spread lamination is dried at 70˚C for 16 hours. Then, the dried foils are rolled to achieve anode with 30 µm thickness by using a roller (Figure 4.4.c).

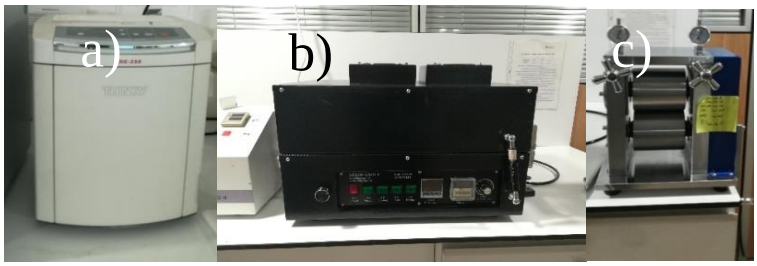

Figure 4.4: Used machines in lamination a) Thinky ARE-250 mixer b) Dr. Blade c) Roller.

4.7 Characterizations

4.7.1 Wet chemical analysis

For determining amount of iron content of leaching solutions, Atomic absorption spectroscopy is made by Shimadzu AA 160. Samples are diluted twice with deionized water.

4.7.2 Thermal analysis

DTA/TG analysis have been eventuated via Pelkin Elmer Diamond TG/ DTA. The test is made at air atmosphere and between room temperature to 950˚C with heating speed of 10˚C/min.

4.7.3 Compositional, morphological and structral analyises

Amount of carbon (and sulfur) in the starting precursor material (Ferrochromium) is detected by Eltra CS 600. X-ray fluorescence (XRF, Rigaku - ZSX Primus II) is applied to the ball-milled ferrochromium, the solid residue obtained after the leaching and the fabricated iron oxalate powders for determining their compositions. Particule size has been determined for milled ferrochromium via Malvern-Mastersizer 3001. Additionally, Energy-dispersive X-ray spectroscopy (EDS, Bruker) is used for chemical analysis. The structural analysis is done by X-ray diffractometer (XRD, Brucker AXS/Discovery D8) between 10-90˚ by Cu Kα with 0.02˚/sec scanning rate

Bonding type of synthesised powders have been investigated by Fourier Transform Infrared Spectrometer (FTIR) by Perkin Elmer Spectrum Two.

Morphological analysis for anode active materials have been performed by Scanning electron microscope (SEM, Zeiss Gemini 500).

4.7.4 Electrochemical tests

CR2032 standard coin cells are assembled to determine the electrochemical performance of the fabricated anodes (Figure 4.5). Batteries are assembled in MBRAUN, Labmaster (<1 ppm O_2, <1 ppm H_2O) glovebox. The separator is Celgrad 2400.The electrolyte contains 1M $LiPF_6$ (in EC:DMC (1:1) solution). Used anodes has 0.75-1.5 mg/cm^2 active material per unit current collector area (FeOxA2, FeOxA3, FeOxA6, FeO205, FeO215, FeO3002, FeO3003 and FeO350Ar) for galvanostatic tests. Cycling voltammetry tests are made with anodes having active material

(FeOxA2, FeOxA3, FeOxA6, FeO205, FeO215, FeO3002, FeO3003 and FeO350Ar) between 0.54-1.08 mg/cm^2.

Figure 4.5: CR2032 standard battery component (right to left), upper case, stainless steel spacer, fabricated anode, separator, lithium metal as cathode, stainless steel spacer, spring and case.

Galvanostatic tests are made with MTI BST8-WA under a current load of 50 mA/g between 1mV-3 V (vs Li/Li$^+$).

Cycling voltammetry has been performed to investigate the lithiation mechanism of the electrodes. Gamry Interface1000E is used in the experiments. First 4 cycles CV curvatures are recovered when the electrode is cycled between 1mV-3V (vs Li/Li$^+$) with a scan rate of 0.2 mV/sec.

5. RESULTS AND DISCUSSION

5.1 Milling

5.1.1 Taguchi results

By the help of the Eq. 5.1, we can calculate S/N ratios for investigating the effect of parameters on particle size. For that purpose, "small is better" approach is chosen because literature claims that leaching efficiency will be higher at smaller particle size of the precursor material [75, 77]. Y represents particle size in unit of μm and n is the number of observations.

$$\frac{S}{N} = -10xlog(\frac{\sum Y^2}{n}) \quad (5.1)$$

The milling experiment parameters, results and calculated S/N ratios for each experiment could be seen in Table 5.1.

Table 5.1: Taguchi experiment and results.

Experiment no	Duration (hours)	Rotation speed (RPM)	BPR	Particle Size (Dv50) (μm)	S/N
1	1	235	4:1	41.1	-32.2768
2	1	500	10:1	43.3	-32.7298
3	4	235	10:1	2.78	-8.8809
4	4	500	4:1	30.8	-29.771

After calculating S/N ratio of each experiment, Eq. 5.2. is applied.

$$b_1 = \frac{Experiment\ no.1 + Experiment\ no.4}{2} \quad (5.2)$$

Graphs with S/N ratios are given in Figure 5.1. S/N graphs show the optimum parameters for ferrochromium milling are 4 hours (a_1), 235 rpm (b_1) and 10:1 BPR (c_2).

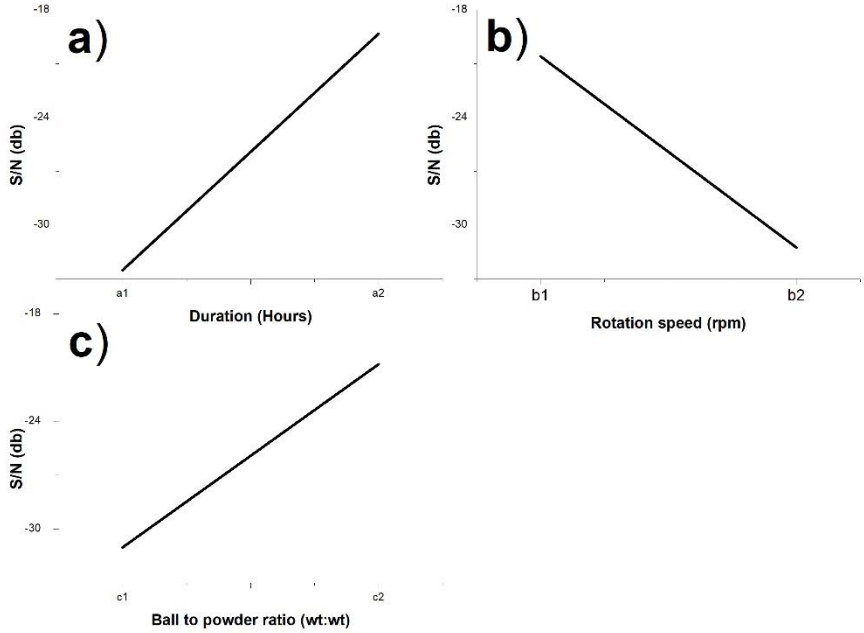

Figure 5.1: a) S/N -duration b) S/N -rotation speed c.) S/N -ball to powder ratio.

5.1.2 Anova analysis

In Table 5.2, ANOVA analysis calculation could be seen.

Table 5.2: ANOVA analysis for ferrochromium milling

	Degree of freedom	**Sum of square**	**Average of square**	**F value**
Duration	1	173.64		
Rotating speed	1	113.88		
BPR	1	104.42		
Error				
Sum	3	391.94		

As seen Table 5.2, BPR has the lowest F value. So by taking BPR parameter into error function, Anova analysis is repeated. The results show that the time and speed are the most effective parameters (Table 5.3). This result is compatible with the literature [99].

Table 5.3: Pooled ANOVA analysis for ferrochromium milling.

	Degree of freedom	Sum of square	Average of square	F value
Duration	1	173.64	173.64	1.59
Rotating speed	1	113.88	113.88	1.09
Error	1	104.42		
Sum	3	391.94		

5.1.3 Morphological, structural and chemical characterization

A control experiment has been run at the optimum parameters. The expected particle size could be calculated by using Eq. 5.3. X, T, a_2, b_1 and c_2 represent control experiment S/N ratio, average S/N value of all experiment and control experiment parameters as stated above, respectively.

$$X = T + (a_2 - T) + (b_1 - T) + (c_2 - T) \quad (5.3)$$

Results prove that control experiment give 2.78 (Dv50) micron particle size which is in agreement with experimental results. A remarkable and a small humps aredetected around 10 µm and 20 µm.

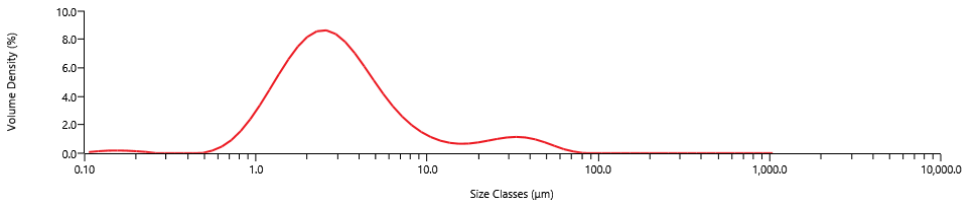

Figure 5.2: Particle size distribution of the control experiment.

Figure 5.3 demonstrates SEM images of the milled powder (at the control experiments' parameters). Images confirm the particle size distribution analysis (the dimensions are generally around 2.78 µm). It is clearly understood by the SEM examination that the obtained particles have irregular morphology (Figure 5.3.a-b).

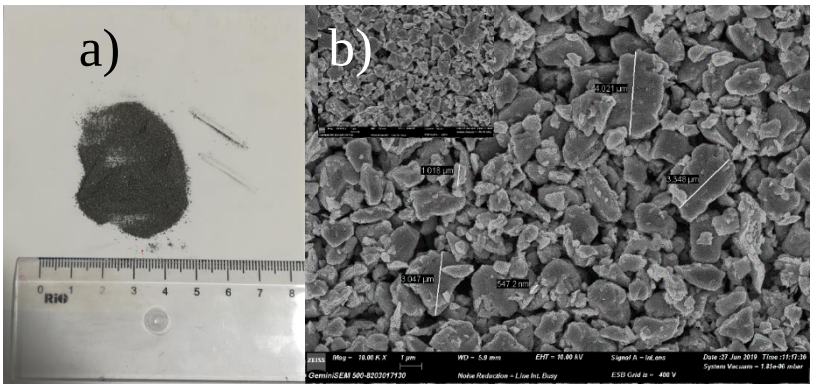

Figure 5.3: Images of milled ferrochromium a.) Taken empirically b.) SEM images x10000 magnification (left hand side x5000 magnification).

XRF analysis result of the milled powder (at the control experiments' parameters) is presented in Table 5.4. The composition shows similarities with the literature [100-101].

Carbon and sulphur content analysis justifies that the milled ferrochromium has wt. ~%5 carbon and 452 ppm sulphur as declared by Eti Krom A.Ş. [101].

Table 5.4: XRF analysis of milled ferrochromium.

Elements	XRF Analysis (el.%)
Si	0.66
Cr	68.34
Fe	29.49
Co	0.008
Ni	0.54
Other metals	balance

XRD analysis results of the pristine (as-received) and the ball-milled ferrochromium alloy are given in Figure 5.4. The XRD spectra show peaks of carbide structures such as Fe-Cr-C (00-005-0720) and chromium carbide (01-089-7244) along with ferrochromium, and iron silicon oxide (00-052-1141) intermetallics and magnetite (00-026-1136). Such spectrum is in agreement with the literature [102-105].

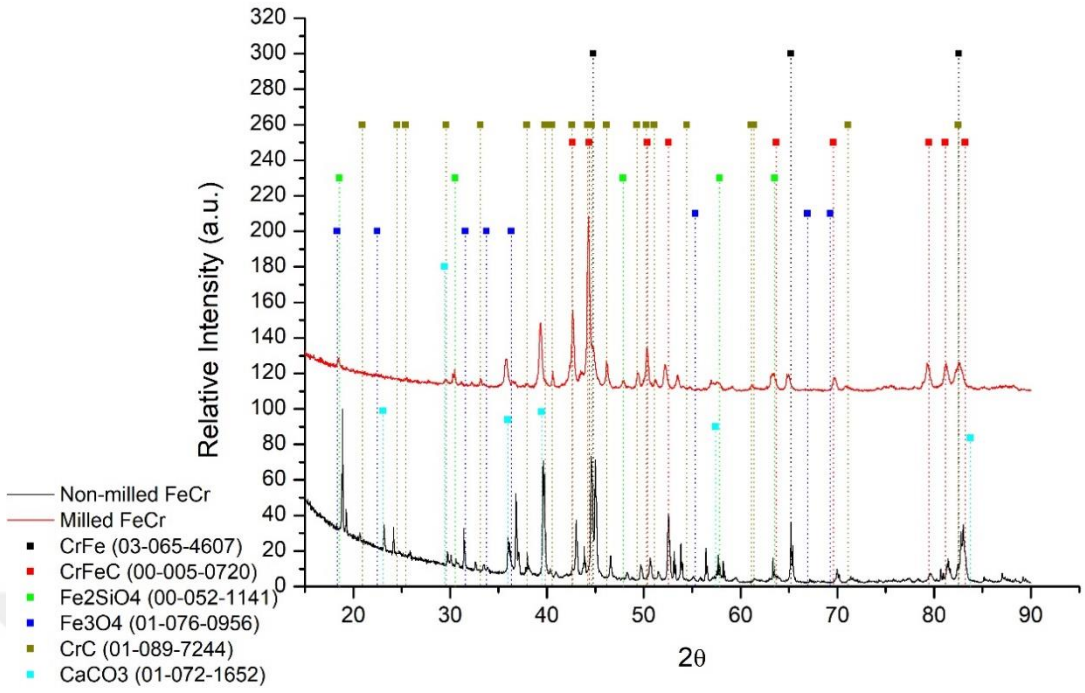

Figure 5.4: XRD patterns of non-milled (black line) and milled ferrochromium (red line).

5.2 Leaching

5.2.1 Taguchi analysis and optimization of leaching operation

Leaching operations have been realized in a rotary evaporator. For achieving the maximum iron leaching efficiency, "larger is better" principle (Eq. 5.4) is used to calculate S/N values. "y_i" represents AAS results and "n" is the number of repeated experiments.

$$S/N = -10 * \log(\frac{1}{n} * \sum_{i=0}^{n}(\frac{1}{y_i{}^2})) \quad (5.4)$$

Calculated S/N ratios and experiment results with parameters can be seen in Table 5.5.

S/N curves (Figure 5.5) have been constructed by the help of Equation 5.2. As seen in Figure 5.5, optimum parameters are demonstrated as 5 M, 1:50 solid: liquid ratio, 90˚C and 30 rpm.

Table 5.5: Design of experiments and results of L_9 (3^4) orthogonal array for iron.

Experiment No	Molar of acid (M)	Solid:liquid Ratio (vol:vol)	Temperature (˚C)	Rotation rate of the flask (rpm)	AAS Fe (g/l)	S/N for Fe (db)
1	0.5	1:50	25	30	10.81	20.67
2	0.5	1:100	60	100	9.59	19.64
3	0.5	1:200	90	200	9.1	19.19
4	2	1:50	60	200	12.38	21.86
5	2	1:100	90	30	10.82	20.68
6	2	1:200	25	100	7.04	16.95
7	5	1:50	90	100	13.1	22.35
8	5	1:100	25	200	9.35	19.42
9	5	1:200	60	30	10.03	20.03

An additional control experiment is performed under these conditions and AAS analysis shows that the solution has 13.22±.1.3 g/l Fe ions. Knowing that the theoretically calculated value is 14.39 g/l (by using Eq. 5.3), 91.88% correlation between experimental and theoretical value is found, eventually.

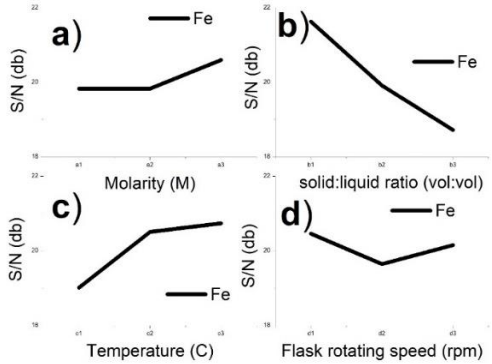

Figure 5.5: S/N values of a.) Molarity (M) b.) S/L ratio c.) Temperature (˚C) d.) Rotation rate of flask (rpm).

5.2.2 Anova analysis

ANOVA analysis has been performed to determine the most effective parameter affecting the leaching efficiency of Fe (Table 5.6 and Table 5.7).

Table 5.6: Calculation of ANOVA for iron leaching.

Parameter	Degree of freedom	Sum of Square	Mean of Square	F value
Molarity	2	1.17		
Solid:Liquid	2	12.78		
Temperature	2	5.26		
Rotation rate of the flask	2	1.02		
Error				
Total	8	20.22		

The calculations show that the rotation rate of flask and molarity are the less effective parameters. Therefore these two parameters are considered as errors and revised ANOVA calculation could be seen in Table 5.7.

Table 5.7: Revised Calculation of ANOVA for iron leaching.

Parameter	Degree of freedom	Sum of Square	Mean of Square	F value
Solid:Liquid	2	12.78	6.39	11.73
Temperature	2	5.26	2.62	4.82
Error	4	2.18	0.54	
Total	8	20.22		

According to these calculations, the most effective parameter on the leaching efficiency has been found as the solid / liquid ratio. It is also revealed that temperature is also an effective parameter.

5.2.3 Effect of precursor's powder size on the leaching efficiency

To justify the advantages of ball milling an additional experiment where 107.5 µm (Dv50) sized FeCr alloy has been used as the starting material for leaching experiment. AAS analysis shows that when precursor material with larger particle size is used in leaching, the iron recovery efficiency is decreased down to 6.61%.

5.2.4 Effect of process duration on the leaching efficiency

Once the ideal leaching parameters are defined by the Taguchi method, the control experiment (5 M, 1:50 solid:liquid ratio, 30 rpm and 90˚C) is repeated for 6 hours to examine the effect of process duration on the leaching efficiency. 11 samples are collected at different times during the control experiment (0, 1, 5, 15, 60, 90, 120, 180, 240, 300 and 360 minutes). 5 ml of samples have been taken from the leach solution and the solution compositions are subjected to AAS analysis. To avoid a sudden change in the solid / liquid ratio, after each sample is taken, the sulphuric acid solution at the same molarity and temperature is added to the rotary evaporator. The amount of iron transferred to the solution is calculated using the equation proposed by Liu et al. (In Equation 5.5) [80].

$$recovery(\%) = \frac{(iron\ in\ solution\ from\ AAS\ (g/L)) * (leachate\ volume(L))}{(metal\ amount\ in\ Fe{-}Cr(\%) from\ XRF) * (initial\ Fe{-}Cr\ amount(g)} * 100 \quad (5.5)$$

Iron leach efficiency based on time is shown in Figure 5.6.

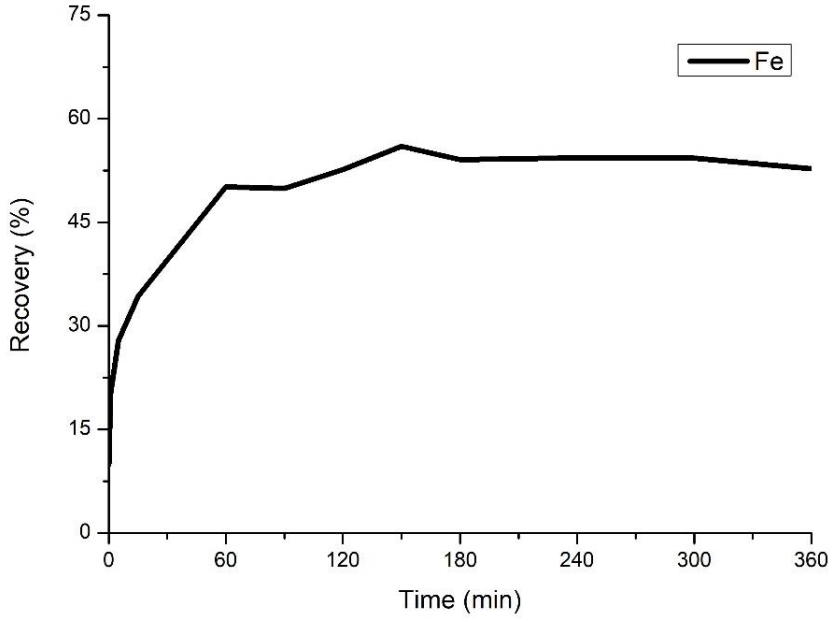

Figure 5.6: Time-recovery graph for iron leaching with sulphuric acid.

This trend (Figure 5.6) has resemblance with Ruiz et al work. They have categorized this type of leaching time-recovery graph in three parts: induction, conversion and stabilization. In this sense, they [106] are explained that the induction is the shortest period lasting around 20 min and afterwards the conversion has taken place where metal complexing happened in the solution, and lastly at the stabilization, leaching operation ended with its highest recovery efficiency [106].

The results exhibit that at 150 min. the maximum amount of iron ions pass into the solution. When the amounts of iron in the precursor and in the leachate are compared, 56% efficiency is found. The existences of FeCr, Fe_3O_4, FeCrC and Fe_2SiO_4 in the residue may explain this result (Figure 5.7., Equations 5.6. and 5.7.) [103-104, 107-108]. Moreover, unlike to the precursor's XRD data, chromium sulfate is also observed (Equation 3.10).

The XRF result of residue could be seen in Table 5.8.

Table 5.8: XRF result of the residue obtained after leaching (under the control experiment conditions).

	Fe	Co	Ni	Si	Cr	Other
Residue	14.479	0	0.417	8.77	52.235	balance

Comparison between the precursor and the residue shows the amount transition metals are decreased dramatically. Dissolution reactions (3.10-3.15) have been occurred as stated in Lui et al. [80] work. Sulphur content has been increased from 452 ppm to 14.095%el. because of the sulphates formation.

$$2\,FeO\ *\ Si\,O_2\ +\ 2\,H_2SO_4\ \rightarrow\ 2FeSO_4\ +\ H_4SiO_4 \tag{5.6}$$

$$CaCO_3 + H_2SO_4 \rightarrow CaSO_4 + CO_2 + H_2O \tag{5.7}$$

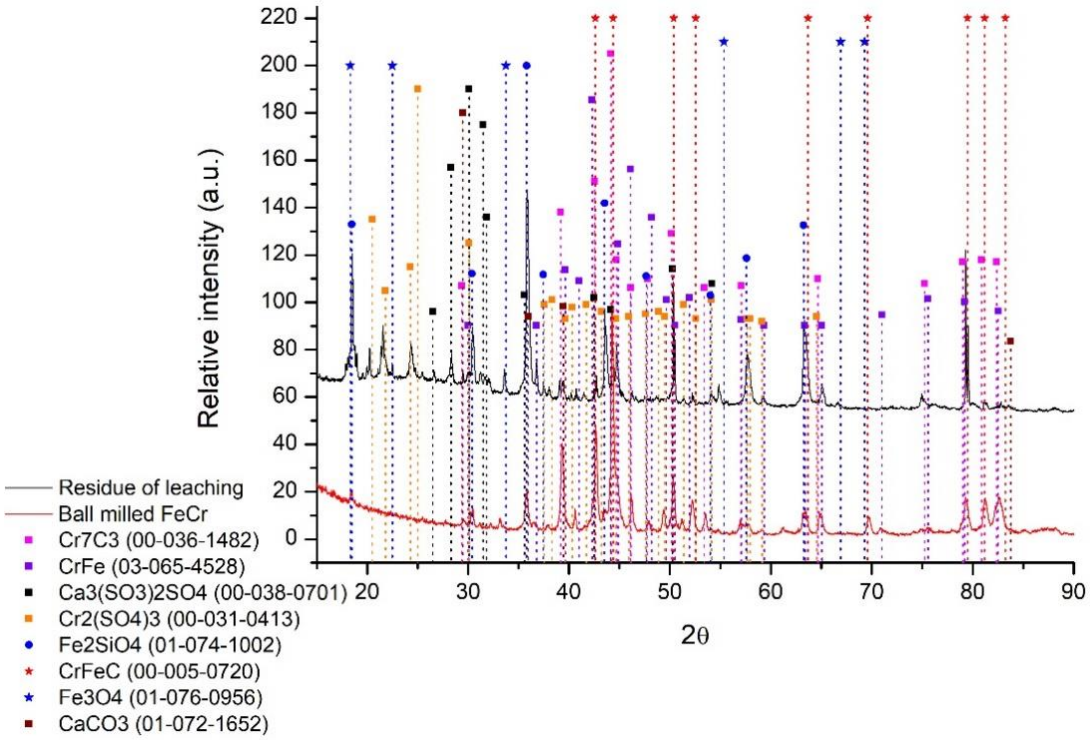

Figure 5.7: XRD pattern of leaching residue (black line) and ball milled FeCr (red line).

5.2.5 Effect of the rotation speed on the leaching efficiency

The experiment at the optimum leaching conditions has been repeated with different rotation speeds (0, 30 and 60 rpm). The stagnant solution results in the worst efficiency, as stated Lui et al [80]. Figure 5.8 demonstrates that the leaching efficiency at different rotation speed is always lower than 40%, which means that the leaching reaction is chemically controlled.

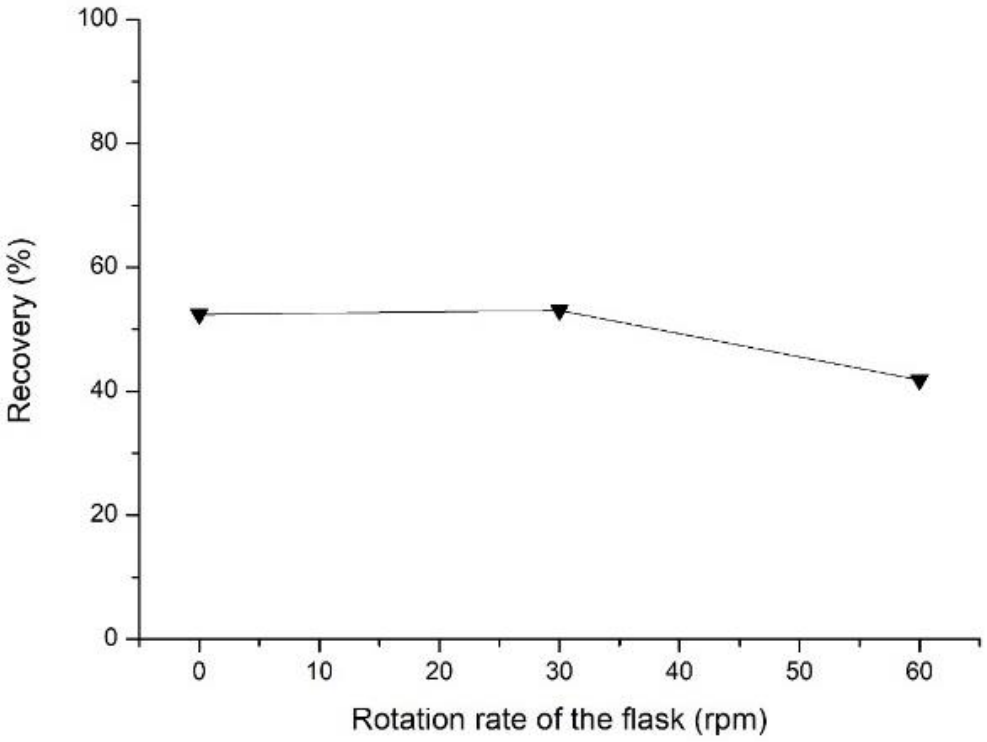

Figure 5.8: Rotation rate of flask (rpm)- recovery(%) graph.

5.2.6 Kinetic analysis of ferrochromium leaching operation with sulphuric acid

Leaching is a heterogeneous reaction due to solid-liquid interactions. Various kinetic models related to the heterogeneous reactions have been studied. Table 5.9 shows the kinetic modals and the calculated R^2 and $R^2_{adjusted}$ values for each temperature.

Calculations show the best fitted model is the mixed modal (surface reaction control; lixiviant diffusion model) as it results in the highest R^2 and $R^2_{adjusted}$ average values compared to other modals. To evaluate the leaching mechanism in detail, the kinetic model can be fitted by changing the n value in the kinetic formula. If n is close to 1, the reaction is described as an 'ideal chemical reaction control phenomena', but if n is equal to or less than 0.5 the reaction is assumed to be 'diffusion controlled'.

Calculations (Table 5.10) give the highest average R^2 and $R^2_{adjusted}$ value (for 45˚C, 60˚C and 90˚C) when n = 0.4 for iron (R^2: 0.886).

Table 5.9: Kinetic models and the calculated R^2(and $R^2_{adjusted}$) values for Fe leaching.

Expression	Controlling mechanism	Fe 45˚C	Fe 60˚C	Fe 90˚C	Average R^2 (and $R^2_{adjusted}$)	Ref.
$1-\frac{2}{3}*x-(1-x)^{\frac{2}{3}}=k*t^n$	Solid product layer diffusion	0.617 (0.5532)	0.8582 (0.8346)	0.6426 (0.583)	0.705933333 (0.6569)	[109]
$\ln(a/a\text{-}x)=k*t^n$	Chemical reaction control model	0.6766 (0.6227)	0.942 (0.9323)	0.8045 (0.772)	0.8077 (0.7757)	[110]
$-\ln(1\text{-}x)=k*t^n$	Mixed model (surface reaction control; lixiviant diffusion model)	0.6784 (0.6248)	0.9392 (0.9290)	0.8357 (0.8083)	0.817766667 (0.7873)	[111]
$1-(1-x)^{\frac{1}{3}}=k*t^n$	Chemical reaction control	0.6755 (0.6237)	0.9409 (0.9310)	0.8213 (0.7915)	0.813 (0.7953)	[112]
$1-(1-0.45*x)^{\frac{1}{3}}=k*t^n$	Surface reaction control by shrinking core model	0.6764 (0.6225)	0.9421 (0.9324)	0.802 (0.769)	0.806833333 (0.7746)	[113]
$1-(1-x)^{\frac{2}{3}}=k*t^n$	Shrinking core model (Film diffusion control-dense-shrinking model)	0.6726 (0.618)	0.9387 (0.9285)	0.7398 (0.6964)	0.7837 (0.7655)	[112]

Activation energy of control experiment could be calculated by Arrhenius equation (Equation 5.9.a-b). E_A, R and T represent activation energy (kj/mol), gas constant (8.314 j/mol.K) and temperature in unit of K.

$$lnK = lnA - \frac{E_A}{R*T} \tag{5.9}$$

Activation energy is calculated as 46.12 kJ/mol according to Equation 5.9 (Figure 9). The calculated value has similarities with the literature [80, 83, 114].

Table 5.10: Calculated R^2 (and $R^2_{adjusted}$) values for different *n (n=1-0.3)* in kinetic expression of this study.

n values	Fe 45˚C	Fe 60˚C	Fe 90˚C	Average of R^2 (and $R^2_{average}$) values
1	0.6784 (0.6248)	0.9392 (0.9290)	0.8357 (0.8083)	0.8178 (0.7874)
0.9	0.6921 (0.6491)	0.9356 (0.9249)	0.8594 (0.8360)	0.8290 (0.8033)
0.8	0.7078 (0.6591)	0.9306 (0.9191)	0.8841 (0.8648)	0.8408 (0.8143)
0.7	0.7259 (0.6803)	0.9238 (0.9111)	0.9095 (0.8944)	0.8531 (0.8286)
0.6	0.7470 (0.7048)	0.9143 (0.9001)	0.9353 (0.9246)	0.8655 (0.8432)
0.5	0.7710 (0.7329)	0.9008 (0.8842)	0.9605 (0.9539)	0.8774 (0.8570)
0.4	0.7967 (0.7629)	0.8795 (0.8594)	0.9818 (0.9788)	0.8860 (0.8670)
0.3	0.8178 (0.7974)	0.8409 (0.8144)	0.9893 (0.9875)	0.8827 (0.8654)

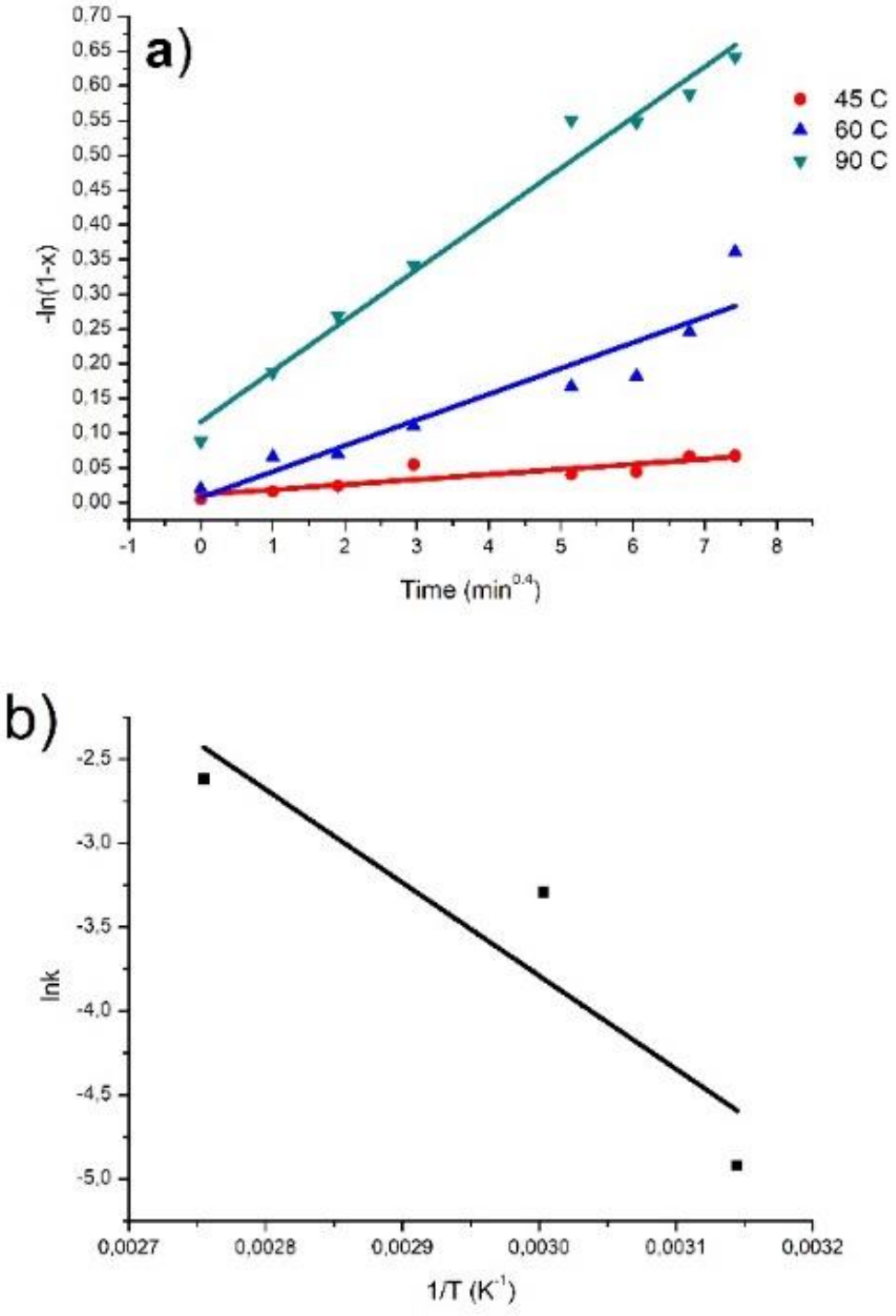

Figure 5.9: a) Kinetic curve of ferrochromium-sulphuric acid leaching b) Temperature dependent kinetic curve

This outcome also agress with the outcome stated in the section 5.2.5 about stirring rate of flask.

5.3 Selective Iron Precipitation

After achieving the highest iron ion concentration in the leachate, oxalate precipitation has been performed according to Lui et al's work to selectively recover Fe (as well as Ni,Mn,Co) ions from the solution [85]. P1, P2, P3 and P4 have been made for observing parameters' effect on the iron precipitation efficiency. Yield of iron oxalate precipitation is calculated following the Equation 5.10 by using initial and final solutions' concentrations obtained by AAS analysis.

$$\%precipitation\ yield = \frac{initial\ iron\ content\ from\ AAS\ result\ \left(\frac{g}{l}\right) - final\ iron\ content\ from\ AAS\ result\ \left(\frac{g}{l}\right)}{initial\ iron\ content\ from\ AAS\ result\ \left(\frac{g}{l}\right)} x100 \qquad (5.10)$$

Results are given in Table 5.11. Precipitation yield is calculated as 86% in P2. Solubility of oxalic acid has important role on precipitation as Ang et al stated [61]. Herein, the effect of oxalic acid/leaching solution ratio has been investigated (P1 (1/100) vs P2 (1/5)). Eye-ball observation reveals that no precipitate is noted in P1; unlike to P2. These could be related to occurance of soluble amount of iron oxalate hydrate in the solution [116].Then, stirring effect has been examined (P3 (200 rpm), P2 (450 rpm)). Results show that at low stirring rate, the precipitation efficiency is decreased from 86% to 58.71%. Lower precipitation efficiency could be explained related to the dielectric constant of the oxalic acid which prevents its practical dissolution [61]. Lastly, temperature effect on precipitation's efficiency is investigated (P4 (60˚C) and P2 (25˚C)). Results show that at high temperature the solubility of iron oxalate is increased, hence no precipitation is observed [116].

After drying at 70˚C (in vacuum) for 12 h, the obtained precipitate (P2) has been analyzed by XRF. XRF result reveals that the powder (P2) contains el. %94.49 Fe, el. %2.62 Ni, el. %1.98 Cr, el. %0.37 S, el. %0.35 Mn, el. %0.13 Co and el. %0.07 Si. This result verifies that not only Fe but trace amounts of other transition metals (other than chromium) are recovered selectively by adjusting the pH (around 3) of the solution.

Then to further examine the structure of the powder (P2), XRD analysis has been done. As seen in Figure 5.10, all peaks are indexed as iron oxalate hydrate (00-022-0635) with orthorhombic structure.

Table 5.11: Precipitation parameters and resutls.

Sample name	Temperature (˚C)	Oxalic acid: leaching solution ratio (vol./vol.)	Rotating speed (RPM)	Iron extraction (%)
P1	25	1:100	450	0
P2	25	1:5	450	86
P3	60	1:5	450	0
P4	25	1:5	200	58.71

FTIR spectroscopy resolves the individual spectroscopic features of all samples (Figure 5.11). It reveals that P2 (FeOxH) has a characteristic spectrum of iron oxalate hydrate as agreed with the literature [117]. As statement of D'Antonio et al., oxalates behave like tetradentate ligand [117]. Therefore, patterns (or peaks) are occurred at high frequency region)[117]. Peak around 3350 cm^{-1} indicate strong O-H bonds and strong C-O bonds are identified at around 1625, 1361 and 1325 cm^{-1} [117]. Tiny bump around 750 cm^{-1} refers weak H_2O. As statement of Angermann and Töpfer [117], peak around 490 cm^{-1} refers to strong Fe-O bond.

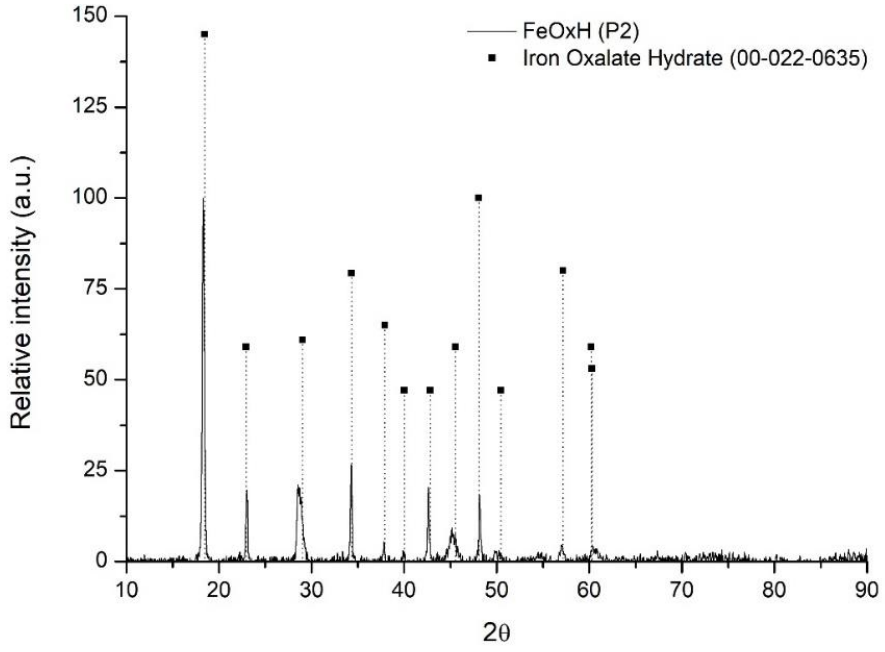

Figure 5.10: XRD analysis of precipitated iron-rich oxalate hydrate from control experiment leaching solution (P2).

No peaks related to other transition metals (or their oxides) have been noted on XRD and FTIR analyses' results. Similar observations have been reported previously in the literature [53-55]. El-Battal et al. [118] and Mai et al [53] have stated that FTIR data donot reveal any characteristic shift in the peak position related to dopping effect.

On the other hand, the effect of doping can be seen as the structural modification of the host structure's unit cell. XRD analysis justifies that the peak at $2\theta = 18.32^{\circ}$ ($2\theta = 18.46^{\circ}$ for JCPDS No: 00-022-0635) that corresponds to (202) plane is the most dominant peak and a slight peak shifting is noted on the XRD result (Figure 5.9) of P2, which could be related to the dopping effect.

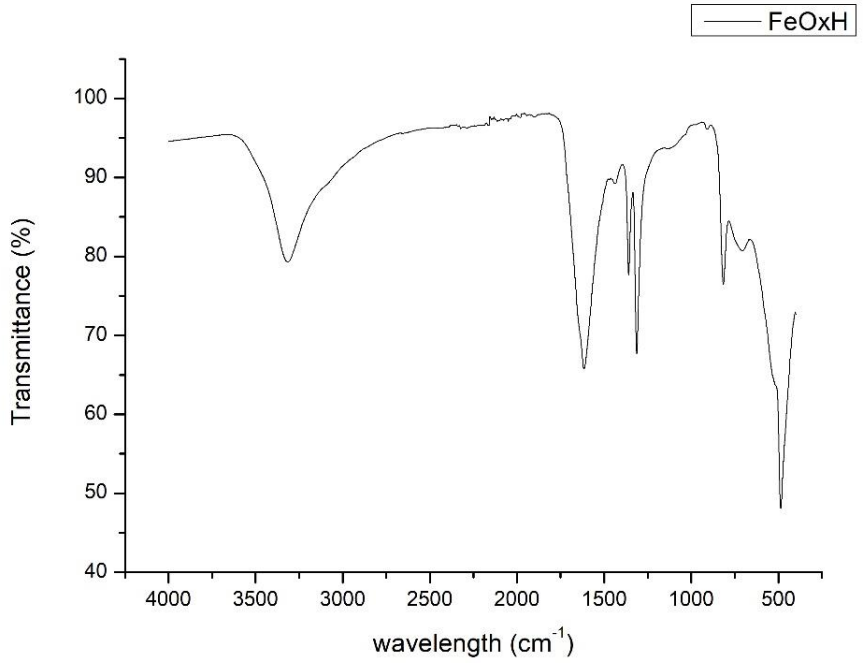

Figure 5.11: FTIR result of FeOxH powder.

The morphology of the iron-rich oxalate hydrate powders (P2) has been investigated by SEM. Figure 5.12 shows that oxalate particles have angular columnar morphology as agreed with literature [64]. The average length of precipitated oxalate powder (P2) is 2.88±1.81 μm and average width is 1.02±0.34 μm

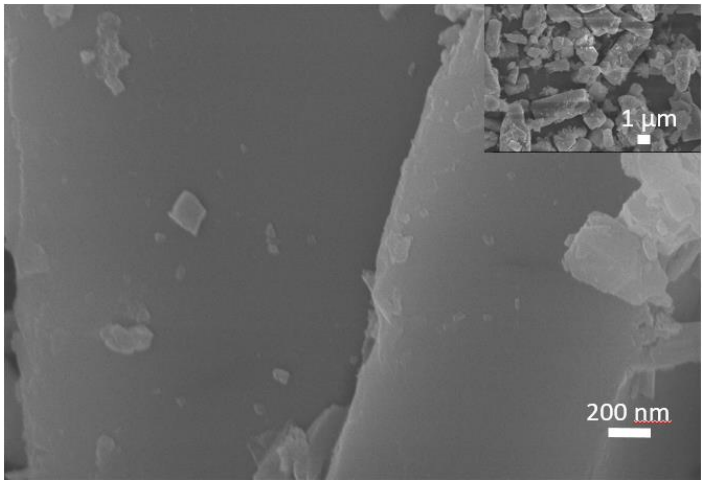

Figure 5.12: SEM images of precipitated iron oxalate hydrate x70000 magnification (right hand side x10000 magnification).

5.4 Heat Treatments for Iron Oxalate Hydrate

5.4.1 Thermal analysis results

TGA-DTA analyses (Figure 5.13.a-b) have been performed to determine the iron-rich oxalate powder (P2)'s thermal stability in air atmosphere. Table 4.3 defines the sample codes and their heat treatment parameters. TGA results are in line with the work of Rao [119] et al. Figure 5.13.a shows that the oxalate hydrate (P2) has multi-step calcination profile similar to the characteristics of the iron oxalate hydrate [119]. A small amount of mass loss has started around 100˚C. For this reason, as stated in the literature [61], oxalate powders are first dried under vacuum for 12 hours at 70˚C, in order to evaporate the moisture without a phase transformation. The obtained FeOxH powder (Figure 5.14.a) was obtained in yellow (HEX: # E3D48D) as indicated in the literature [119]. Further investigation via DTA show that (Figure 5.13.b), there are an endothermic dehydration peak at 180˚C and an exothermic peak for oxidative decomposition at 220˚C [119]. As a consequence, TGA reveals two different slopes in the range of 170-215˚C and 215-270˚C, showing 55% of the initial mass lost in the heat treatment. Rao et al. have associated this mass change with the formation of Fe_2O_3 [119]. Therefore, after drying in vacuum, iron-rich oxalate powders (FeOxH) are calcinated under vacuum for 2 (FeOxA2), 3 (FeOxA3) and 6 (FeOxA6) hours at 180˚C, considering the TGA and the literature outcomes. The related reaction can be seen in Equation 5.11, which demonstrates that the crystal water is partially released in that condition depending on the process duration for FeOxA2, FeOxA3 and FeOxA6 [61]. The colour of the powders (FeOxA2, FeOxA3 and FeOxA6) after this heat

treatment are changed to brown types (HEX: # B4A088, #2B1002 and #844423, respectively) as agreed with the literature (Figure 5.14.b-d) [120]. Then, different heat treatment experiments are planned in the light of TGA to determine the effect of heat treatment duration (Iron oxalate hydrate heat treated at 300˚C for 2 hours (FeO3002) and 3 hours (FeO3003)), temperature (Iron-rich oxalate hydrate heat treated at 215°C (FeO215 for 3 hours in air environment to compare the result with that of FeO3003) and environment (Iron-rich oxalate hydrate heat treated at 350˚C for 2 hours at argon atmospehere (FeO350Ar)). The views of the powders (Fig. 5.14.e-i) after these heat treatments demonstrate that each oxide powder has different color, as stated in the literature [119-122]: FeO205 (Hex: #422520), FeO215 (Hex: #774435), FeO3002 (Hex: #270604), FeO3003 (Hex: #38060A) and FeO350Ar (Hex: #4C291E).

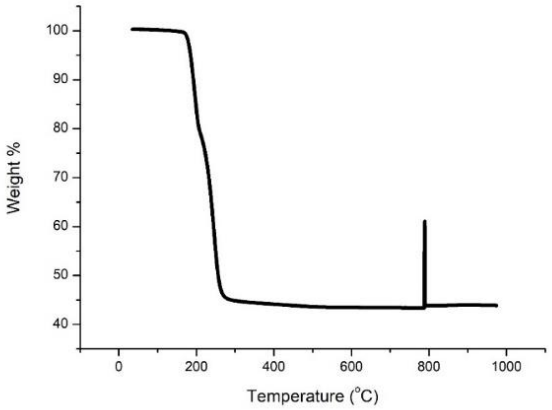

a)

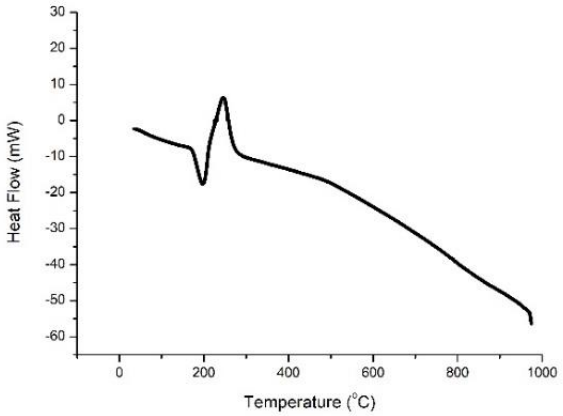

b)

Figure 5.13: Thermal analysis in air atmosphere a) TG result b) DTA result.

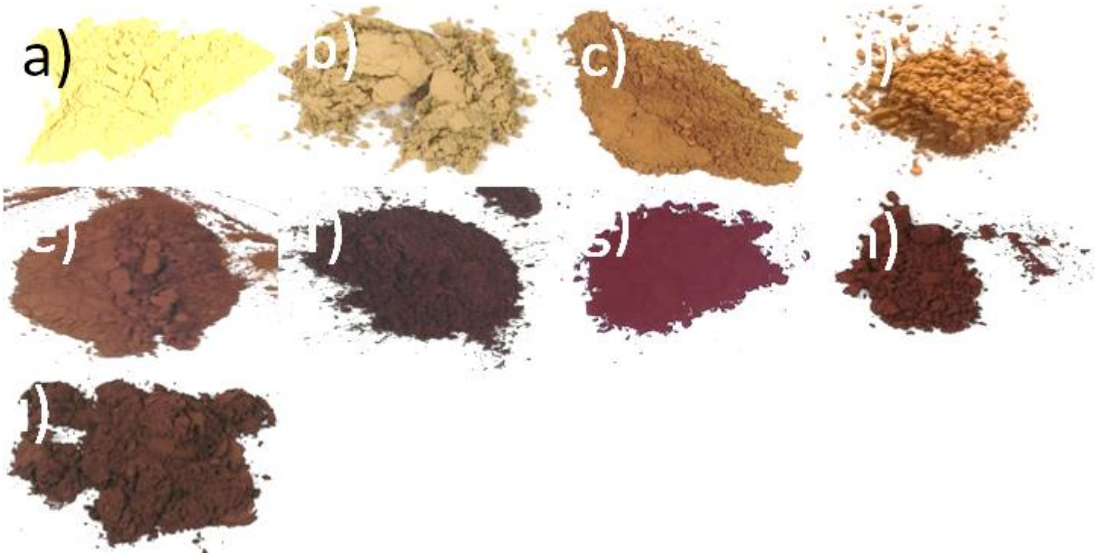

Figure 5.14: Empirically view of synthesized powders a) FeOxH b) FeOxA2 c) FeOxA3 d) FeOxA6 e) FeO205 f) FeO215 g) FeO3002 h) FeO3003 i) FeO350Ar.

5.4.2 Structural analysis

XRD analyses have been performed onto the heat-treated samples. The heat treatment process parameters of these samples are given in Table 4.3. As seen in Figure 5.15.a, iron oxalate anhydrate (Equation 5.11 [121]) has been achieved at 180˚C for 2 hours in vacuum atmosphere as Ang et al [61] have mentioned.

When XRD results of the FeOxA2, FeOxA3 and FeOxA6 are examined, it is seent that longer heat treatment duration (at 180˚C in vacuum environment) leads to the evaporation of the first crystal water (see Equation 5.11) then a distortion in the crystal structure and transformation of oxalate into magnetite occur eventually (Figure 5.15.a-c).

$$FeC_2O_4.2H_2O \rightarrow FeC_2O_4 + 2H_2O \quad (5.11)$$

Figure 5.15.e-f also exhibit the effect of heat treatment temperature on the atomic arrangement. By the effect of the elevetad temeperature, oxalate structure (FeOxA3) turns into oxide (Hematite, FeO205) in the vacuum atmosphere.

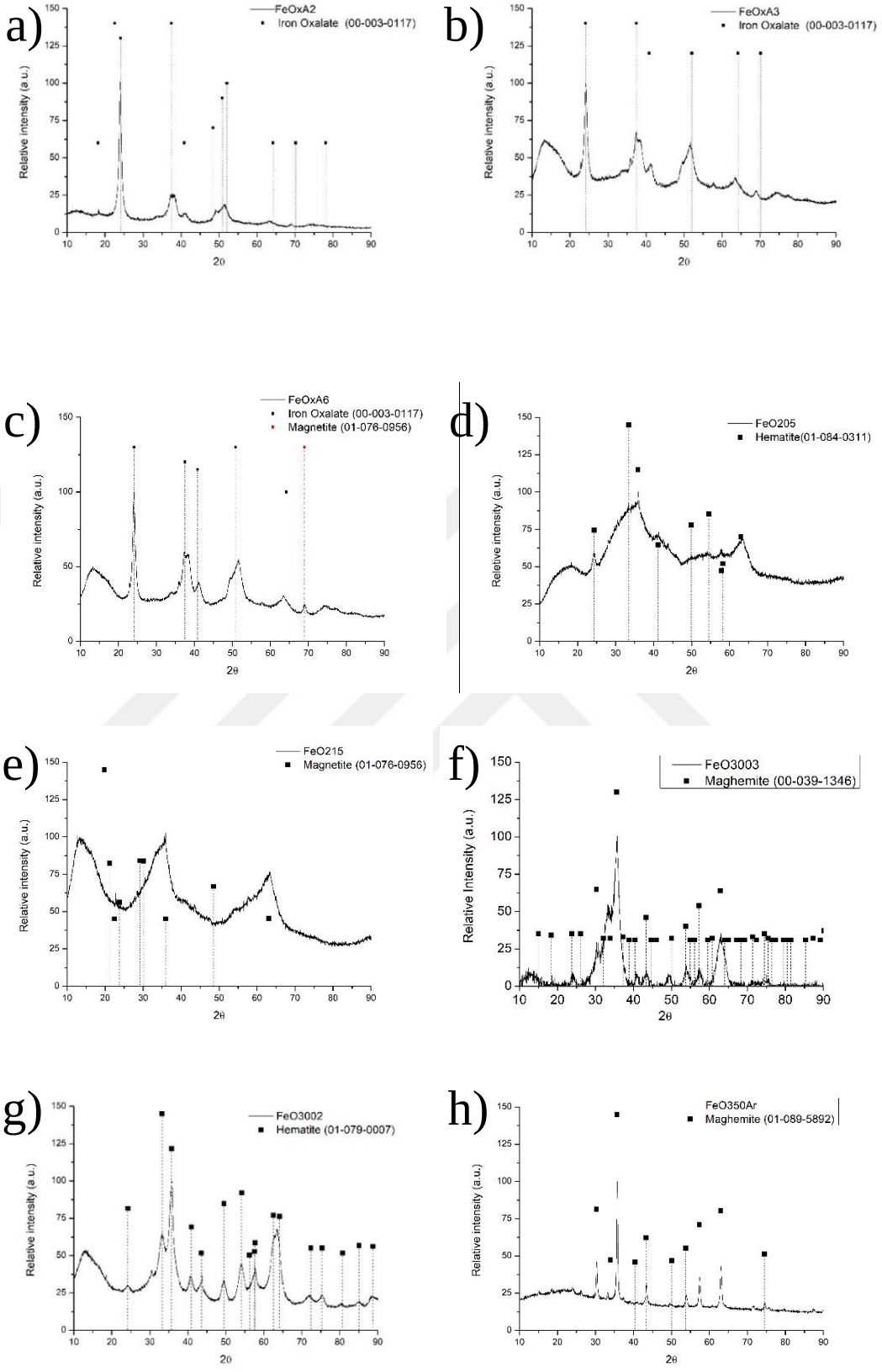

Figure 5.15: XRD patterns of achieved samples according to table 4.3 a) FeOxA2 b) FeOxA3 c) FeOxA6 d) FeO205 e) FeO215 f) FeO3003 g) FeO3002 h) FeO350Ar.

In case of air atmosphere, firstly, P2 sample is heat treated at 215˚C for 3 hours (FeO215) according to TGA result. Hermanek et al [121], have demonstrated that such heat treatment (around 230˚C) results in magnetite formation (Equation 5.12 [95]). Figure 5.15.e shows that similar to Hermanek's et al work, FeO215 contains magnetite particles.

$$12FeC_2O_4 \cdot 2H_2O + 8O_2 \rightarrow 4Fe_3O_4 + 24CO_2 + 24H_2O \qquad (5.12)$$

Then, to compare the effect of the temperature in air atmosphere, FeO3003 has been synthesised at 300˚C in 3 hours and maghematite phase is achieved according to XRD result. This occurrence resembles with Dhal et al [122] work's outcome.

For investigating the effect of heat treatment time onto the powders' crystal structures, P2 is heat treated in air atmosphere at 300˚C for 2 hours (FeO3002) and 3 hours (FeO3003). The results show that longer duration leads transformation of magnetite (FeO3002 (2 hours)) to hematite (FeO3003 (3 hours)). This output has resemblance with Zhou et al [95] work where they achieved hematite following the heat treatment of the iron oxalate hydrate in air atmosphere for 2 hours. Hematite (FeO3002) formation reaction could be defined by Equation 5.13 [123].

$$FeC_2O_4.2H_2O + 1/4O_2 \rightarrow 1/2Fe_2O_3 + CO + CO_2 + 2H_2O \qquad (5.13)$$

Finally, to investigate the effect of heat treatment atmosphere, P2 sample is heat treated in Ar atmosphere at 350˚C for 2 hours. Argon atmosphere calcination effect has been mentioned by Angerman and Töpfer [123]. They have claimed that maghematite could be achieved at 400˚C in an inert atmosphere when iron oxalate hydrate is used as the precursor material. Similar to Angerman and Töpfer studies, herein the powder (FeO350Ar) revealed maghematite structure when P2 is heat treated in Ar atm at 350˚C for 3 hours (Figure 5.15.h).

According to XRD result, iron-rich oxalate powders (FeOxA2, FeOxA3 and FeOxA6) are found to have orthohrombic structure (JCPDS no: 00-003-0117). Magnetite powder (FeO215) has orthorhombic structure, hematite powders (FeO205 and FeO3002) have rhombohedral structure and maghematite (FeO3002 and FeO350Ar) powders are determined to have cubic structure.

When FTIR result are examined for iron-rich oxalate anhydrate samples (FeOxA2, FeOxA3 and FeOxA6), related peak for strong O-H bonding (peak around 3350 cm^{-1})

from water as in Figure 5.16 is disappearing by increasing calcination duration (from FeOxH to FeOxA6). Strong C-O bonds are identified at around 1625, 1361 and 1325 cm^{-1} and the peak around 719 cm^{-1} refers vibrational C-C bonding [117]. As statement of Angermann and Töpfer [123], peak around 490 cm^{-1} refers to strong Fe-O bond of the oxalate structure.

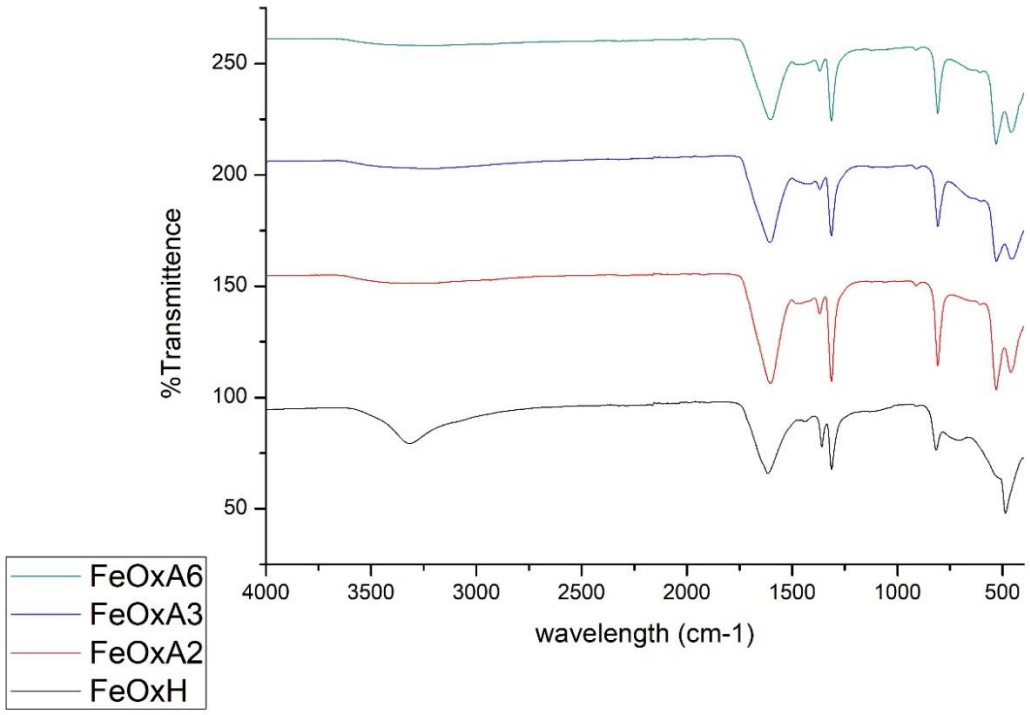

Figure 5.16: FTIR spectrums for FeOxH, FeOxA2, FeOxA3 and FeOxA6 (from down to up).

When iron oxide samples' FTIR results are examined in Figure 5.16, the peak at 570 cm^{-1} which is assigned to Fe-O bonding is noted for all samples other than FeO215 [124]. For FeO215, amorphization is noted due to absence of any peaks in the FTIR spectrum (Figure 5.14.e). In case of FeO205, there are peaks for strong C-O bonds at 1625, 1361 and 1325 cm^{-1} [117]. Moreover, there is a peak for vibrational C-C bonding at 719 cm^{-1} [117].

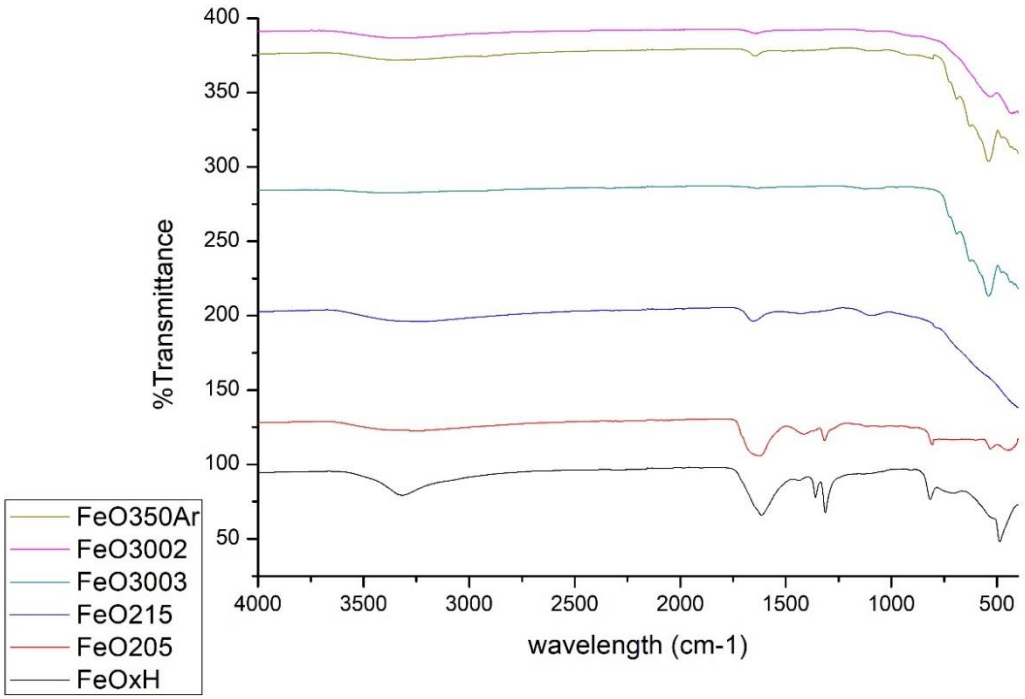

Figure 5.17: FTIR spectrum of FeOxH, FeO205, FeO215, FeO3003, FeO350Ar and FeO3002 (from down to up).

5.4.3 Morphological analysis

The morphology of the powders (FeOxA2, FeOxA3, FeOxA6, FeO205, FeO215, FeO3002, FeO3003 and FeO350Ar) are given in Figure 5.18.a-h. SEM images show that both the oxalates as well as the oxide powders have nearly same angular columnar morphology. However, there are some difference about morphology in case of sides and corners of columnar shapes according to occuring phase. This fact agrees with the article of Zhang et al [64] where they have stated that the columnar morphology of the oxalates is independent of crystal structures. In accordance with the work of Dhal et al [122], herein dramatic morphology changes have not been observed during the heat treatment of the oxalate powders (FeOxA2, FeOxA3 and FeOxA6).

Zhang et al. [64] have defined the formation of columnar shaped iron oxalate based on the growth of the metal and oxalate chains along one dimension, regardless of the crystal structure. Interestingly, Figures 5.18.a-h reveal that although the columnar morphology of the oxalate structures remain intact, heat treatment under different atmosphere causes void formation in the structure.

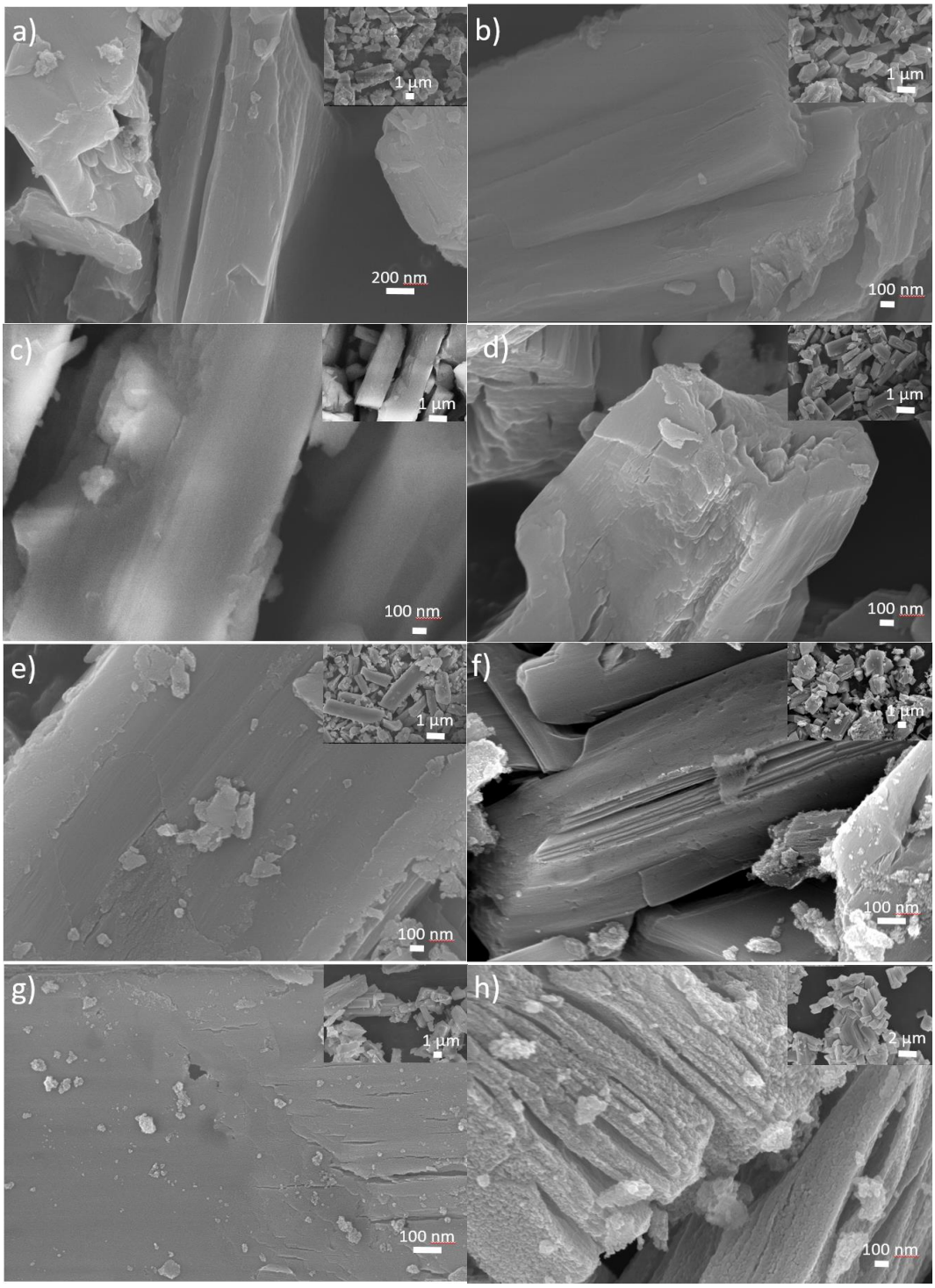

Figure 5.18: SEM images of achieved powders according to table 5.3 a) FeOxA2 b) FeOxA3 c) FeOxA6 d) FeO205 e) FeO215 f) FeO3003 g) FeO3002 h) FeO350Ar.

As Angerman et al [123] have mentioned, the topotactic calcination mechanism can be used to explain this observation. In case of iron oxide particles (FeO205, FeO215, FeO3002, FeO3003 and FeO350Ar) in Figure 5.17.d-h, some leafing in the morphology is noted.

A scrutiny analysis demonstrates that for oxalate powders (FeOxA2, FeOxA3 and FeOxA6) in Figure 5.18.a-c, most homogeneous morphology is achieved at 3 hours. When the temperature effect in vacuum atmosphere (FeOxA3 and FeO205) is studied, the rod size is noted to be increasedat high temperature. When temperature and duration effects in air atmosphere are discussed (FeO215 and FeO3003 (Figue 5.18.e-f) are compared) at elevated temperature or longer duration (FeO3003, FeO3002; Figure 5.18.f-g, respectively) diffusion in the particles is noted to be promoted, leading smaller aspect ratio.

5.4.4 Chemical analysis

The EDS analysis results of all samples demonstrate that the samples have 0.41±0.14% at. cobalt, 0.46±0.34% at. nickel, 0.35±0.34% at. manganese and 0.66±0.35 % at. chromium in their structure. These results agree with XRF result of the oxalate precursor for calcination and heat treatment operation (P2, see section 5.5). Trace amounts of transition metals (Ni, Cr, Mn) are present along with Fe.

EDS also reveals that lower than 0.1% at. sulphur detected on the samples which is caused from sulfuric acid that is used in leaching. The low content of S justifies that the samples are cleansed effectively after leaching and precipitation. Low amount of chromium content in all samples (Less than ~at. %1), demonstrate successful selective precipitation of iron from the leachate, eventually.

5.5 Electrochemical Tests

5.5.1 Galvanostatic test results

Anodes have been fabricated for electrochemical testing of synthesized powders of which properties are described in the experiment section (4.7.4). Electrodes in CR2032 standard half-cells are tested under a current load of 50 mA/g between 1 mV-3 V. Galvanostatic test results at room temperature are given in Figure 5.19.a-h. Active materials with different crystal structures and morphologies exhibit varying performance versus Li/Li^+.

Galvanostatic performances demonstrate that oxalate samples have higher capacity than the theoretical capacity value (373 mAh/g for iron oxalate) in cycling test. Possible explanation could be related to the pseudo capacitance effect of the oxalates [59]. In case of iron-rich oxalate samples that are calcinated in different durations at

the same temperature (FeOxA2, FeOxA3 and FeOxA6), FeOxA3 reveals the highest first discharge capacity. As seen in FTIR result of anhydrate oxalate powders (Figure 5.16), longer calcination duration causes lower intensity in the spectrum line and water has been completely removed from strucutre from 3 hours. Therefore, FeOxA3 has the highest capacity and FeOxA6 has a lower capacity value than FeOxA3. Possible detoriation of the structure at longer heat treatment duration may explain this.

When the iron-rich oxides performances are examined, it is seen that samples (FeO215, FeO3002 and FeO3003) have delivered higher discharge capacities than that of the graphite (372 mAh/g) at 100^{th} cycle. This fact substantiates that the approach presented in this thesis is promising to fabricate electrodes with high energy density. Although iron rich oxides have been produced via metallurgical grade precursor, obtained iron-rich oxide has a moderate first discharge capacity and long lasting capacity performans in comparison to those stated in the open literature (Tables 3.7, 3.8)

Figure 5.19.a-h demonstrate that FeOxA3 in iron-rich oxalate and FeO3002 in iron-rich oxide deliver the highest capacity and retention over 100 cycles, and FeO205 shows the weakest performance. The remarkable performance of FeO3002 is believed to be related to its particularities in the morphology (columunar morphology) and structure (Hematite). On the other hand, the poor crystalline (FeO205) structure is believed to explain this weak performance of FeO205, as agreed with the literature [128].

A scrutiny look in the galvanostatic test results exhibits that both crystallinity improves the cycle capability of the samples. Moreover, the irregular distribution of macroporosities in the particle (in the FeO350Ar) and inhomogeneity in the particle size (FeO215) are believed to deteriorate the performance of the electrode.

When the coulombic efficiencies of all tested samples are examined, it is understood that the solid electrolyte interface film formation [127] at the electrode/electrolyte interface and the destructive volume change performed upon lithation cause lower first discharge capacity and lower capacity over lasting cycles [128-130].

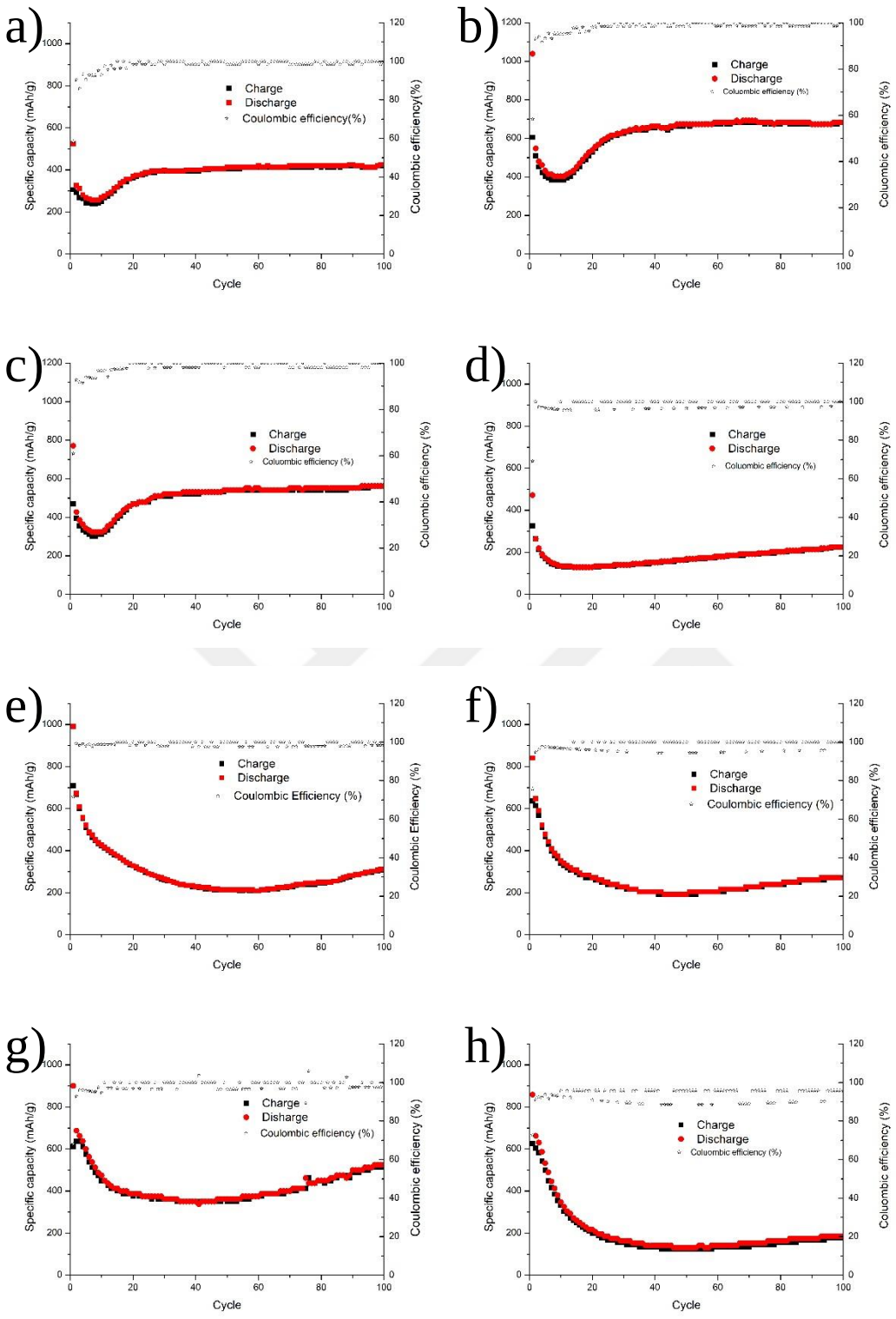

Figure 5.19: Capacity-cycle grarph of samples a) FeOxA2 b) FeOxA3 c) FeOxA6 d) FeO205 e) FeO215 f) FeO3003 g) FeO3002 h) FeO350Ar.

Voltage-Capacity curvatures of the samples are given in Figure 5.20.a-h. The iron-rich oxalates (FeOxA2, FeOxA3 and FeOxA6; Figure 5.18.a-c, respectively) that are fabricated within the scope of this thesis reveal similar lithiation characteristics as stated in the literature [61,64] (Figure 5.21.a-c). In the first cycle, a sharp voltage

decrease down to 1.2 V is noted. Afterwards, a slope is noted from 1.2 V to 1 mV (vs Li/Li^+). Upon charging no plateau is detected, which confirms the amorphization of the oxalate structure after the first discharge reaction. The following cycles justify the proposed lithiation mechanism of Ang et al. [61], as no plateau is observed on 2nd and 3rd discharge and charges cycles' curvatures: Ang et al. [61] have defined the electorchemical amorphization of the oxalate particles upto lithiation and claimed that at 1.6 V (vs Li/Li+), lithiation of oxalate happens following Equation 3.9.

On the other hand, as expected, the iron-rich oxides that are fabricated within the scope of this thesis demonstrate different curvatures (in Figure 5.20.d-h). All samples except from FeO350Ar reveal a similar capacity-voltage profiles like the micron-sized iron oxide has as stated by Larcher et al [48]. The samples reveal that upon the first discharge reaction, the voltage drops down from the open circuit potential voltage to 1.6 V (vs Li/Li^+) steeply. Then a less steepy slope is noted when the voltage gets down to 0.7 V (vs Li/Li^+). Around 0.7 V a plateau is noted for all samples as stated in the literature [6, 48, 129]. Down to lower potential (1 mV (vs Li/Li^+)) another slope is noted. Similar discharging curves are noted upon 2nd and 3rd discharge reactions. Larcher et al have explained that the plateau detected at 0.7 V for micron-sized iron oxide particle is related to the conversion reaction from iron oxide and lithium to iron and lithium oxide (see Equation 3.6).

In case of FeO350Ar, unlike to others, an additional small plateau is noted around 1V (along with small plateaus around 1.6 and 0.7V). This additional plateau is also noted in Larcher et al work [48] when they use nano-sized iron oxide as electrode material.

The absence of additional plateaus related to other transition metal oxide's lithiation justify the outcomes of XRD and FTIR analyses. It is believed that the transition metals may be present in the oxide strucutre as dopping metals and work as electron conductive pathways within the structure as suggested by Liu et al [132]. Further investigation will be done to define the positions of the transition metals in the iron oxide structure and their effects on the electrochemical performance of the anodes.

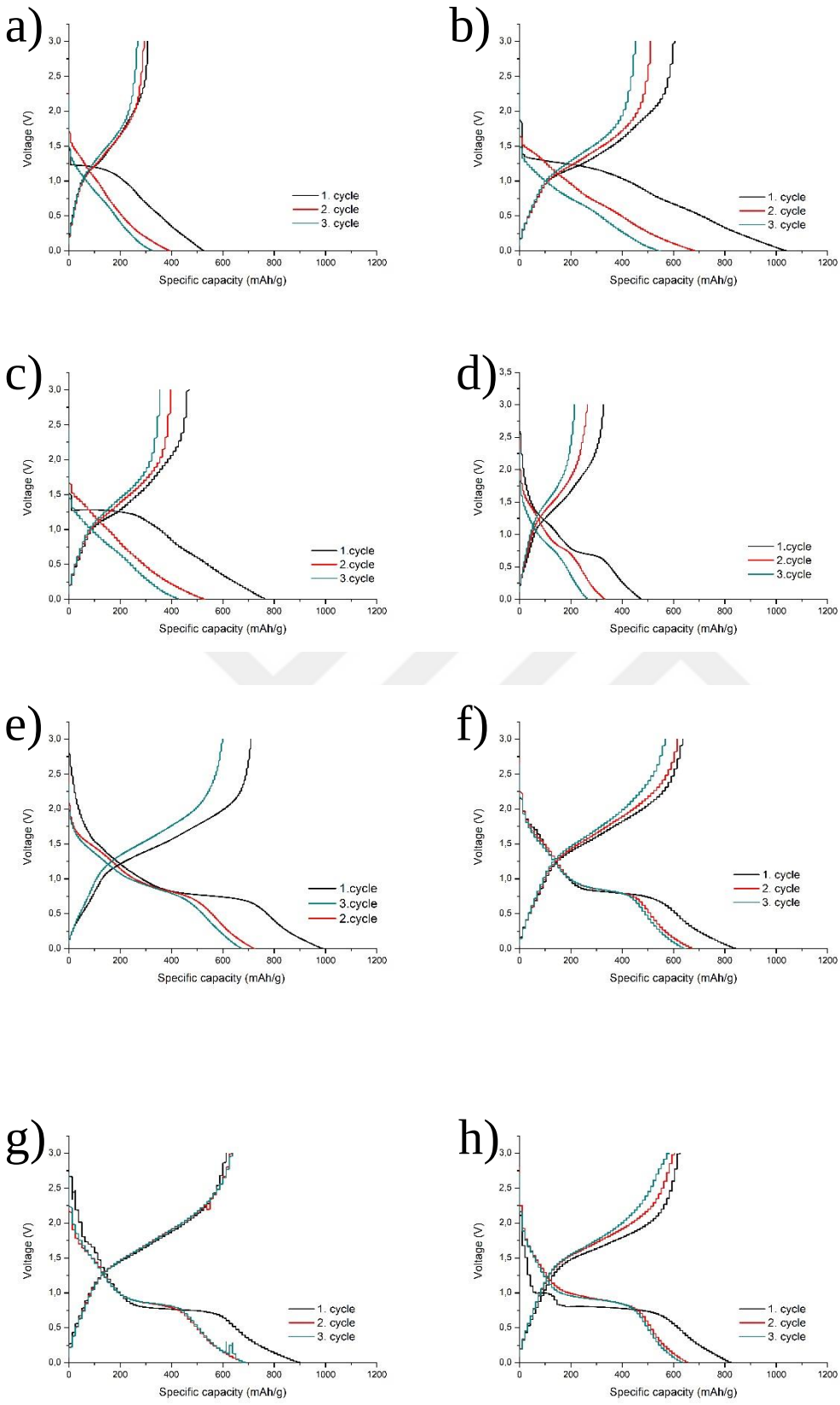

Figure 5.20: Voltage-capacity grarph of samples a) FeOxA2 b) FeOxA3 c) FeOxA6 d) FeO205 e) FeO215 f) FeO3003 g) FeO3002 h) FeO350Ar.

5.5.2 Cycling voltammetry results

Cycling voltammetry (CV) has been applied for determining electrochemical activities of all samples. Cyclic voltammetry results of the samples produced within the scope of this thesis are given in Figure 5.21.a.h. It is understood that CV curves of the structures obtained after the heat treatment are different from those of oxalate powders as expected.

In Figure 5.21.a-c, iron-rich oxalate (FeOxA2, FeOxA3 and FeOxA6) samples' CV results are given. All samples have peaks at 0.75 V and 1.2 V (vs Li/Li^+) at the cathodic region which verify the conversion reaction of Li^+ to form $Li_2C_2O_4$ and metallic iron [61, 64, 131]. In the 1^{st} cycle of all oxalate samples, the cathodic peak intensity is larger than the others. The change in the number and the intensity of the peaks upon cycling could be explained by SEI formation and phase transformation happened upon cycling [61, 64, 131]. On the anodic side, anodic hump appears around 1.5 V in all samples. This can be explained as the oxidation of metals [61].

In case of iron-rich oxide samples (Figure 5.21.d-h), a sharpy cathodic peak at 0.6 V which is related to the reduction of Fe^{3+} to Fe^0 and SEI formation on the electrode surface is noted [130]. After the 1^{st} cycle a peak shifting is noted at the cathodic region along with 2 cathodic peaks formation at 0.7 and 1.4V [132]. The shift in the peak position is caused due to increased polarization of the electrode over cycle [7,132]. And the generation of the additional peak at 1.5 V in FeO3002 and FeO3003 show multiple step reduction of iron oxide as claimed by Chaudhari et al. [7]. In anodic side, the peak around 1.75 V demonstrates reversible oxidation of metals [7].

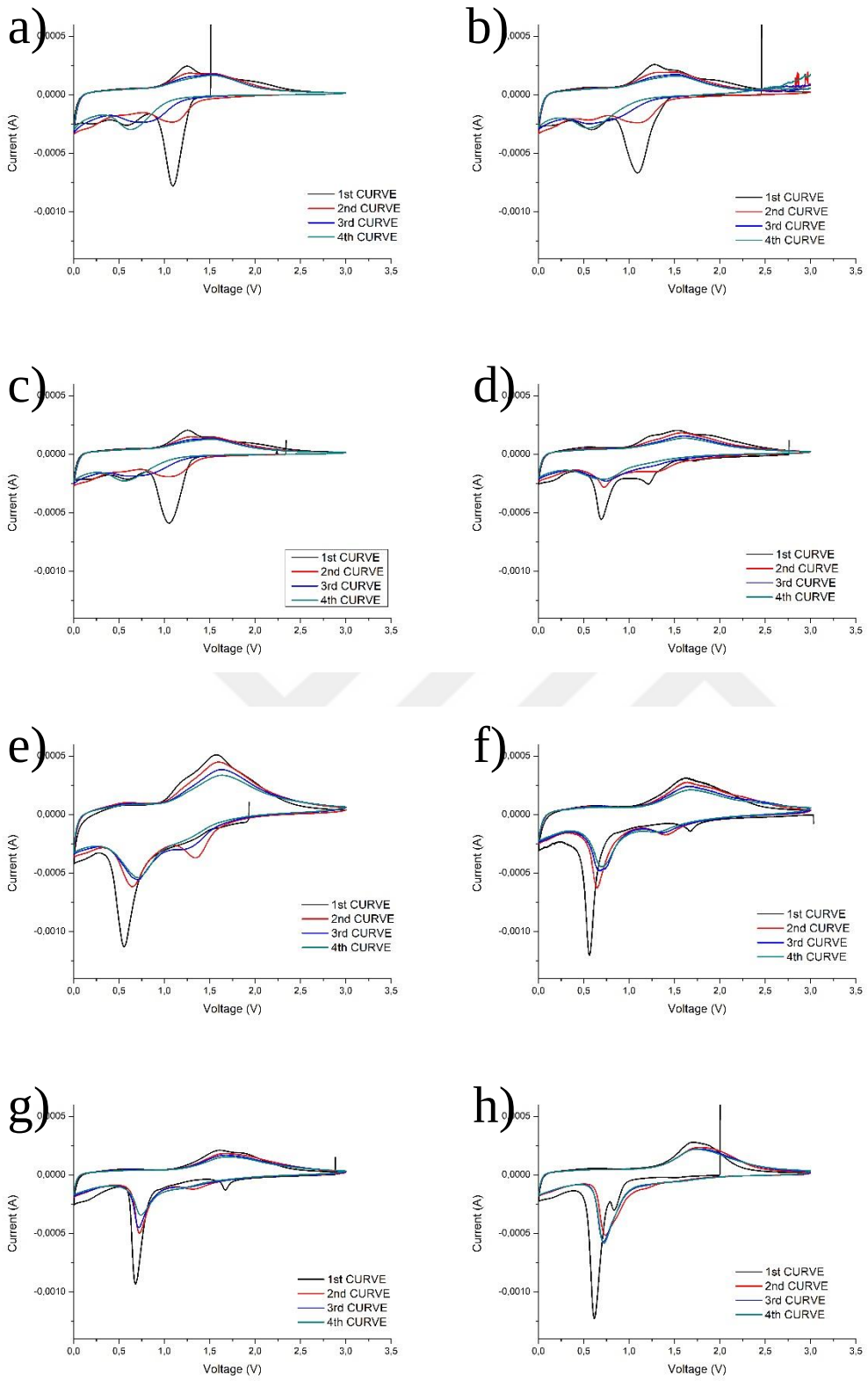

Figure 5.21: Cycling voltammetry grarph of samples a) FeOxA2 b) FeOxA3 c) FeOxA6 d) FeO205 e) FeO215 f) FeO3003 g) FeO3002 h) FeO350Ar.

6. CONCLUSION

In this thesis, chemical, structural and morphological analyses have determined that different types of iron-rich oxides (Hematite, magnetite and maghematite) and iron-rich oxalates are fabricated by precipitation and calcination routes. By the help of the approach presented in this thesis work, enviromental friendly and economical anode active material has been synthesized. Five samples show higher capacity (FeOxA2, FeOxA3, FeOxA6, FeO215 and FeO3002) values than that of the commercial graphite anode after 100 cycle. The outcomes of this research can be summarized as follows:

- The effect of parameters on FeCr milling (Milling duration, ball to powder ratio in weigth and rotation speed) have been investigated. Ferrochromium with 5% C have been milled to 2.78 μm in average (Dv50) by the help of Taguchi experimental desing: 3 parameter and 2 level. Optimum parameters are 4 hours, 235 rpm and 10:1 ball to powder ratio in weigth.
- ANOVA analysis demonstrates the most effective parameter of milling is duration.
- Milled Fe-Cr have been successfully leached by benefiting Taguchi orthogonal experiment design: 4 parameter and 3 levels. Control experiment has been run with 5 molar H_2SO_4, 1:50 solid:liquid ratio according to volume, 30 rpm and 90˚C.
- ANOVA analysis has been made to understand the most effective parameters on the leaching experiment designed following the Taguchi Orthagonal Array. The most effective parameter is found to be solid:liquid ratio for iron leaching.
- There is 91.88% correlation between the calculated value and AAS result of the control experiment.
- The effect of duration on the leaching has been investigated. The most iron containg solution is obtained at the end of 150 minutes when the experiment is run with the control experiment's parameters.
- Leaching kinetic has been investigated and determined as mixed model (surface reaction control; lixiviant diffusion model). Then, the activation energy of leaching is calculated as 46.12 kJ/mol

- The effect of parameters such as temperature, oxalic acid:leaching solution ratio (vol.:vol.) and rotating speed have been investigated for iron oxalate dihydrate (FeOxH) rods precipitation. Iron ions have been successfully precipitated with 86% efficiency at 25˚C with 1:5 oxalic acid:leaching solution ratio (vol.:vol.) and 450 rpm.
- Time, atmosphere and temperature effects have been examined and different types of iron-rich oxides in the shape of the rods (2.87±1.36 μm in length and 1.2±1.36 μm in width) (Magnetite, hematite and maghematite) have been produced.
- Galvanostatic tests shows that FeOxA3 has the highest 1st discharge capacity (1038.46 mAh/g) among the oxalates, and FeO215 has the highest 1st discharge capacity (989.58 mAh/g) among the oxide powders fabricated within the scope of this thesis.
- FeOxA2, FeOxA3, FeOxA6, FeO3002 and FeO2153 samples have revealed higher capacities over 100 cycle in comparison to that of the graphite (372 mAh/g).
- Further investigation will be done to define the positions of the transition metals in the iron oxide structure and their effects on the electrochemical performance of the anodes.

REFERENCES

[1] **Andres, R. J., Fielding, D. J., Marland, G., Boden, T. A., Kumar, N., & Kearney, A. T.** (1999). Carbon dioxide emissions from fossil-fuel use, 1751–1950. *Tellus B*, *51*(4), 759-765.

[2] **Turner, J. A. (1999).** A realizable renewable energy future. *Science*, *285*(5428), 687-689.

[3] **Poullikkas, A. (2013).** A comparative overview of large-scale battery systems for electricity storage. *Renewable and Sustainable energy reviews*, 27, 778-788.

[4] **Whittingham, M. S. (2012).** History, evolution, and future status of energy storage. *Proceedings of the IEEE*, 100(Special Centennial Issue), 1518-1534.

[5] **Kim, I. T., Magasinski, A., Jacob, K., Yushin, G., & Tannenbaum, R.** (2013). Synthesis and electrochemical performance of reduced graphene oxide/maghemite composite anode for lithium ion batteries. *Carbon*, 52, 56-64.

[6] **Nuli, Y., Zeng, R., Zhang, P., Guo, Z., & Liu, H.** (2008). Controlled synthesis of α-Fe2O3 nanostructures and their size-dependent electrochemical properties for lithium-ion batteries. *Journal of Power Sources*, 184(2), 456–461. doi: 10.1016/j.jpowsour.2008.03.004

[7] **Chaudhari, N. K., Kim, M. S., Bae, T. S., & Yu, J. S.** (2013). Hematite (α-Fe2O3) nanoparticles on vulcan carbon as an ultrahigh capacity anode material in lithium ion battery. *Electrochimica Acta*, 114, 60-67.

[8] **Zhang, L., Wu, H. B., & Lou, X. W.** (2014). Iron-oxide-based advanced anode materials for lithium-ion batteries. *Advanced Energy Materials*, 4(4), 1300958.

[9] **Dghoughi, L., Elidrissi, B., Bernede, C., Addou, M., Lamrani, M. A., Regragui, M., & Erguig, H.** (2006). Physico-chemical, optical and electrochemical properties of iron oxide thin films prepared by spray pyrolysis. *Applied Surface Science*, 253(4), 1823-1829.

[10] **Scrosati, B.** (2011). History of lithium batteries. *Journal of solid state electrochemistry*, 15(7-8), 1623-1630.

[11] **Wrublewski, D. T.** (2020). Analysis for Science Librarians of the 2019 Nobel Prize in Chemistry: Lithium-Ion Batteries. *Science & Technology Libraries*, 1-17

[12] **Díaz-González, F., Sumper, A., Gomis-Bellmunt, O., & Villafáfila-Robles, R.** (2012). A review of energy storage technologies for wind power applications. *Renewable and sustainable energy reviews*, 16(4), 2154-2171.

[13] **Nishi, Y.** (2014). Past, Present and Future of Lithium-Ion Batteries: Can New Technologies Open up New Horizons? *In Lithium-Ion Batteries* (pp. 21-39). Elsevier.

[14] **Chen, H., Cong, T. N., Yang, W., Tan, C., Li, Y., & Ding, Y.** (2009). Progress in electrical energy storage system: A critical review. *Progress in natural science*, 19(3), 291-312.

[15] **Liang, Y., Zhao, C. Z., Yuan, H., Chen, Y., Zhang, W., Huang, J. Q., Yui D., Liu, Y. Titirici, M. M., Chuen, Y. L., Yu, H. & Zhang, H.** (2019). A review of rechargeable batteries for portable electronic devices. *InfoMat*, 1(1), 6-32.

[16] **Blomgren, G. E.** (2016). The development and future of lithium ion batteries. *Journal of The Electrochemical Society*, 164(1), A5019.

[17] **Thackeray, M. M., Wolverton, C., & Isaacs, E. D.** (2012). Electrical energy storage for transportation—approaching the limits of, and going beyond, lithium-ion batteries. *Energy & Environmental Science*, *5*(7), 7854-7863.

[18] **Lee, H., Yanilmaz, M., Toprakci, O., Fu, K., & Zhang, X.** (2014). A review of recent developments in membrane separators for rechargeable lithium-ion batteries. Energy & Environmental Science, 7(12), 3857-3886.

[19] **Huang, X.** (2011). Separator technologies for lithium-ion batteries. *Journal of Solid State Electrochemistry*, 15(4), 649-662.

[20] **Jow, T. R., Xu, K., Borodin, O., & Ue, M.** (Eds.). (2014). *Electrolytes for lithium and lithium-ion batteries* (Vol. 58). New York: Springer.

[21] **Xu, K.** (2004). Nonaqueous liquid electrolytes for lithium-based rechargeable batteries. *Chemical reviews*, 104(10), 4303-4418.

[22] **Aravindan, V., Gnanaraj, J., Madhavi, S., & Liu, H. K.** (2011). Lithium-ion conducting electrolyte salts for lithium batteries. *Chemistry–A European Journal*, 17(51), 14326-14346.

[23] **Ue, M.** (2009). Electrolytes: nonaqueous in encyclopedia of electrochemical power sources. *Elsevier* BV, 71-84.

[24] **Tarascon, J. M., & Guyomard, D.** (1994). New electrolyte compositions stable over the 0 to 5 V voltage range and compatible with the Li1+ xMn2O4/carbon Li-ion cells. *Solid State Ionics*, 69(3-4), 293-305.

[25] **Zhou, H., Fang, Z., & Li, J.** (2013). LiPF6 and lithium difluoro (oxalato) borate/ethylene carbonate+ dimethyl carbonate+ ethyl (methyl) carbonate electrolyte for Li4Ti5O12 anode. *Journal of Power Sources*, 230, 148-154.

[26] **Melot, B. C., & Tarascon, J. M.** (2013). Design and preparation of materials for advanced electrochemical storage. *Accounts of chemical research*, 46(5), 1226-1238.

[27] **Ebin, B.** (2014). Lityum İyon Pilleri İçin Nanoyapılı Ve Yüksek Kapasiteli Katot Malzemelerinin Aerosol Tekniği İle Üretimi (Doctoral dissertation, Fen Bilimleri Enstitüsü).

[28] **Gulbinska, M. K.** (Ed.). (2014). Lithium-ion battery materials and engineering: current topics and problems from the manufacturing perspective. Springer.

[29] **Reddy, M. V., Subba Rao, G. V., & Chowdari, B. V. R.** (2013). Metal oxides and oxysalts as anode materials for Li ion batteries. *Chemical reviews*, 113(7), 5364-5457.

[30] **Nitta, N., Wu, F., Lee, J. T., & Yushin, G.** (2015). Li-ion battery materials: present and future. *Materials today*, 18(5), 252-264.

[31] **Kalbáč, M., Zukalová, M., & Kavan, L.** (2003). Phase-pure nanocrystalline Li 4 Ti 5 O 12 for a lithium-ion battery. *Journal of Solid State Electrochemistry*, 8(1), 2-6.

[32] **Zhang, W. J.** (2011). A review of the electrochemical performance of alloy anodes for lithium-ion batteries. *Journal of Power Sources*, 196(1), 13-24.

[33] **Xiao, X., Li, X., Zheng, S., Shao, J., Xue, H., & Pang, H.** (2017). Nanostructured germanium anode materials for advanced rechargeable batteries. *Advanced Materials Interfaces*, 4(6), 1600798.

[34] **Poizot, P. L. S. G., Laruelle, S., Grugeon, S., Dupont, L., & Tarascon, J. M.** (2000). Nano-sized transition-metal oxides as negative-electrode materials for lithium-ion batteries. *Nature*, 407(6803), 496.

[35] **Bhatt, M. D., & Lee, J. Y.** (2019). High capacity conversion anodes in Li-ion batteries: A review. *International Journal of Hydrogen Energy*, 44(21), 10852-10905.

[36] **Abu-Lebdeh, Y., & Davidson, I. (Eds.).** (2012). Nanotechnology for lithium-ion batteries. Springer Science & Business Media.

[37] **Zu, C. X., & Li, H.** (2011). Thermodynamic analysis on energy densities of batteries. *Energy & Environmental Science*, 4(8), 2614-2624.

[38] **Bhatt, M. D., & Lee, J. Y.** (2019). High capacity conversion anodes in Li-ion batteries: A review. *International Journal of Hydrogen Energy*, 44(21), 10852-10905.

[39] **Xu, J., He, L., Liu, H., Han, T., Wang, Y., Zhang, C., & Zhang, Y.** (2015). Controlled synthesis of porous anhydrous cobalt oxalate nanorods with high reversible capacity and excellent cycling stability. *Electrochimica Acta*, 170, 85–91. doi:10.1016/j.electacta.2015.04.114

[40] **Hu, J., Li, H., & Huang, X.** (2005). Cr2 O 3-Based Anode Materials for Li-Ion Batteries. *Electrochemical and solid-state letters*, 8(1), A66-A69.

[41] **Aydın, S.** (2014). Metalurji ve Malzeme Mühendisleri için TERMODİNAMİK. Istanbul: Literatur

[42] **Wang, F., Chen, J., Huang, K., & Liu, S.** (2009). Preparation and electrochemical performance of spherical Fe3O4 as anode materials for Li-ion batteries. *Science in China Series E: Technological Sciences*, 52(11), 3219–3223. doi:10.1007/s11431-009-0310-2

[43] **Petnikota, S., Marka, S. K., Banerjee, A., Reddy, M. V., Srikanth, V. V. S. S., & Chowdari, B. V. R.** (2015). Graphenothermal reduction synthesis of ‘exfoliated graphene oxide/iron (II) oxide’composite for anode application in lithium ion batteries. *Journal of Power Sources*, 293, 253-263.

[44] **Han, Y., Wang, Y., Li, L., Wang, Y., Jiao, L., Yuan, H., & Liu, S.** (2011). Preparation and electrochemical performance of flower-like hematite for lithium-ion batteries. Electrochimica Acta, 56(9), 3175-3181.

[45] **Chaudhari, N. K., Kim, M. S., Bae, T. S., & Yu, J. S.** (2013). Hematite (α-Fe2O3) nanoparticles on vulcan carbon as an ultrahigh capacity anode material in lithium ion battery. *Electrochimica Acta*, 114, 60-67.

[46] **Zhu, J., Lu, Y., Chen, C., Ge, Y., Jasper, S., Leary, J. D., Li, D., Jiang, M. & Zhang, X.** (2016). Porous one-dimensional carbon/iron oxide composite for rechargeable lithium-ion batteries with high and stable capacity. *Journal of Alloys and Compounds*, 672, 79-85.

[47] **Golmohammad, M., Golestanifard, F., & Mirhabibi, A.** (2016). Synthesis and characterization of maghemite as an anode for lithium-ion batteries. *Int. J. Electrochem. Sci*, 11, 6432-6442.

[48] **Larcher, D., Masquelier, C., Bonnin, D., Chabre, Y., Masson, V., Leriche, J. B., & Tarascon, J. M.** (2003). Effect of Particle Size on Lithium Intercalation into α Fe2 O 3. *Journal of the Electrochemical Society*, 150(1), A133-A139.

[49] **Wang, C., Wang, L., & Tang, K.** (2013). Synthesis of mesoporous Fe2O3 nanorods and their electrochemical performance. *Int. J. Electrochem. Sci*, 8, 4543-4550.

[50] **Chun, L., Wu, X., Lou, X., & Zhang, Y.** (2010). Hematite nanoflakes as anode electrode materials for rechargeable lithium-ion batteries. *Electrochimica acta*, 55(9), 3089-3092.

[51] **Liu, H., Wexler, D., & Wang, G.** (2009). One-pot facile synthesis of iron oxide nanowires as high capacity anode materials for lithium ion batteries. *Journal of Alloys and Compounds*, 487(1-2). doi: 10.1016/j.jallcom.2009.08.043

[52] **Li, M. Y., Wang, Y., Liu, C. L., Gao, H., & Dong, W. S.** (2012). Iron oxide/carbon microsphere lithium-ion battery electrode with high capacity and good cycling stability. *Electrochimica acta*, 67, 187-193.

[53] **Mai, Y. J., Tu, J. P., Xia, X. H., Gu, C. D., & Wang, X. L.** (2011). Co-doped NiO nanoflake arrays toward superior anode materials for lithium ion batteries. *Journal of Power Sources*, 196(15), 6388-6393.

[54] **Shi, S., Liu, L., Ouyang, C., Wang, D. S., Wang, Z., Chen, L., & Huang, X.** (2003). Enhancement of electronic conductivity of LiFePO 4 by Cr doping and its identification by first-principles calculations. *Physical Review B*, 68(19), 195108.

[55] **Lin, C., Lai, M. O., Lu, L., Zhou, H., & Xin, Y.** (2013). Structure and high rate performance of Ni2+ doped Li4Ti5O12 for lithium ion battery. *Journal of power sources*, 244, 272-279.

[56] **Yeoh, J. S., Armer, C. F., & Lowe, A.** (2018). Transition metal oxalates as energy storage materials. A review. *Materials Today Energy*, 9, 198–222. doi:10.1016/j.mtener.2018.05.010

[57] **León, B., Vicente, C. P., & Tirado, J. L.** (2012). New mixed transition metal oxysalts as negative electrode materials for lithium-ion batteries. Solid State Ionics, 225, 518-521.

[58] **Aragón, M. J., Leon, B., Perez Vicente, C., Tirado, J. L., Chadwick, A. V., Berko, A., & Beh, S. Y.** (2009). Cobalt oxalate nanoribbons as negative-electrode material for lithium-ion batteries. Chemistry of Materials, 21(9), 1834-1840.

[59] **López, M. C., Tirado, J. L., & Vicente, C. P.** (2013). Structural and comparative electrochemical study of M (II) oxalates, M= Mn, Fe, Co, Ni, Cu, Zn. Journal of power sources, 227, 65-71.

[60] **León, B., Vicente, C. P., & Tirado, J. L.** (2012). New mixed transition metal oxysalts as negative electrode materials for lithium-ion batteries. *Solid State Ionics*, 225, 518-521.

[61] **Ang, W. A., Gupta, N., Prasanth, R., & Madhavi, S.** (2012). High-performing mesoporous iron oxalate anodes for lithium-ion batteries. ACS applied materials & interfaces, 4(12), 7011-7019.

[62] **Oh, H. J., Jo, C. H., Yoon, C. S., Yashiro, H., Kim, S. J., Passerini, S., Sun, Y. K. & Myung, S. T.** (2016). Nickel oxalate dihydrate nanorods attached to reduced graphene oxide sheets as a high-capacity anode for rechargeable lithium batteries. *NPG Asia Materials*, 8(5), e270-e270.

[63] **Pang, H., Wang, S., Li, X., Zhao, S., Zhang, N., Chen, J., Zhang, J., Zheng, H., & Li, S.** (2013). Controlled fabrication of iron oxalate hydrate microstructures and study of their electrochemical properties. *Int. J. Electrochem. Sci.*, 8, 4174-4182.

[64**] Zhang, K., Li, Y., Wang, Y., Zhao, J., Chen, X., Dai, Y., & Yao, Y.** (2020). Enhanced electrochemical properties of iron oxalate with more stable Li+ ions diffusion channels by controlling polymorphic structure. *Chemical Engineering Journal*, 384, 123281.

[65] **Aragón, M. J., León, B., Perez Vicente, C., & Tirado, J. L.** (2008). Synthesis and electrochemical reaction with lithium of mesoporous iron oxalate nanoribbons. *Inorganic chemistry*, 47(22), 10366-10371.

[66] **Gonzalez-Carreno, T., Morales, M. P., Gracia, M., & Serna, C. J.** (1993). Preparation of uniform γ-Fe2O3 particles with nanometer size by spray pyrolysis. Materials Letters, 18(3), 151-155.

[67] **Wu, Y., & Wang, X.** (2011). Preparation and characterization of single-phase α-Fe2O3 nano-powders by Pechini sol–gel method. Materials Letters, 65(13), 2062-2065.

[68] **Li, Y., Liao, H., & Qian, Y.** (1998). Hydrothermal synthesis of ultrafine α-Fe2O3 and Fe3O4 powders. Materials research bulletin, 33(6), 841-844.

[69] **Sahoo, S. K., Agarwal, K., Singh, A. K., Polke, B. G., & Raha, K. C.** (2010). Characterization of γ-and α-Fe 2 O 3 nano powders synthesized by emulsion precipitation-calcination route and rheological behaviour of α-Fe 2 O 3. International Journal of Engineering, Science and Technology, 2(8).

[70] **Arbain, R., Othman, M., & Palaniandy, S.** (2011). Preparation of iron oxide nanoparticles by mechanical milling. Minerals Engineering, 24(1), 1-9.

[71] **Aydin, S., Ersundu, E., & Yücel, O.** Ferroalloy Production and Consumption in Türkiye.

[72] **Url-1** <https://www.metals-hub.com/en/blog/ferrochrome-plants-worldwide-and-their-annual-production-capacity/>, date retrieved 20.03.2020

[73] **Mohanty, U. S., Rintala, L., Halli, P., Taskinen, P., & Lundström, M.** (2018). Hydrometallurgical approach for leaching of metals from copper rich side stream originating from base metal production. *Metals*, 8(1), 40.

[74] **Tzeferis, P. G., & Agatzini-Leonardou, S.** (1994). Leaching of nickel and iron from Greek non-sulphide nickeliferous ores by organic acids. Hydrometallurgy, 36(3), 345-360.

[75] **Ige, J., Akanni, M. S., Morakinyo, M. K., & Owoyomi, O.** (2005). A kinetic study of the leaching of iron and manganese from a Nigerian tantalite-columbite ore. *Journal of Applied Sciences*, 5(3), 496-502.

[76] **Bar D, E.L. & Barket, D.** (2018). Leaching of metals from hydrometallurgical residue by Sulfuric Acid. *Aspects in Mining & Mineral Science* 1(4). DOI: 10.31031/AMMS.2018.01.000518

[77] **Liu, C. J., Qi, J., & Jiang, M. F.** (2011). Experimental Study on Sulfuric Acid Leaching Behavior of Chromite with Different Temperature. *Advanced Materials Research*, 361-363, 628–631. doi:10.4028/www.scientific.net/amr.361-363.628

[78] **El Bar, D., & Barket, D.** (2015). The leaching of sulfide iron (II) with sulfuric acid. *Journal of Mining Science*, 51(1), 179-185.

[79] **Zhao, Q., Liu, C., Shi, P., Zhang, B., Jiang, M., Zhang, Q., Saxen, H. & Zevenhoven, R.** (2014). Sulfuric acid leaching of South African chromite. Part 1: Study on leaching behavior. *International Journal of Mineral Processing*, 130, 95-101.

[80] **Liu, J. J., Hu, G. R., Du, K., Peng, Z. D., & Cao, Y. B.** (2014). Influencing factors and kinetics analysis of a new clean leaching process for producing chromate from Cr–Fe alloy. Journal of Cleaner Production, 84, 746-751.

[81] **Geelhoed, J. S., Meeussen, J. C., Roe, M. J., Hillier, S., Thomas, R. P., Farmer, J. G., & Paterson, E.** (2003). Chromium remediation or release? Effect of iron (II) sulfate addition on chromium (VI) leaching from columns of chromite ore processing residue. *Environmental science & technology*, 37(14), 3206-3213.

[82] **Mandiwana, K. L.** (2008). Rapid leaching of Cr (VI) in soil with Na3PO4 in the determination of hexavalent chromium by electrothermal atomic absorption spectrometry. *Talanta*, 74(4), 736-740.

[83] **Geveci, A., Topkaya, Y., & Ayhan, E.** (2002). Sulfuric acid leaching of Turkish chromite concentrate. Minerals Engineering, 15(11), 885-888.

[84] **Coetzer, G., Giesekke, E. W., & Guest, R. N.** (1997). Hexavalent chromium in the recovery of ferrochromium from slag. *Canadian Metallurgical Quarterly*, 36(4), 261-268

[85] **Liu, J. J., Hu, G. R., Du, K., Peng, Z. D., Wang, W. G., & Cao, Y. B.** (2014). The new technique on separation of Cr and Fe as well as Ni-Co-Mn impurity in leaching sulfate solution of ferrochrome alloy. *Russian Journal of Non-Ferrous Metals*, 55(6), 533-537.

[86] **Chen, L., Tang, X., Zhang, Y., Li, L., Zeng, Z., & Zhang, Y.** (2011). Process for the recovery of cobalt oxalate from spent lithium-ion batteries. Hydrometallurgy, 108(1-2), 80-86.

[87] **Sahu, K. K., & Das, R. P.** (1997). Synergistic extraction of iron (III) at higher concentrations in D2EHPA-TBP mixed solvent systems. *Metallurgical and Materials Transactions B*, 28(2), 181-189.

[88] **Hayes, P. C.** (2003). Process principles in minerals and materials production

[89] **Nowack, B., & Sigg, L.** (1996). Adsorption of EDTA and metal–EDTA complexes onto goethite. *Journal of Colloid and Interface Science*, 177(1), 106-121.

[90] **Shokrollahi, H. J. J. O. M.** (2017). A review of the magnetic properties, synthesis methods and applications of maghemite. Journal of Magnetism and Magnetic Materials, 426, 74-81

[91] **Rozenberg, G. K., Amiel, Y., Xu, W. M., Pasternak, M. P., Jeanloz, R., Hanfland, M., & Taylor, R. D.** (2007). Structural characterization of temperature-and pressure-induced inverse↔ normal spinel transformation in magnetite. Physical Review B, 75(2), 020102.

[92] **Peshev D. & Tsyrnorechki O.**, Chem. Abstr. 55 (1961) 913711.

[93] **J. Gopalakrıshnan**, private communication

[94] **Tailhades, P., Sarda, C., Bonino, C., Mollard, P., & Rousset, A.** (1990). Magnetic properties of boron and cobalt doped iron oxide pigments prepared from oxalic precursors. *Journal of magnetism and magnetic materials*, 89(1-2), 33-37.

[95] **Zhou, W., Tang, K., Zeng, S., & Qi, Y.** (2008). Room temperature synthesis of rod-like FeC2O4· 2H2O and its transition to maghemite, magnetite and hematite nanorods through controlled thermal decomposition. *Nanotechnology*, 19(6), 065602.

[96] **Krishnaiah, K., & Shahabudeen, P.** (2012). Applied design of experiments and Taguchi methods. PHI Learning Pvt. Ltd.

[97] **Lawson, J.** (2014). *Design and Analysis of Experiments with R* (Vol. 115). CRC press.

[98] **Url-2** <http://itulabs.itu.edu.tr/Cihaz.aspx?id=7b55f61b-d8a5-44b1-be5f-7b0f9d57bf84>, date retrieved 22.04.2019

[99] **Enayati, M. H., Bafandeh, M. R., & Nosohian, S.** (2007). Ball milling of stainless steel scrap chips to produce nanocrystalline powder. *Journal of Materials Science*, 42(8), 2844–2848. doi:10.1007/s10853-006-1371-2

[100] **Coedo, A. G., Dorado, T., Rivero, C. J., & Cobo, I. G.** (1993). Study of X-ray fluorescence spectrometry and spark ablation inductively coupled plasma atomic emission spectrometry for chromium determination in ferrochromium from bulk metal samples. *Journal of Analytical Atomic Spectrometry*, 8(7), 1023. doi:10.1039/ja9930801023

[101] **Url-3** <http://tr.etikrom.com/?mode=urundetay&UID=1271>, date retrieved 10 March 2020

[102] **Leško, A., & Navara, E.** (1996). Microstructural characterization of high-carbon ferrochromium. *Materials characterization*, 36(4-5), 349-356.

[103] **Maslyuk, V. A., Bondar, A. A., Pidoprygora, M. I., & Varchenko, V. M.** (2013). Structure and properties of iron–high-carbon ferrochrome powder composites. *Powder Metallurgy and Metal Ceramics*, 52(5-6), 291-297.

[104] **Agarwal, S., Pal, J., & Ghosh, D.** (2016). Smelting characteristics of fluxed chromite sinter and its performance assessment in electric arc furnace to produce high carbon ferrochrome. *Ironmaking & Steelmaking*, 43(2), 97-111

[105] **Ge, X., Jin, S., Zhang, M., Wang, X., & Seetharaman, S.** (2015). Synthesis of chromium and ferrochromium alloy in molten salts by the electro-reduction method. *Journal of Mining and Metallurgy B: Metallurgy*, 51(2), 185-191.

[106] **Teja Ruiz, A. M., Juárez Tapia, J. C., Reyes Domínguez, I. A., Hernández Cruz, L. E., Pérez, M. R., Patiño Cardona, F., Flores Guerrero, M. U.** (2017). Kinetic Study of Ag Leaching from Arsenic Sulfosalts in the S2O32−-O2-NaOH System. *Metals*, 7(10), 411. https://doi.org/10.3390/met7100411

[107] **Nadirov, R. & Mussapyrova, L.** (2020). Effect of Mechanical Activation on Leachability of Fayalite in Sulfuric Acid Solution. *Current Physical Chemistry* (2020) 10: 82. https://doi.org/10.2174/1877946810666200128152729

[108] **Havlik, T., Turzakova, M., Stopic, S., & Friedrich, B.** (2005). Atmospheric leaching of EAF dust with diluted sulphuric acid. Hydrometallurgy, 77(1-2), 41-50. https://doi.org/10.1016/j.hydromet.2004.10.008

[109] **Yu, Z., Xie, K., Ma, W., Zhou, Y., Xie, G., & Dai, Y.** (2011). Kinetics of iron removal from metallurgical grade silicon with pressure leaching. *Rare Metals*, 30(6), 688-694. https://doi.org/10.1007/s12598-011-0450-y

[110] **Gireesh, V. S., Vinod, V. P., Nair, S. K., & Ninan, G.** (2013). Effect of sulphate ions on leaching of ilmenite with hydrochloric acid. *Journal of Academia and Industrial Research* (JAIR), 2(7), 402.

[111] **Sokić, M. D., Marković, B., & Živković, D.** (2009). Kinetics of chalcopyrite leaching by sodium nitrate in sulphuric acid. *Hydrometallurgy*, 95(3-4), 273-279. https://doi.org/10.1016/j.hydromet.2008.06.012

[112] **Georgiou, D., & Papangelakis, V. G.** (1998). Sulphuric acid pressure leaching of a limonitic laterite: chemistry and kinetics. *Hydrometallurgy*, 49(1-2), 23-46. https://doi.org/10.1016/S0304-386X(98)00023-1

[113] **Mulak, W., Miazga, B., & Szymczycha, A.** (2005). Kinetics of nickel leaching from spent catalyst in sulphuric acid solution. *International Journal of Mineral Processing*, 77(4), 231-235. https://doi.org/10.1016/j.minpro.2005.06.005

[114] **Aydogan, S., Aras, A., & Canbazoglu, M.** (2005). Dissolution kinetics of sphalerite in acidic ferric chloride leaching. *Chemical Engineering Journal*, 114(1-3), 67-72. https://doi.org/10.1016/j.cej.2005.09.005

[115] **Nekrasov B.V.** Fundamentals of General Chemistry. - T.2. - M.: Chemistry, 1973. - pp. 363

[116] **Hussain, S. T., & Khan, G. A.** (2012). Solubility of Oxalic Acid. *Asian Journal of Research in Chemistry*, 5(11), 1323-1330.

[117] **D'Antonio, M. C., Wladimirsky, A., Palacios, D., Coggiolaa, L., González-Baró, A. C., Baran, E. J., & Mercader, R. C.** (2009). Spectroscopic investigations of iron(II) and iron(III) oxalates. *Journal of the Brazilian Chemical Society*, 20(3), 445–450. doi:10.1590/s0103-50532009000300006

[118] **El-Batal, F. H., Khalil, E. M., Hamdy, Y. M., Zidan, H. M., Aziz, M. S., & Abdelghany, A. M.** (2010). FTIR spectral analysis of corrosion mechanisms in soda lime silica glasses doped with transition metal oxides. *Silicon*, 2(1), 41-47.

[119] **Rao, V., Shashimohan, A. L., & Biswas, A. B.** (1974). Studies on the formation of γ-Fe 2 O 3 (maghemite) by thermal decomposition of ferrous oxalate dihydrate. *Journal of Materials Science*, 9(3), 430-433.

[120] **Kashyap, R., Talukdar, D. J., & Pratihar, S.** (2015). Iron oxalate capped iron–copper nanomaterial for oxidative transformation of aldehydes. *New Journal of Chemistry*, 39(2), 1430-1437.

[121] **Hermanek, M., Zboril, R., Mashlan, M., Machala, L., & Schneeweiss, O.** (2006). Thermal behaviour of iron (II) oxalate dihydrate in the atmosphere of its conversion gases. *Journal of Materials Chemistry*, 16(13), 1273-1280.

[122] **Dhal, J. P., Mishra, B. G., & Hota, G.** (2015). Ferrous oxalate, maghemite and hematite nanorods as efficient adsorbents for decontamination of Congo red dye from aqueous system. *International Journal of Environmental Science and Technology*, 12(6), 1845-1856.

[123] **Angermann, A., & Töpfer, J.** (2008). Synthesis of magnetite nanoparticles by thermal decomposition of ferrous oxalate dihydrate. *Journal of materials science*, 43(15), 5123-5130.

[124] **Rahman, M. M., Jamal, A., Khan, S. B., & Faisal, M.** (2011). Characterization and applications of as-grown β-Fe 2 O 3 nanoparticles prepared by hydrothermal method. *Journal of Nanoparticle Research*, 13(9), 3789-3799.

[125] **Winter, M., Appel, W. K., Evers, B., Hodal, T., Möller, K. C., Schneider, I., Wacthler, M., Wagner, M. R., Wrodnigg, G. H. & Besenhard, J. O.** (2001). Studies on the anode/electrolyte interface in lithium ion batteries. In Electroactive Materials (pp. 53-66). Springer, Vienna.

[126] **Gao, X. P., Bao, J. L., Pan, G. L., Zhu, H. Y., Huang, P. X., Wu, F., & Song, D. Y.** (2004). Preparation and electrochemical performance of polycrystalline and single crystalline CuO nanorods as anode materials for Li ion battery. *The Journal of Physical Chemistry B*, 108(18), 5547-5551.

[127] **Li, M., Wang, W., Yang, M., Lv, F., Cao, L., Tang, Y., Sun, Y. & Lu, Z.** (2015). Large-scale fabrication of porous carbon-decorated iron oxide microcuboids from Fe–MOF as high-performance anode materials for lithium-ion batteries. RSC Advances, 5(10), 7356-7362.

[128] **Chen, Y., Xia, H., Lu, L., & Xue, J.** (2012). Synthesis of porous hollow Fe 3 O 4 beads and their applications in lithium ion batteries. Journal of Materials Chemistry, 22(11), 5006-5012.

[129] **Wang, F., Chen, J., Huang, K., & Liu, S.** (2009). Preparation and electrochemical performance of spherical Fe3O4 as anode materials for Li-ion batteries. *Science in China Series E: Technological Sciences*, 52(11), 3219–3223. doi:10.1007/s11431-009-0310-2

[130] **Hu, G. R., Liu, J. J., Du, K., Peng, Z. D., Cao, Y. B., Wang, W. G., & Duan, J. G.** (2014). Preparing high performance of LiFe (1− x) MxPO4 by using Fe (1− x) MxC2O4 as raw material precipitated from ferrochrome alloy leaching solution. Physica B: Condensed Matter, 446, 67-70.

[131] **Zhang, K., Liang, F., Wang, Y., Dai, Y., & Yao, Y.** (2019). Multilayer iron oxalate with a mesoporous nanostructure as a high-performance anode material for lithium-ion batteries. *Journal of Alloys and Compounds*, 779, 91-99.

[132] **Liu, H., Wexler, D., & Wang, G.** (2009). One-pot facile synthesis of iron oxide nanowires as high capacity anode materials for lithium ion batteries. Journal of Alloys and Compounds, 487(1-2), L24-L27.

CURRICULUM VITAE

Name Surname **:** Mehmet Feryat GÜLCAN

Place and Date of Birth **:** Kadıköy, 09.01.1995

E-Mail **:** mferyatglcan@gmail.com

EDUCATION **:**

- **B.Sc.** **:** 2018, Istanbul Technical University, Chemistry and Metallurgy Faculty, Metallurgical and Material Engineering

PROFESSIONAL EXPERIENCE AND REWARDS:

- Researcher in 218M768 since April 2019

OTHER PUBLICATIONS, PRESENTATIONS AND PATENTS:

- **Gülcan, F. M.,** & Karahan, B. D. (2019). Fabrication of Metal oxalates as anode material for Lithium Ion Batteries. Presented at the International Materials Technologies and Metallurgy Conference 2019, Istanbul .